CONVECTIVE ASSEMBLY OF NON-SPHERICAL COLLOIDS

A Dissertation

Presented to the Faculty of the Graduate School

of Cornell University

In Partial Fulfillment of the Requirements for the Degree of

Doctor of Philosophy

by

Ian Dean Hosein

May 2009

CONVECTIVE ASSEMBLY OF NON-SPHERICAL COLLOIDS

Ian Dean Hosein, Ph. D.

Cornell University 2009

Fabricating colloidal based materials from non-spherical particles shows the potential to produce materials having a broader diversity of particle packing arrangements and crystal lattice symmetries than possible for spherical bases. These new materials show enhanced structure-property relations, specifically, in terms of photonic bandgap properties. In order to access these enchance properties, a viable method to assemble non-spherical based ordered structures is required. This dissertation describes the application of the convective self-assembly technique to fabricated regular two- and three-dimensional structures from disc, hemispherical cap, spherocylinder and dumbbell shaped colloids.

Aqueous particle suspensions with controlled volume fraction permitted the assembly of large scale crystalline monolayers on substrates vertically immersed in the suspension, as the solvent was evaporated. Systematically tuning the particle volume fraction induced different particle packing arrangements in the monolayer. The monolayer structures were then correlated to the crystallization rate and suspension concentration, the two key convective assembly parameters, establishing process control of film structure in the monolayer regime. Adjusting the parameters for slower film deposition, higher suspension concentrations were used to extend the convective assembly technique three-dimensional structures from spherocylinder and dumbbell shaped particles.

Additionally, the photonic band structures of crystals with face-centered cubic

(FCC) and base-centered monoclinic lattices and dumbbell shape bases were calculated. The band structures revealed that a range of particle shapes produced complete photonic bandgaps.

BIOGRAPHICAL SKETCH

Ian was born and raised in the city of Toronto, Canada. From a young age, he was interested in math and sciences, and decided early that engineering was the perfect fit for his career aspirations. He completed his secondary education at Albert Campbell Collegiate Institute, and attended the University of Toronto for his undergraduate studies in Engineering Science. It was his undegrad years that sparked his interest in scientific research and teaching. For three consecutive summers during his undergraduate studies, Ian worked as science camp counselor at the University of Toronto's Science Outreach program, developing and teaching projects that would inspire future generations of scientists and engineers. In the summer of 2003, Ian received a Natural Sciences and Engineering Research Council (NSERC) summer research internship, working in the lab of Professor Geoffrey A. Ozin, Canada Research Chair in Materials Chemistry. His research work, which he continued in his undergraduate thesis, focused on the optical enhancement of silver infiltrated silica opal based photonic crystals, fabricated by chemical vapor deposition. In 2004, he received his Bachelor in Applied Science, specializing in the Nanoengineering.

He continued his studies at Cornell University in the department of Materials Science and Engineering, in the Colloid Based Materials Research Lab (CBMRL), under the supervision of Professor Chekesha M. Liddell. His work focused on the self-assembly and optical properties of non-spherical based colloidal crystals.

Ian earned his M. S. degree from Cornell in 2006, and completed his doctoral work in the spring of 2009.

To the *True* Assembler of “Self”-Assembled Materials

ACKNOWLEDGMENTS

In the name of God, Most Gracious, Most Merciful.

Salutations on the Prophet Muhammad, upon him be peace.

I never would have expected my path in life to lead me to Ithaca, this small college town in Upstate New York, to complete my education and to begin my research career. These past five years have been a remarkable time for me to grow both personally and as a researcher. This dissertation completes so many goals I had set for myself, some from an early age, to be an engineer, to further my studies in graduate school, to conduct research, and to study abroad. I complete my graduate studies greatly knowledgeable not only of my field of study, which I have spent this time intensely working on, but also of myself, who I am, what I want in this life, and what my direction in life should be from here onward. And for all that I have learned about myself and life, the greatest lesson I have learned is that there is still so much left to know and understand in this world and the journey of knowledge, for me, has just begun.

"Which of the favors of your Lord will you deny?" – The Holy Quran (55:13)

I am thankful to God for the guidance, mercy, blessings, and provisions he has bestowed on me throughout my endeavors to reach where I am today. I still remember, quite vividly, that momentous night as I struggled to decide which US University to attend for my graduate studies, nervously placing a check mark on the "accept" box on the Cornell admission form, and saying "Take care of me God." He did. I am grateful to him for making all that I have achieved attainable, with ease and enjoyment, and allowing my success to reach levels beyond my hopes and expectations. I am also grateful to him for allowing me to see the divine in the natural systems that I studied and endeavored to understand.

I am also happy that my personal knowledge and personal life also grew and

flourished during my time here. I was blessed, in this final year, with the time and provisions to make the sacred pilgrimage to Mecca, one of my personal life goals. The blessings and gifts from God are countless, and could go on for pages upon pages.

I am also deeply grateful to my family for their encouragement and support: my mother and father, Zalina and Taj, and my sister Alana. They were part of what made these past five years easy, enjoyable, and successful. As well, I express sincere gratitude to my graduate class for their companionship and support. My love and gratitude is also deeply owed to the Muslim community here in Ithaca, and to all my brothers and sisters in Islam who offered their sincere friendship, counsel, advice and support. I give my most sincere and deepest appreciation to Professor Chekesha Liddell for her encouragement, counsel and support over the span of my graduate career. She provided me the freedom to explore my research interests, and the support for me to flourish as a scientific and engineering researcher. Finally, I am thankful for the friendship and support of all members of the Liddell group.

And to the countless other people, too many to mention, who provided me with friendship, counsel, support and strength in some way over these past five years, I am thankful for all of you.

TABLE OF CONTENTS

BIOGRAPHICAL SKETCH.....iii

DEDICATION……...iv

ACKNOWLEDGMENTS……..v

LIST OF FIGURES…….viii

LIST OF TABLES…….....xi

CHAPTER 1- Introduction.....1

CHAPTER 2 - Convectively assembled nonspherical mushroom cap-based colloidal crystals.....13

CHAPTER 3 - Convectively assembled asymmetric dimer-based colloidal crystals..30

CHAPTER 4 - Rotator and crystalline films via self-assembly of short- bond length colloidal dimers.....50

CHAPTER 5 - Controlled monolayer structure from asymmetric dimer colloids by dip coating.....72

CHAPTER 6 - Convective assembly of three-dimensional dimer and spherocylinder based colloidal crystals.....90

CHAPTER 7 - Photonic bandgaps of three-dimensional asymmetric dimer based fcc lattices.....105

CHAPTER 8 - Photonic bandgaps of three-dimensional asymmetric dimer based monoclinic lattices.....124

LIST OF FIGURES

Figure 2.1. Mushroom cap-shaped polystyrene particles.. 17
Figure 2.2. 2D hexagonally close-packed monolayers of mushroom cap particles assembled at 55°C from a 0.05wt% suspension. 19
Figure 2.3. Surface topography of mushroom cap monolayers..... 20
Figure 2.4. Optical diffraction from a monolayer of mushroom cap particles. 22
Figure 2.5. Multilayers of mushroom cap particles via layer-by-layer convective assembly. 24
Figure 3.1. Large area monolayers of asymmetric dimers. 36
Figure 3.2. Self-assembled asymmetric dimers, oriented in-plane. 38
Figure 3.3. Self-assembled asymmetric dimers, perpendicular to substrate.. 39
Figure 3.4. Optical diffraction patterns of peanut based crystals. 41
Figure 3.5. Structures formed from asymmetric dimers as a function of concentration 44
Figure 3.6. Thickness versus particle concentration. 45
Figure 4.1. Monolayer films of pear-shaped particles..... 54
Figure 4.2. Monolayer films of spherocylinders. 55
Figure 4.3. Selected area laser diffraction patterns from monolayer films 57
Figure 4.4. Simulated equation of state for pear-shaped particles. 59
Figure 4.5. Simulated snapshot for 2D rotator structure of pear-shaped particles. 60
Figure 4.6. Radial distribution functions and bond-orientational correlation functions for 2D rotator structures of pear- and spherocylinder-shaped particles. 61
Figure 4.7. Germanium films of hollow hemi-spherocylinder units arranged 63
Figure 4.8. Simulated equation of state for spherocylinders in compression run. 64
Figure 5.1. OM and SEM images of the peanut monolayers assembled from 8vol% suspensions at decreasing withdrawal rates. 78

Figure 5.2. OM and SEM images of the pear monolayers assembled from 8vol% suspensions. 79
Figure 5.3. Colloidal structure in the transition region from out-of-plane to bilayer for peanut and pear shaped particles. 80
Figure 5.4. Operation "phase" diagrams showing film structure as a function of withdrawal rate and particle suspension volume fraction. 81
Figure 5.5. Optical microscopy of the confinement of particles at a pinned meniscus region on a horizontal surface. 83
Figure 5.6. Schematic of close packing of dimer monolayer structure with in-plane particle orientation. 85
Figure 6.1. SEM images of non-spherical particles 97
Figure 6.2. SEM images of spherocylinder based assembly. 98
Figure 6.3. SEM images of dumbbell based assemblies. 99
Figure 6.4. FIB milled cross-sections of the dimer and spherocylinder crystalline phases inverted in silica 100
Figure 6.5. Optical laser diffraction patterns for spherocylinder, dimer rotator and dimer structures. 101
Figure 7.1. Particle parameter space. 109
Figure 7.2. FCC dimer based structure, with S=0.8 and L*=0.5. Model particles are oriented in the $<11\bar{1}>$ direction. 111
Figure 7.3. Photonic band structures for FCC dimer-based crystals 113
Figure 7.4. Band structures along the X-W symmetry line for direct structures of particles with S=1 and varied L*. 115
Figure 7.5. Contour plots of Gap-to-midgap ratio versus particle symmetry (S) and L*. 116
Figure 7.6. Contour plots of minimum refractive index n_c required to open a photonic

bandgap versus particle symmetry (S) and L* 118
Figure 7.7. Gap to midgap ratio as a function of filling fraction and the refractive index contrast..... 120
Figure 8.1. Particle shape parameter space. 127
Figure 8.2. Monoclinic crystal structure..... 129
Figure 8.3. Photonic band structure, with L*=0.03 and S=0.965, producing a gap width of 4.47% between the 8^{th} and 9^{th} bands. 131
Figure 8.4. Contour plot of gap to midgap ratio versus S and L*. 132
Figure 8.5. Gap to midgap ratio as a function of filling fraction and refractive index contrast. 134
Figure 8.6. Packing geometries of particles 135
Figure 8.7. Brillouin zone for base-centered monoclinic lattice 136

LIST OF TABLES

Table 2.1. Laser diffraction data from mushroom-cap based crystals. 23

Table 3.1. Summary of optical diffraction data. 43

Table 4.1. Lattice parameters from convective assembly of pear-shaped particles. 56

Table 4.2. Lattice parameters from convective assembly of spherocylinders. 65

Table 5.1. Particle film characteristics. 81

Table 6.1. Particle synthesis parameters. 93

Table 6.2. Particle shape characteristics. 96

Table 6.3. Summary of assembly results. 102

Table 7.1. Summary of photonic gap data. 117

Table 7.2. Summary of photonic gap optimization data. 120

CHAPTER 1

INTRODUCTION

Self-assembly refers to the natural, and spontaneous, aggregation of objects into structures with regular and correlated positional and orientatonal arrangements.[1] The process was first observed at the molecular scale, where nature assembles a diversity of organic materials such as proteins and vesicles into complex arrangements for the metabolic processes of living systems. The versatility of this process, and thus its viability as a fabrication platform, extends from the molecular to millimeter scale length.[1, 2]

Employing self-assembly in nano- and micro-fabrication harnesses this phenomena to produce structured materials and devices from pre-constructed building blocks.[3] Characteristically a "bottom-up" approach, this method provides a rapid, cost-effective, and energy efficient alternative to conventional top-down methods such as photolithography, electron beam lithography, and micromachining. The process also demonstrates control over meso-sized building blocks (approximately 100nm-1μm), which are exploited for engineering structure and device features at this crucial length scale.[3] Furthermore, this length scale is inaccessible by mechanical manipulation, molecular-scale interparticle interactions, or current top-down methods; and a wider range of interactions are available, compared to the molecular scale, as controllable processes for assembly, such as capillary, electrostatic, magnetic, optical, fluidic shear, and gravitational forces.[3] Additionally, this is the signature length-scale for structural features that yield enhanced or novel electronic, optical, magnetic, mechanical, and biological properties, which extend the capacity of several size-dependent technologies such as nanofabrication, nanoparticle based lithography,

magnetic disk storage, biological sensing, chemical and biochemical analysis, DNA processing, nanomaterial growth templating, photocatalysis, and photonic crystals. [4-19]

The viability of self-assemly as a fabrication scheme, for materials and devices, depends highly on the diversity of structures it can produce, as structure has a strong effect on the ensuing properties of self-assembled materials. Spherical particles, from a range of compositions, are the primary building blocks employed to render mesoscale features in self-assembled materials.[20-23] However, spherical particle systems are highly restricted in their range of structures, limited to close-packed arrangements such as hexagonal, cubic, random hexagonal, or body-centered.[24] These lattices have been observed in both simulations[25,26] and experimental reports.[27-31] Consequently, more complex methods are necessary to extend the range of structures, accessible with spheres, such as inducing anisotropic particle-particle interactions,[32-34] applying external fields on the particle system during assembly,[35-37] assembling binary colloidal systems,[38-39] and employing more advanced assembly techniques (i.e. spin coating or surface templating).[40,41]

One approach not thoroughly explored in experiments is the self-assembly of non-spherical particles. Inducing particle shape anisotropy can significantly affect the stable packing arrangement, and lead to a broader spectrum of structures.[42-44] The thermodynamic stability of these structural phases have been confirmed in rich body of theoretical literature. Structured phase formation is driven by the maximization of the total system entropy, a summation of free volume and particle orientation terms.[45] At low system density, orientational disorder maximizes the system entropy and stabilizes the fluid phase. With an increase in system density, the particle proximities to one another decrease, restricting the free volume available per particle to sample in space. As a result, the particle system undergoes a disorder-order

transition, providing each particle with approximately the same free volume. This maximizes the free volume entropy, and thus the entropy of the system. In this unique case, each particle has translational order, but no orientational order in terms of the particle directors, and is referred to as a *plastic crystal* or *rotator structure*. At higher system densities, free volume entropy is further maximized by a perfect crystalline phase, having both translational and orientational order. The gain in free volume entropy, achived via system ordering, more than offsets the loss in orientational entropy, and maximal system entropy is maintained. Particle systems experience either a disorder-rotator-crystal or a disorder-crystal phase transition, depending on particle shape, the latter resulting for particles with high shape aspect ratios.

Phase formation is examined for particle systems undergoing step-wise compression (i.e. densification) and equilibration. At each successive step the particles are reconfigured via translations and rotations in space, and the free energy of the system calculated. Acceptance of a new configuration is based on the Metropolis criteria— of the set of new configurations, that which yields the greatest decrease in the free energy, compared to the free energy of the previous configuration, is accepted.[80] As a result, the particle system tends towards a stable equilibrium phase with each successive compression cycle. The phases are mapped out as function the particle shape aspect ratio and system density or pressure.

The phases of disc, ellipsoid, spherocylinder, and dumbbell shapes have been theoretically studied using Monte Carlo simulations, as a function of their particle shape parameters. The discs were modeled as a cylinder with diameter D and length L, and the phases mapped as a function of the ratio L/D. Ratios between 0.1 and 0.25 produced solid crystalline phases.[47] The crystalline phase consisted of layers of hexagonally packed discs, with the disc face oriented parallel to the layer, and stacked in either an AAA or ABC fashion. Ellipsoids were modeled as two hemispherical

caps of diameter D on the ends of a cylinder of diameter D and length L, and the phases mapped as a function of the L/D ratio. Ratios between zero and five produced crystalline phases consisting of hexagonally packed 2D layers stacked in an ABC fashion.[48-53] The particle directors were oriented perpendicular to the hexagonal layers. Ratios larger than five produced AAA stacking. Additional studies showed that plastic crystal phases occur for ratios less than 0.37.[58] The rotator phase consists of randomly oriented particles position on a hexagonal and RHCP lattice in 2D and 3D, respectively. Dumbbell shapes were modeled as two spheres of radius r_1 and r_2 ($r_2 \leq r_1$), with a center-to-center distance L. The particle shape was described by a symmetry parameter $S=r_2/r_1$ and normalized bond length $L^*=L/D_1$. Crystalline phases formed with L^* values greater than 0.37.[54-60] The 2D lattice had oblique symmetry with particle orientation parallel to the lattice. In the 3D case, the lattice was base-centered monoclinic, having particle orientation parallel to the 2D oblique lattices that stacked to produce the 3D structure. Both 2D and 3D rotator and crystalline phases produced in spherocylinder and dumbbell systems were demarcated by the value of $L^* \approx 0.37$, with rotator phases existing for particle shapes with L^* below this value.

Despite this rich body of theoretical literature, and the numerous experimental reports of self-assembled non-spherical based structures at the molecular and sub-millimeter scale,[1-3] examples at the mesoscale are few. As examples, polymer ellipsoids, approximately 200nm in length, produced disordered structures when assembled in a fluidic cell in the presence of heat.[61] Zeolite hexagonal shaped nanoplates approximately 150nm wide were convectively assembled into monolayers having translational order with the hexagonal faces oriented parallel to the substrate.[62] However, the quality of the crystals was significantly reduced by particle shape dispersity, and a wide orientation distribution existed for the plates.

The multilayer films from these particles were also oriented parallel to the substrate plane, however, no 3D translational order was observed. Monodisperse nickel(II) hydroxide discs approximately 84nm in diameter where assembled under shear flow and inferred by neutron diffraction analysis to have translational order in the form of ABC or AAA stacking of hexagonal layers.[63] Highly fused dumbbell shapes were observed to form rotator and crystalline phases in suspension, via analysis of the small angle x-ray scattering from the suspension volume. The phases were then confirmed in thin colloidal films formed on planar substrates.[64] Recently, disc and cylindrical shapes were shown to assemble into single crystalline phases in suspension as a function of salt concentration, however dry structures were not reported.[65]

The lack of successful methods for non-spherical assembly at the mesoscale renders their advantageous properties inaccessible. For example, non-spherical based photonic crystals theoretically show enhanced band structure properties compared with crystals with sphere bases, as well as the potential to overcome several bottle-necks. The colloidal crystal templates used for photonic crystal fabrication are assembled from either polymer or silica spheres and filled with a high index material via sol-gel infiltration or vacuum deposition techniques.[67] The polymer or silica template is removed by chemical etching to produce an inverted high refractive index structure, referred to as an inverted opal. Only pseudogaps open for dielectric spheres in an air matrix, whereas complete photonic bandgaps open for the inverted case.[66] Although the latter structure theoretically and experimentally exhibits a photonic bandgap between the 8^{th} and 9^{th} bands,[67-69] the gap width is very small, extremely sensitive to defects (i.e. closes on sphere dispersity greater than 2%) and is limited to exceedingly high refractive index materials for gap formation.[70-73] These poor band structure properties are a consequence of the shape of the particle basis. A more stable photonic bandgap remains closed between the 2^{nd} and 3^{rd} bands as a consequnce

of symmetry induced degeneracies at the W and U symmetry points of the photonic band structure.[74] Other spherical close-packing arrangements also have bandgap inhibiting symmetry induced degeneraces, for example, BCC at the P and H symmetry points and SC at the M and R symmetry points.[75]

Producing photonic crystals from non-spherical colloidal building blocks has been theoretically shown to lift the degeneracies, allowing wider and more stable photonic bandgap to form between the 2^{nd} and 3^{rd} bands,[76] for example, in the case of iron oxide dumbbells position on an FCC lattice, and oriented so as to produce a diamond like lattice.[77] Lower refractive index contrasts are required for stable gap formation, permitting photonic crystals to be fabricated from a wider range of materials.

In addition to photonic properties, mesoscale particles are suitable model systems for studying atomic scale phenomena such as phase formation, melting and freezing. Although the two characteristic scale lengths differ by approximately three orders of magnitude, the atomic and colloidal pair-potentials (Leonard-Jones and Derjaguin-Landau-Verwey-Overbeek, respectively) have similar ranges and magnitudes relative to their particle size.[78] Similar to spherical systems mimicking the phases as atomic systems (i.e. FCC, BCC, HCP), non-spherical colloids are potential model systems for studying the phases of non-spherical molecules, the simplest being small diatomic molecules such as N_2, NO and CO.[79,80]

This dissertation investigates the fabrication of non-spherical colloid based structures using the convective self-assembly technique. Monolayer and multilayer structures were produced on glass and silicon substrates, using either ambient conditions or heat. Chapters two through six describe the experimental studies conducted. Chapter seven and eight present photonic computation studies on non-spherical based photonic crystals.

In chapter two, the convective assembly technique that produced ordered 2D arrays from hemispherical cap-shaped colloids is described. Chapter three discusses the assembly of asymmetric dumbbells and control of the particle via systematically tuning the process parameters, producing different 2D packing arrangements. In chapter four, an examination of the 2D rotator and crystalline phases formed by short-bond length dimer and spherocylinder particles is given. Chapter five presents a study on the correlation of the monolayer structure with the convective assembly parameters, concentration and crystallization rate. Chapter six discusses the convective assembly technique employed to produce 3D rotator and crystalline phases, and the characterization of their structure.

The photonic band structures of asymmetric dumbbell based photonic crystals with FCC (Chapter seven) and base-centered monoclinic lattices (Chapter eight) are examined. Both structures are shown to produce wide and stable photonic bandgaps, which can be tuned by the particle shape parameters.

REFERENCES

1. Whitesides, G. M.; Grzybowski B. *Science* **2002**, 295, 2418-2421.
2. Boncheva, M.; Bruzewicz D.A.; Whitesides, G.M. *Pure Appl. Chem.* **2003**, *75*, 621.
3. M. Boncheva, G. M. Whitesides, *MRS Bull.* **2005**, *30*, 736-742.
4. Deckman, H. W.; Dunsmuir, J. H. *Appl. Phys. Lett.* **1982**, 41, 377-.
5. Haynes, C. L.; Van Duyne, R. P. *J. Phys. Chem. B* **2001**, *105*, 5599-5611.
6. Choi, D. G.; Yu, H. K.; Jang, S. G.; Yang, S. M. *J. Am. Chem. Soc.* **2004**, *126*, 7019-7025.
7. Rybczynski, J.; Ebels, U.; Giersig, M. *Colloids Surf., A.* **2003**, *219*, 1-6.
8. Goncharov, A.; Zhukov, A. A.; Bartlett, P. N.; Ghanem, M. A.; Boardman, R.; Fangohr, H.; de Groot, P. A. J. *J. Magn. Magn. Mater.* **2005**, *286*, 1-4.
9. Haes, A. J.; Hall, W. P.; Chang, L.; Klein, W. L.; van Duyne, R. P. *Nano Lett.* **2004**, *4*, 1029-1034.
10. Haes, A. J.; Chang, L.; Klein, W. L.; van Duyne, R. P. *J. Am. Chem. Soc.* **2005**, *127*, 2264-2271.
11. Chiu, D. T.; Wilson, C. F.; Ryttsen, F.; Stromberg, A.; Farre, C.; Karlsson, A.; Nordholm, S.; Gaggar, A.; Modi, B. P.; Moscho, A.; Garza-Lopez, R. A.; Orwar, O.; Zare, R. N. *Science* **1999**, *283*, 1892-1895.
12. Grosvenor, A. L.; Feltus, A.; Conover, R. C.; Daunert, S.; Anderson K. W. *Anal. Chem.* **2000**, *72*, 2590-2594.
13. Cooper, J. M. *Trends Biotechnol.* **1999**, *17*, 226-230.
14. Grzybowski, B. A.; Haag, R.; Bowden, N.; Whitesides, G. M. *Anal. Chem.* **1998**, *70*, 4645-4652.
15. Kaji, N.; Tezuka, Y.; Takamura, Y.; Ueda, M.; Nishimoto, T.; Nakanishi, H.; Horiike, Y.; Baba, Y. *Anal. Chem.* **2004**, *76*, 15-22.

16. Kempa, K.; Kimball, B.; Rybczynski, J.; Huang, Z. P.; Wu, P. F.; Steeves, D.; Sennett, M.; Giersig, M.; Rao, D.; Carnahan, D. L.; Wang, D. Z.; Lao, J. Y.; Li, W. Z.; Ren, Z. F. *Nano Lett.* **2003**, *3*, 13-18.
17. Rybczynski, J.; Banerjee, D.; Kosiorek, A.; Giersig, M.; Ren, Z. F. *Nano Lett.* **2004**, *4*, 2037-2040.
18. Gu, Z.-Z.; Fujishima, A.; Sato, O. *Angew. Chem. Int. Ed.* **2002**, *41*, 2067-2070
19. Birner, A.; Wehrspohn, R. B.; Gosele, U. M.; Busch, K. *Adv. Mater.* **2001**, *13*, 377-388.
20. Garcia-Santamaria, F.; Salgueirino-Maceira, V.; Lopez, C.; Liz-Marzan, L. M. *Langmuir* **2002**, *18*, 4519.
21. Gu, Z. Z.; Fujishima, A.; Sato, O. *Chem. Mater.* **2002**, *14*, 760.
22. Stein, A.; Schroden, R. C. *Curr. Opin. Solid State Mater. Sci.* **2001**, *5*, 553.
23. Meseguer, F.; Blanco, A.; Miguez, H.; Garcia-Santamaria, F.; Ibisate, M.; Lopez, C. *Colloids Surf.* **2002**, *202*, 281.
24. Russel, W. B. *Nature* **2003**, *421*, 490-491.
25. Schmidt, M.; Lowen, H. *Phys. Rev. Lett.* **1996**, *76*, 4552-4555.
26. Zangi, R.; Rice, S. A. *Phys. Rev. E* **2000**, *61*, 660-670.
27. Pieranski, P. *Contemp. Phys.* **1983**, *24*, 25.
28. Xia, Y. N.; Gates, B.; Yin, Y. D.; Lu, Y. Adv. Mater. **2000**, *12*, 693-713.
29. Jiang, P.; Bertone, J. F.; Hwang, K. S.; Colvin, V. L.; *Chem. Mater.* **1999**, *11*, 2132-2140.
30. Norris, D. J.; Arlinghaus, E. G.; Meng, L.; Heiny, R.; Scriven L. E. *Adv. Mater.* **2004***, 16*, 1393 -1399.
31. Meng, L.; Wei, H.; Nagel, A.; Wiley, B. J.; Scriven, L. E.; Norris, D. J. *Nano Lett.* **2006**, *6*, 2249–2253.
32. Zhang, Z.; Glotzer S. C. *Nano Lett.* **2004**, *4*, 1407–1413.

33. Zhang, Z.; Keys, A. S.; Chen, T.; Glotzer, S. C. *Langmuir*, **2005**, *21* (25), 11547–11551

34. Gangwal, S.; Cayre, O. J.; Velev, O. D. *Langmuir* **2008**, *24*, 13312-13320.

35. Yethiraj, A; van Blaaderen, A. *Nature* **2003**, *421*, 513-517.

36. Hynninen, A.-P. Dijkstra, M. *Phys. Rev. Lett.* **2005**, *94*, 138303-138306.

37. Yethiraj, A.; Thijssen, J. H. J.; Wouterse, A.; van Blaaderen A. *Adv. Mater.* **2004**, *16*, 596-600.

38. Leunissen, M. E.; Christova, C. G.; Hynninen, A.-P.; C. P. Royall, ; Campbell, A. I.; Imhof, A.; Dijkstra, M.; van Roij, R.; van Blaaderen, A. *Nature* **2005**, *437*, 235-240.

39. Hynninen, A.-P.; Thijssen, J. H. J.; Vermolen, E. C. M.; Dijkstra, M.; van Blaaderen, A. *Nat. Mater.* **2007**, *6*, 202-205.

40. Jiang, P.; McFarland M. J. *J. Am. Chem. Soc.* **2004**, *126*, 13778–13786.

41. García-Santamaría , F.; Miyazaki , H.T.; Urquía , A.; Ibisate M., ; Belmonte, M.; Shinya , N.; Meseguer , F.; López C. *Adv. Mater. 2002*, *14*, 1144 – 1147.

42. Glotzer, S. C. *Science* **2004**, *306*, 419-420.

43. Glotzer, S. C.; Solomon M. J. *Nat. Mater.* **2007**, *6*, 557-562.

44. van Blaaderen, A. *Nature* **2006**, *439*, 545-546.

45. Berry, R. S.; Rice, S. A. ; Ross, J. *Physical Chemistry, 2nd ed.* Oxford University Press: New York, **2000**.

46. Scott, T. A. *Phys. Rev.* **1976**, *27*, 89.

47. Veerman, J. A. C.; Frenkel, D. *Phys. Rev. A.* **1992**, *45*, 5632-5648.

48. Hentschke, R.; Taylor, M. P.; Herzfeld, J. *Phys. Rev. A.* **1989**, *40*, 1678-1680

49. Taylor, M. P.; Hentschke, R.; Herzfeld, J. *Phys. Rev. Lett.* **1989**, *62*, 800-803.

50. Stroobants, A.; Lekkerkerker, H. N. W.; Frenkel, D. *Phys. Rev. A.* **1986**, *57*, 1452-1455.

51. Stroobants, A.; Lekkerkerker, H. N. W.; Frenkel, D. *Phys. Rev. A.* **1987**, *36*, 2929 - 2945.

52. Veerman, J. A. C.; Frenkel, D. *Phys. Rev. A. 1990*, *41*, 3237-3244.

53. Veerman, J. A. C.; Frenkel, D. *Phys. Rev. A.* **1991**, *43*, 4334-4343.

54. Wojciechowski, K. W. *Phys. Rev. B.* **1992**, *46*, 26–39.

55. Vega, C.; Paras, E. P. A.; Monson, P. A. *J. Chem. Phys.* **1992**, *96*, 9060–9072.

56. Marechal, M.; Dijkstra, M. *Phys. Rev. E* **2008**, *77*, 061405-061414.

57. Branka, A. C.; Wojciechowski, K. W. *Phys. Rev. Lett.* **1983**, *50*, 846–849.

58. Vega, C.; Monson P. A. *J. Chem. Phys.* **1997**, *107*, 2696-2697.

59. Bolhuis, P.; Frenkel D. *J. Chem. Phys.* **1997**, *106*, 666–687.

60. Gay, S. C.; Beale, P. D.; Rainwater, J. C. *Int. J. Thermophys*, **1998**, *19*, 1535.

61. Lu, Y.; Yin, Y.; Li, Z.-Y.; Xia, Y. *Langmuir* **2002**, *18*, 7722–7727.

62. Lee, J. A.; Meng, L.; Norris, D. J.; Scriven, L. E.; Tsapatsis M. *Langmuir* **2006**, *22*, 5217–5219.

63. Brown, A. B. D.; Rennie A. R. *Phys. Rev. E* **2000**, *62*, 851-862.

64. Mock, E. B.; Zukoski, C. F. *Langmuir*, **2007**, *23* , pp 8760–8771

65. Badaire, S.; Cottin-Bizonne, C.; Woody, J. W.; Yang, A.; Stroock, A. D. *J. Amer. Chem. Soc*. **2007**, *129*, 40-41.

66. Moroz, A.; Sommers, C. *J. Phys.: Condens. Matter* **1999**, *11*, 997–1008.

67. Norris, D. J.; Vlasov Y. A. *Adv. Mater.* **2001**, *13*, 371-376.

68. Vlasov, Y. A.; Bo, X.-Z.; Sturm, J. C.; Norris, D. J. *Nature* **2001**, *414*, 289.

69. Blanco, A.; Chomski, E.; Grabtchak, S.; Ibisate, M.; John, S.; Leonard, S. W.; Lopez, C.; Meseguer, F.; Miguez, H.; Mondia, J. P.; Ozin, G. A.; Toader, O.; van Driel, H. M. *Nature* **2000**, *405*, 437-440.

70. Li, Z.-Y.; Zhang Z.-Q. *Phys. Rev. B* **2000**, *62*, 1516.

71. Vlasov, Y. A.; Astratov, V. N.; Baryshev, A. V.; Kaplyanskii, A. A.; Karimov, O. Z.; Limonov, M. F. *Phys. Rev. E* **2000**, *61*, 5784.

72. Wong, S.; Kitaev, V.; Ozin G. A. *J. Am. Chem. Soc.*, **2003**, *125*, 15589–15598.

73. Meseguer, F.; Fenollosac R. *J. Mater. Chem.*, **2005**, *15*, 4577–4580

74. Ho, K. M.; Chan, C. T.; Soukoulis C. M. *Phys. Rev. Lett.* **1990**, *65*, 3152-3155.

75. Li, Z.-Y.; Wang, J.; Gu, B.-Y. *Phys. Rev. B* **1998**, *58*, 3721 – 3729.

76. Yablonovitch, E.; Gmitter, T. J.; Leung, K. M. *Phys. Rev. Lett.* **1991,** *67*, 2295-2298.

77. Xia, Y.; Gates, B.; Li, Z.-Y. *Adv. Mater.* **2001**, *13*, 409-413.

78. Glotzer, S. C.; Solomon, M. J.; Kotov, N. A. *AIChE J.* **2004**, *50*, 2978-2985.

79. Manzheliim, V. G.; Freiman, Y. A. *Physics of Cryocrystals*, AIP Press: New York, **1997**.

80. Frenkel, D.; Smit, B. *Understanding Molecular Simulation. From Algorithms to Applications, 2nd ed.;* Academic Press: New York, **2002**.

CHAPTER 2

CONVECTIVELY ASSEMBLED NONSPHERICAL MUSHROOM CAP-BASED COLLOIDAL CRYSTALS*

Abstract

Monolayers from mushroom cap shaped polymer colloids were fabrication by a vertical substrate deposition technique. As confirmed by SEM and autocorrelation analysis, the monolayers show long-range hexagonal packing with particle orientational freedom restricted to either "heads up" or "heads down" alignment with respect to the substrate. The monolayers are modeled as a 2D diffraction grating and were studied with selected area laser diffraction. The stacking of ordered monolayers into the third dimension was achieved via layer-by-layer deposition. Convective assembly is shown as a viable approach to the large-scale crystallization of monodisperse non-spherical colloids.

Introduction

Nonspherical based colloidal crystals have been desired as photonic materials due to the enhanced light control provided by the anisotropy of the building blocks.[1, 2] For example, nonspherical building blocks were found to lift the symmetry induced degeneracy of photonic bands, leading to complete photonic band gaps in face-centered cubic and other simple lattices.[1, 3-5] The self-assembly of nonspherical colloidal particles into ordered arrays also has applications in low cost, large area micro- and nanofabrication,[6] for example, in micro-lens arrays[7] and coatings for anti-

* *Published: I. D. Hosein, C. M. Liddell, "Convectively assembled nonspherical mushroom cap-based colloidal crystals",* Langmuir*, **2007**, 23 (17), pp 8810–8814. – Reproduced by permission of The American Chemical Society*
http://pubs.acs.org/doi/abs/10.1021/la700865t

reflective[8] or anti-fouling applications. A variety of monodisperse nonspherical colloids have been prepared including ellipsoids,[9] snowman-like,[10] corpuscle-shaped,[11] and tetrahedra[12] polymer particles, as well as inorganic rods, cubes, peanuts,[13-27] and dimers.[16, 17] Computational studies suggest that ordered structures should ultimately be experimentally accessible for disc, rod, ellipsoidal, and spherocylinder colloidal shapes.[18-21] Particle sizes within the range from 100nm to ~1μm are of interest for their interaction with visible and near infrared light. However, self-assembling nonspherical particles of these sizes remains challenging. Specifically, control over particle orientation during the assembly process and in the final crystal has been difficult to achieve.[22]

Crystallization experiments to date using nonspherical particles often produced liquid crystalline phases. The columnar structure was observed in colloidal disc sediments[6, 23] and for discs under shear.[24] Sediments of PMMA rods formed either nematic or smectic phases.[25] Such structures are difficult to extract from liquid media without disturbing the order. Few attempts have been made to self-assemble mesoscale nonspherical colloids into dry films employing the crystallization methods commonly applied for spheres.[9, 26-27] Using capillary interactions, unusual colloidal metal plates— i.e., hexagons with central holes, snowflake-like, and elongated hexagons ~10μm in longest dimension— were self-assembled into multilayered stacks of ordered hexagonal columnar structures.[26] The faces and sides of the lithographically defined plates were functionalized with complementary self-assembled which programmed the specific alignment of particles with respect to each other. Attempts to crystallize 200nm polystyrene spheroids with aspect ratio ~1.2 in a microfluidic confinement cell resulted only in thick disordered films due to the loss of orientational order.[9] Recently, Lee et al. applied a convective assembly technique to hexagonal zeolite plates.[27] Orientational order with plates aligned parallel to the

substrate was achieved in monolayer films, but positional (translational) order was limited to small regions due to the size and shape polydispersity of the zeolite particles.

Here, we report the formation of 2D and 3D ordered colloidal crystals by convective assembly of monodisperse micron sized mushroom cap-shaped colloids. Long range hexagonal close-packed ordered arrays were obtained due to the monodispersity and compatibility of the particle shape (circular cross-section) with the deposition technique. The ordering was explained not only by thermodynamic considerations, such as free energy minimization, but also by the restriction of the particle orientational freedom at the suspension drying front. The fabrication of multilayered films was achieved through layer-by-layer deposition of ordered 2D films.

Experimental Section

The mushroom cap-shaped polystyrene (PS) particles were purchased from Interfacial Dynamics Corporation and used as received. The particles could also be synthesized following procedures reported in the literature by Okubo et al.[29-32] All particle suspensions were prepared in 18.2MΩ deionized water. 25-50μL of a 4.2 wt% suspension of the mushroom cap-shaped PS particles were added to 2mL of water. The suspension was placed in a vial and sonicated for 1 minute to ensure complete dispersion of the particles. The vial was cleaned with water and ethanol, and dried with dry nitrogen prior to use. Silicon and glass substrates were soaked in freshly prepared piranha solution (H_2SO_4 and H_2O_2, 30 wt% in a 2:1 v/v mixture) for 30 minutes, rinsed several times with water, and dried under a nitrogen flow. Glass substrates were further treated with oxygen plasma before use. Substrates were dipped vertically into the particle solution and were held in place by two binders clips. The

setup was placed in an oven at 45°C, 55°C or 65°C. Samples were left overnight until the liquid evaporated. Scotch tape was used to anchor the clips, in order to ensure that the substrate position would be stable when the set up was transferred into- and out of the oven. To prepare multilayers, the deposition process was repeated on the same substrate. The monolayer films were fumed with tetraethylorthosilicate (TEOS) at 50°C for 40 minutes to ensure particle adhesion to the substrate prior to subsequent depositions.[28] The films were sputtered with gold before being characterized with SEM. The SEM images were obtained with an LEO 1550 field emission scanning electron microscope. AFM images were obtained with a Nanonics (Jerusalem, Israel) MultiView 1000 system. Selected area laser diffraction was conducted using a Renishaw inVia Raman system with a Leica DMLB optical microscope and a 488nm, 20mW laser. Diffraction images were taken with a digital camera (Angstrom Sun Tech., Acton MA, Model CFM-USB-3) mounted under the sample.

Results & Discussion

Perspectives of the nonspherical colloid morphology are provided in Figure 2.1, illustrating the resemblance of the particle shape to the cap of a mushroom. Similar shapes have been formed via the collapse of polymer core-shell particles during seeded polymerization in the dynamic swelling method.[29, 30] The shell is highly crosslinked compared to the core and the collapse is induced by the subsequent evaporation of unpolymerized DVB and toluene in the particle. Due to the hydrophobic shell, the penetration rate of water into the core is much slower than the rate of evaporation of DVB and toluene.[31] Consequently, the hydrostatic pressure causes the shell to cave in, producing the cavity.

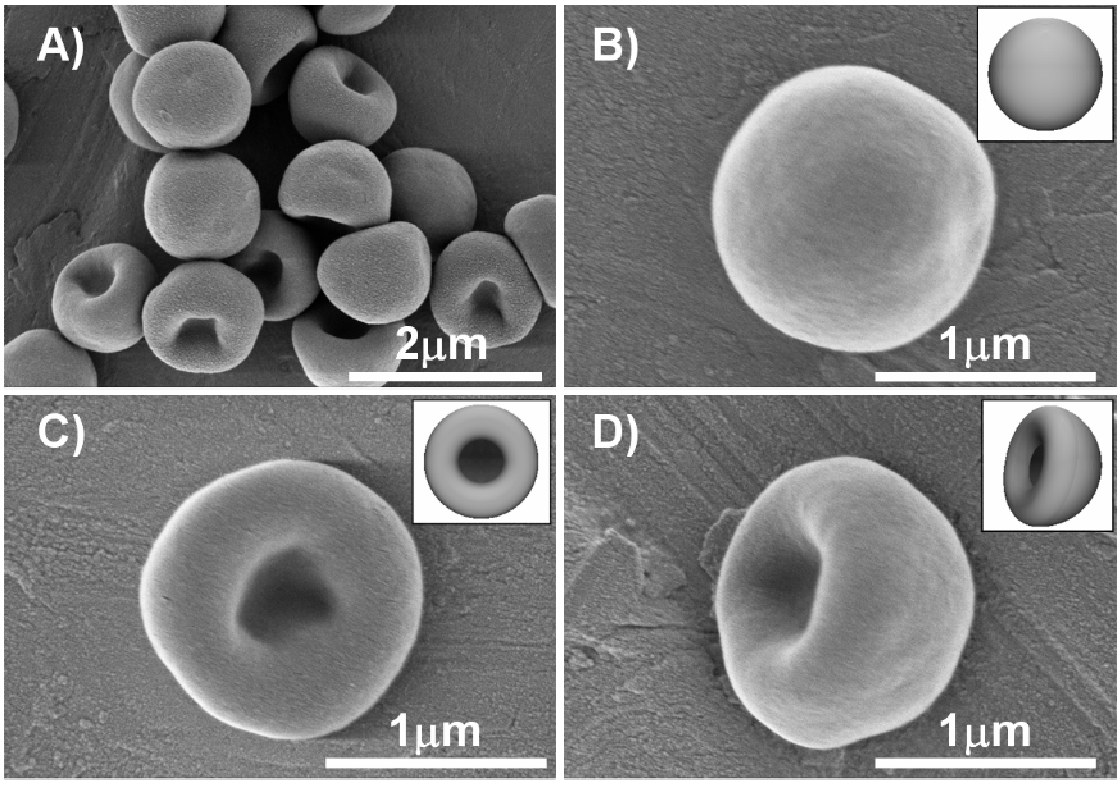

Figure 2.1. Mushroom cap-shaped polystyrene particles. Particle alignment on the substrate is (a) heads up, (b) heads down, and (c) sideways. Insets show 3D models of the particle shape. (d) Cross-section of thin film deposited from 0.1 wt% suspension of particles assembled at 65°C.

The mushroom-cap shaped particles employed in the present study measure 1.2μm in outer diameter (CV = 4.2%), 890nm in height, and ~450nm in cavity width. The morphology is similar to that of red blood cells,[29-32] with the exception that blood cells are larger in size (7-8μm) and thinner in shape (i.e. higher aspect ratio). A simple model for the mushroom cap is the union between a hemisphere and a torus (Figure1, insets). The overall shape polydispersity was less that 5%, although variations in particle morphology were observed, such as in cavity depth, square or ovular cavity shape, as well as pinched closed cavities or dented caps. The particle orientations were classified as either "heads up", "heads down", or "sideways", corresponding respectively to the cavity facing downward (Figure 2.1a), upward

(Figure 1b), or at oblique angles (Figure 1c) to the substrate.

The particles were convectively assembled from aqueous solution onto clean hydrophilic silicon substrates using a heat-assisted vertical deposition technique[33] . The degree of order was examined as a function of particle concentration (ϕ) in solution. Relatively high particle concentrations, $\phi > 0.1$ wt%, produced thick disordered films of randomly oriented particles, as shown in Figure 1d. The films also exhibited high surface roughness and non-uniform thickness. For lower particle concentrations, between 0.05 wt% and 0.1 wt%, the films exhibited large scale order in monolayer regions. Films thicker than one layer could also form for this concentration range, however, the order was typically disrupted in the multilayer regions. Further reducing the concentration to $\phi \leq 0.05$ wt% exclusively produced monolayers with large single crystal domains of 2D ordered close-packing, up to 100μm wide. The monolayers, formed on a silicon substrate at 55°C from 0.05 wt% suspensions, are presented in Figure 2.2(a-c). When the assembly temperature was increased to 65°C a decrease in the domain size from 100μm to 80μm was observed. The decrease in grain size may be due to the increased number of small nuclei of ordered particles (i.e., nucleation sites) in the crystallization region. This is a result of the increased particle flux at higher temperatures and the limited time for particle incorporation into a single growing nucleus. Crystal bands approximately 300μm wide consisting of the domains (unresolved) are shown on a glass vial wall and silicon substrate in Figure 2.2d and 2.2e, respectively. The presence of bands is common in convectively assembled monolayers, since the solvent contact line often becomes pinned to the substrate. Bands form due to the stick-and-slip motion of the meniscus as it recedes.[27,34] The differences in surface wetting of the suspension medium on the substrate versus the monolayer film contribute to the effect.[35] Slippage occurs when gravitational effects exceed the pinning force. The low suspension concentration also

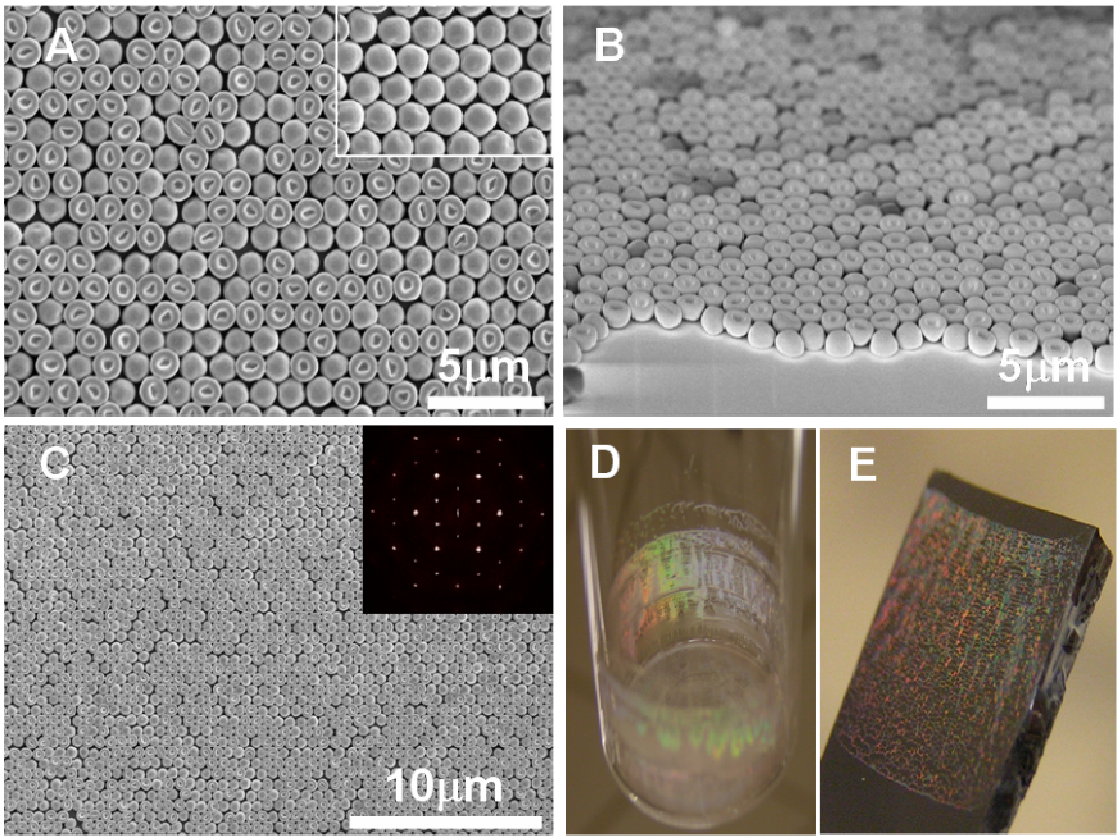

Figure 2.2. 2D hexagonally close-packed monolayers of mushroom cap particles assembled at 55°C from a 0.05wt% suspension. (a) Top view at high magnification. Particles in either heads up or heads down orientations. Inset shows local region with both positional and heads up orientational order. (b) Cross-section view of monolayer. (c) Top view at low magnification showing long range order. Inset shows fast Fourier transform of (c). Iridescent films of mushroom cap-shaped particles assembled on (d) glass vial wall and (e) silicon substrate.

leads to local regions at the drying front with insufficient particle flux so that gaps open as the meniscus recedes. The monolayer films displayed colorful iridescence. The fast Fourier transforms of the SEM images (inset Figure 2.2c) indicated well defined 6-fold symmetry. Spots even beyond the fourth order could be clearly resolved, evidence of the high quality 2D hexagonal packing. The particle orientation in the monolayers was distributed nearly equally between the heads up and heads down configurations. The alignment of the particles into heads up versus heads down orientation may depend on substrate-particle and particle-liquid-vapor interactions.

However, in deionized water with a bare substrate surface, the interactions are not significant enough to force assembly exclusively into one of the orientations. Thus, random heads up/down orientations were observed in the monolayers. Future studies may entail varying the particle-substrate and particle-liquid-vapor interface interactions with polyelectrolytes and surfactants to explore the possibility of even more precise control of the orientation.

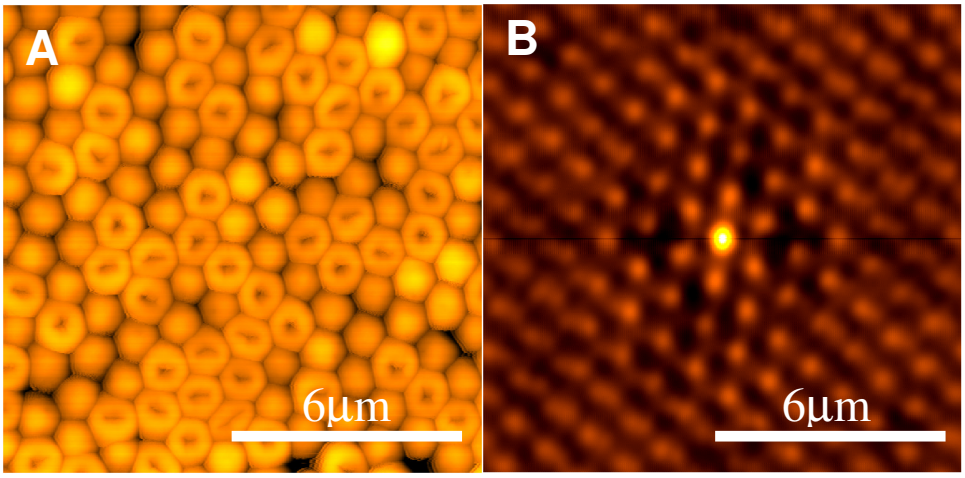

Figure 2.3. Surface topography of mushroom cap monolayers. (a) 15×15µm^2 AFM image of the monolayer surface. (b) Auto-correlation of (a) showing a 1.18µm lattice spacing.

Figure 2.3a shows the surface topography of the crystalline monolayer obtained using atomic force microscopy (AFM). The image shows a dependence of the packing distance on the orientation of nearest neighbors. Regions with mixed orientation generated pores in the monolayer, whereas regions with the same orientation maintained a consistent packing. From the autocorrelation function (Figure 2.3b) of the AFM image, the calculated lattice constant was 1.19µm, which is in good agreement with the corresponding lattice constant (1.17µm) measured by SEM. The autocorrelation also shows the hexagonal symmetry of the crystal structure and reveals the high degree of positional order present in the monolayer, even with particle orientation mixed between heads-up and heads-down.

The monolayers were also characterized using laser diffraction. Figure 2.4a shows the diffraction of a monochromatic 488nm laser from the particle film formed on a glass substrate (0.05wt%, 55°). When light is incident on the surface, the monolayer operates as a 2D diffraction grating of wavelength comparable to the spacing between rows of particle centers. Light is coherently scattered from the film at discrete angles and directions. For normal incidence the diffraction pattern was hexagonally symmetric and reproduced the symmetry of the 2D array. The pattern consisted of several diffraction orders which encircled the incident transmitted spot. The symmetry of the pattern is consistent with diffraction patterns obtain from spherical based 2D hexagonal arrays.[36-39] Figure 2.4b shows a magnified image of the first order diffraction. Each spot in the diffraction pattern can be associated with a point in the reciprocal lattice of the mushroom-cap based crystal structure. Vectors from the center of the diffraction pattern to points in it correspond to reciprocal lattice vectors with lines of particles in the crystal structure having orientation perpendicular to the vector directions.[36] The line spacing consistent with the location of each diffraction spot was determined. For example, Figure 4c indicates two sets of particle lines from which diffraction was observed. The first order peaks shown in Figure 4b, correspond to the (1,1) lines of the crystal with spacing d_{11}. The diffraction angles were predicted from the grating equation:[40]

$$\frac{\lambda}{d_{hk}} = \sin\theta - \sin\theta_i \qquad (1)$$

where λ is the wavelength, d_{hk} is the line spacing with miller indices (h,k), θ is the diffraction angle of the mth order and θ_i is the angle of incident light. Both angles are measured from the surface normal. For light at normal incidence, equation (1) simplifies to the von Laue relation,

$$\frac{\lambda}{d_{hk}} = \sin\theta \qquad (2)$$

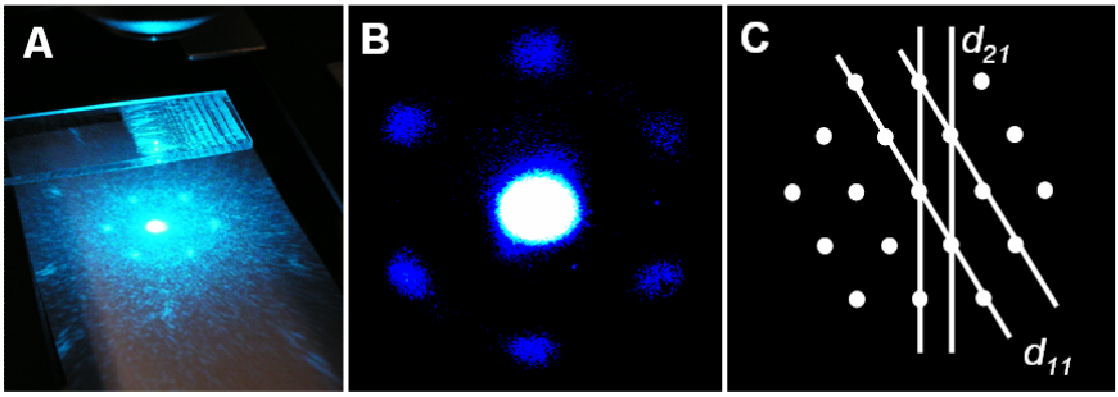

Figure 2.4. Optical diffraction from a monolayer of mushroom cap particles showing (a) several diffraction orders and (b) first order diffraction spots magnified. (c) A schematic of the real space lattice and line spacings from which diffraction was observed [not scaled with (b)].

Table 2.1 gives the measured and calculated diffraction angles. The diffraction angles of 28.5° and 66.7° correspond to diffraction from the same set of lines in the crystal, but are first and second order reflections, respectively. The predicted diffraction angles were calculated using a lattice with unmixed orientational order (i.e., a fixed lattice parameter of 1.2μm). The experimentally determined lattice constant of 1.18μm was found from the diffraction angles associated with the first order spots (28.5°) and from a line spacing of $(\sqrt{3}/2)D$, where D is the diameter of the particle. This value of the lattice constant (representative of an average over many line spacings, since the laser beam samples approximately a 100μm diameter area) is more characteristic of a film with mixed rather than unmixed orientation. This is consistent with the actual particle orientational composition of the films observed in the SEM images. The optical diffraction images indicated that monolayers with mixed orientation maintained the strong coherent scattering properties associated with 2D crystals.

Figure 2.5 illustrates the multilayers fabricated using layer-by-layer deposition with 0.05 wt% suspensions at 65°C. Each sequential dip and controlled drying cycle of the substrate typically led to the addition of one ordered layer. Fabricating

Table 2.1. Laser diffraction data from mushroom-cap based crystals.

Wavelength (nm)	Miller Indices	Line Spacing	Diffraction Angle (Calcd.)	Diffraction Angle (Exptl)
488	(0,1), (0,-1) (1,0), (-1,0) (1,1), (-1,-1)	$(\sqrt{3}/2)D$	28.0°	28.5°
488	(1,2), (2,1) (1,-1), (-1,1) (-1,-2), (-2,-1)	$(1/2)D$	54.4°	53.6°
488	(0,2), (0,-2) (2,0), (-2,0), (2,2), (-2,-2)	$(\sqrt{3}/2)D$	69.9°	66.7°

multilayers by sequential deposition of monolayers allowed each layer to retain the heads up/down alignment, producing a 3D film with a higher degree of order than a film grown from a higher suspension concentration. In contrast to monolayer deposition, for multilayers assembly does not occur in the meniscus region with height comparable to the particle diameter. Additionally, to form multilayers in a single deposition the temperature would have to be decreased to slow the kinetics of crystallization. Settling effects would then be more likely to prevent film formation and ordering for these micron sized particles. Preferential alignment with ~85% of the particles in the heads down orientation was observed for the layers added on top of the first (percentage estimated from SEM images by considering the orientations of over 2000 particles). This may be explained by the curved cap head sitting stably in the lowest lying positions, i.e., the interstitial pore spaces between particles in the layer below. In contrast to Figure 2.1d, which shows glassy multilayer films deposited in one step at high particle concentration, Figure 2.5 confirms that ordered multilayers resulted from layer-by-layer deposition at low particle concentration. The nonspherical assemblies had structural features similar to sphere based polycrystalline colloidal crystals, such as single crystal domains separated by grain boundaries as well

as the presence of point defects. Some disorder in the cross-sections is associated with the rough fracture surface produced when using a diamond scribe to cleave the substrate.

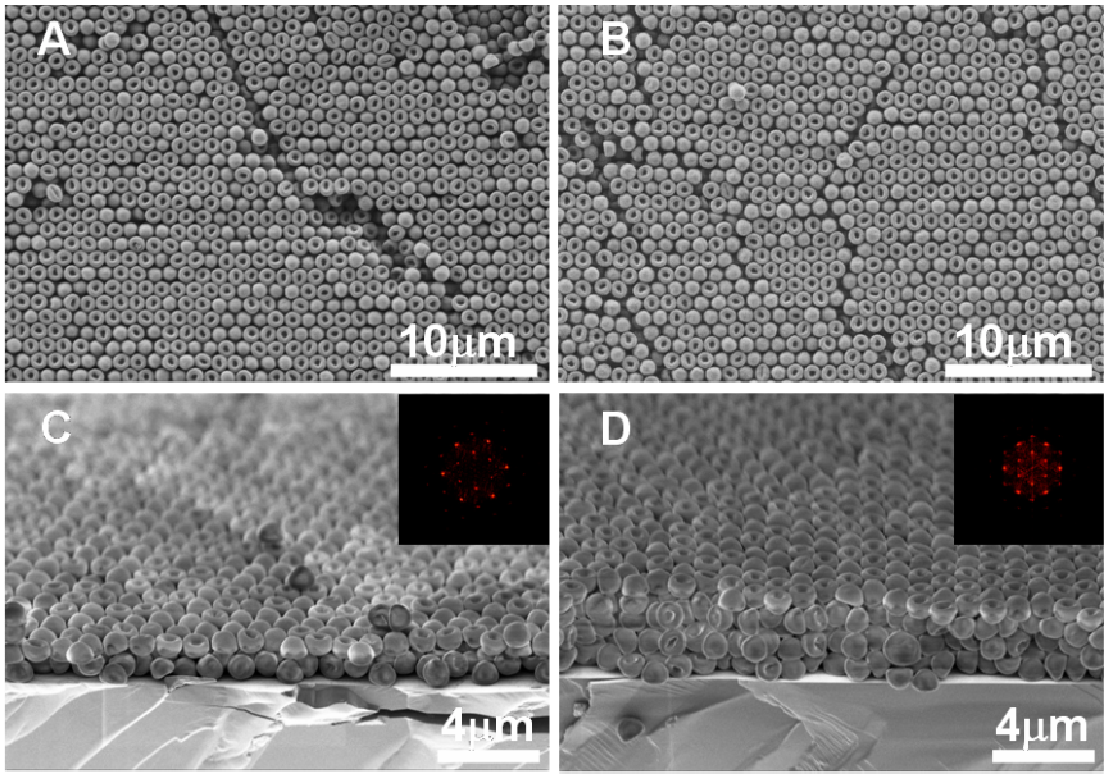

Figure 2.5. Multilayers of mushroom cap particles via layer-by-layer convective assembly. (a) Long range hexagonally ordered second layer, with registry preserved across the crack. (b) Top surface of a 4-layer thick film. Cross-sections of (c) 2-layer and (d) 4-layer mushroom cap particle assemblies. Insets show fast Fourier transform of top layer, confirming that sequentially deposited layers maintained highly ordered packing.

Crystallization under nonequilibrium convective assembly conditions is influenced by a variety of factors including the— (1) Reduction in the free energy of the condensed matter system. An increase in entropy is associated with the free volume gained as particles close-pack on a lattice; (2) Minimization of the surface free energy of the drying liquid film. The related confining force of the meniscus is

often treated equivalently to a confining wall, plate or wedge; and (3) Attractive capillary forces on the partially immersed particles when the water layer thickness becomes smaller than the particle diameter.[41, 42]

In the present convective assembly process,[43-46] the colloidal crystal of mushroom cap-shaped particles formed at the drying front of a low volume fraction suspension. The rapid evaporation of the liquid at the meniscus, induced convective transport from the bulk suspension and concentrated the particles into the drying front region.[43] The action of confinement by the meniscus and surface tension has the effect of inducing and maintaining particle orientation parallel to the substrate for certain classes of nonspherical particles. The mushroom cap-shaped particles were forced to lie flat with cavity parallel to the substrate (heads up or heads down, as the meniscus height approached the particle size) and were essentially prohibited from other orientations. The particles then behaved similarly to spheres, assembling in two dimensions into the minimum free energy hexagonal structure. The mushroom caps aided by the capillary forces between particles, assumed close-packed configurations for particle orientations parallel to the substrate. The particle concentration must be sufficiently low so that physical particle-particle interactions do not inhibit orientational ordering and lead to glassy films. Random heads up and heads down orientations did not significantly affect the long range positional order since the difference in lattice constant between similarly and oppositely aligned nearest neighbors was small. Layers forming on top of an existing film were subject to the templating effect of the prior layer as well as to the combination of the effects discussed above.

The previous principles may be generalized to the class of particles with low aspect ratio which will exhibit 1-, 2-, 3-, 4- or 6-fold rotationally symmetric projections on the substrate plane when confined by the meniscus. Examples of

nonspherical colloidal particles for which convective assembly should produce ordered films in this scheme include oblate ellipsoids, discs, cubes, and hexagonal plates. Our findings suggest the goal of achieving ordered crystals from a rich variety of complex colloids is within reach.

Conclusion

In summary, the self-assembly of micrometer sized mushroom cap-shaped colloids was demonstrated for the first time. Through a simple heat assisted convective assembly technique, the particles formed long range crystalline domains with 2D hexagonal close-packing. The monolayers showed well-defined diffraction properties for light in the visible regime. The meniscus at the drying front facilitates both the reduction in orientational configurations (leading to alignment) and the self-assembly into translational ordered arrays. 3D structures were fabricated using layer-by-layer deposition of successive monolayers.

REFERENCES

1. Xia, Y.; Gates, B.; Li, Z.-Y. *Adv. Mater.* **2001**, *13*, 409-413.
2. Noda, S.; Yokoyama, M.; Imada, M.; Chutinan, A.; Mochizuki, M. *Science* **2001**, *293*, 1123-1125.
3. Leung, K. M.; Liu, Y. F. *Phys. Rev. Lett.* **1990**, *65*, 2646-2649.
4. Li, Z.; Wang, J.; Gu, B.-Y. *Phys. Rev. B* **1998**, *58*, 3721-3729.
5. Ngo, T. T.; Ghebrebrhan, M.; Joannopoulos, J. D.; Liddell, C. M. *Appl. Phys. Lett.* **2006**, *88*, 241920-1.
6. Brown, A. B. D.; Ferrero, C.; Narayanan, T; Rennie, A. R. *Eur. Phys. J. B* **1998**, *11*, 481-489.
7. Lu, Y.; Yin, Y.; Xia, Y. *Adv. Mater.* **2001**, *13*, 34-37.
8. Prevo, B. G.; Hwang, Y.; Velev, O. D. *Chem. Mater.* **2005**, *17*, 3642-3651.
9. Lu, Y.; Yin, Y.; Li, Z.-Y.; Xia, Y. *Langmuir* **2002**, *18*, 7722-7727.
10. Okubo, M.; Katsuta, Y.; Matsumoto, T. *J. Polym. Sci.: Polym. Lett. Ed.* **1982**, *20*, 45.
11. Okubo, M.; Minami, H. *Macromol. Symp.* **2000**, *150*, 201.
12. Manoharan, V. N.; Imhof, A.; Pine, D. J. *Adv. Mater.* **2001**, *13*, 447-450.
13. Sugimoto, T.; Itoh, H.; Mochida, T. *J. Colloid Inter. Sci.* **1998**, *205*, 42-52.
14. Sugimoto, T.; Khan, M. M.; Muramatsu, A. *Colloid Surf. A: Physiochem Eng. Aspects*, **1993**, *70*, 167-169.
15. Matijevic, E. *Langmuir* **1994**, *10*, 8-16.
16. Liddell, C. M.; Summers, C. J. *Adv. Mater.* **2003**, *15*, 1715-1719.
17. Van Kats, C. M.; Johnson, P. M.; van den Meerakker, J. E. A. M.; van Blaaderen, A. *Langmuir* **2004**, *20*, 11201-11207.
18. Trizac, E.; Bocquet, L.; Agra, R.; Weis, J.-J; Aubouy, M. *J. Phys. C* **2002**, *14*, 9339-9352.

19. Savenko, S. V. ; Dijkstra, M. *Phys. Rev. E* **2004**, *70*, 051401-7.

20. Marko, J. F. *Phys. Rev. A,* **1989**, *39*, 2050-2062.

21. Stroobants, A.; Lekkerkerker, H. N. W.; Frenkel, D. *Phys. Rev. A.* **1987**, *36*, 2929-2945.

22. Xia, Y.; Fudouzi, H.; Lu, Y.; Yin Y. in *Colloids and Colloid Assemblies* (Ed: F. Caruso), Wiley-VCH, Weinheim, Germany **2004**, Ch. 9.

23. Van der Kooij, F. A.; Lekkerkerker, H. N. W. *J. Phys. Chem. B* **1998**, *102*, 7829-7832.

24. Brown, A. B. D. *Phys. Rev. E.* **2000**, *62*, 851-862.

25. Mohraz, A.; Solomon, M. J. *Langmuir* **2005**, *21*, 5298-5306.

26. Clarke, T. D.; Tien, J.; Buffy, D. C.; Paul, K. E.; Whitesides, G. M. *J. Am. Chem. Soc.* **2001**, *123*, 7677-7682.

27. Lee, J. A.; Meng, L.; Norris, D. J.; Scriven, L. E.; Tsapatsis, M. *Langmuir* **2006**, *22*, 5217-5219.

28. Wong, S.; Kitaev, V.; Ozin, G. A. *J. Am. Chem. Soc.* **2003**, *125*, 15589-15598.

29. Okubo, M.; Minami, H. *Macromol. Symp.* **2000**, *150*, 201-210.

30. Okubo, M.; Minami, H. *Colloid Polym. Sci.* **1997**, *275*, 992-997.

31. Okubo, M.; Minami, H.; Yamamoto, Y. *Colloid Surfaces A: Physicochem. Eng. Aspects* **1999**, *153*, 405-411.

32. Okubo, M.; Minami, H.; Morikawa, K. *Colloid Polym. Sci.* **2001**, *279*, 931-935.

33. Ye, Y.; LeBlanc, F. ; Hache, A.; Truong, V. *Appl. Phys. Lett*. **2001**, *78*, 52-54.

34. Adachi, E.; Dimitrov, A. S.; Nagayama, K. *Langmuir*, **1995**, *11*, 1057-1060.

35. Akbarian, M.; Nunes, J.; Stone, H. A. *J. Am. Chem. Soc.* **2004**, *126*, 5978-5979.

36. Pan, F.; Zhang, J.; Cai, C.; Wang, T. *Langmuir*, **2006**, *22*, 7101-7104.

37. Prevo, B. G.; Velev, O. D. *Langmuir*, **2004**, *20*, 2099-2107.

38. Lumsdon, S. O.; Kaler, E. W.; Velev, O. D. *Langmuir*, **2004**, *20*, 2108-2116.

39. Liu, J.; Weitz, D. A.; Ackerson, B. J. *Phys. Rev. E* **1993**, *48*, 1106-1114.

40. Palmer, C. Diffraction Grating Handbook 5th Ed.; Thermo RGL: New York, **2002**, Ch. 2.

41. Velikov, K. P.; Christova, C. G.; Dullens, R. P. A.; van Blaaderen, A. *Science* **2002**, *296*, 106-109.

42. Denkov, N. D.; Velev, O. D.; Kralchevsky, P. A.; Ivanov, I. B.; Yoshimura, H.; Nagayama, K. *Langmuir* **1992**, *8*, 3183-3190.

43. Dimitrov, A. S.; Nagayama, K. *Langmuir* **1996**, *12*, 1303-1311.

44. Dushkin, C. D.; Lazarov, G. S.; Kotsev, S. N.; Yoshimura, H.; Nagayama, K. *Colloid Polym. Sci.* **1999**, *277*, 914-930.

45. Cong, H.; Cao, W. *Langmuir* **2003**, *19*, 8177-8181.

46. Kralchevsky, P. A.; Nagayama, K. *Langmuir* **1994**, *10*, 23-36.

CHAPTER 3

CONVECTIVELY ASSEMBLED ASYMMETRIC DIMER-BASED COLLOIDAL CRYSTALS*

Abstract

Monolayer films from polystyrene asymmetric dimer colloidal particles were formed on a silicon substrate using a heat assisted vertical deposition technique. In dilute particle suspensions of systematically varied concentration, the system maximizes the packing efficiency within a thin meniscus region. Structures with positional order and orientational order in- and out of the substrate plane were observed in surface and cross-sectional SEM images. The confining effect of the meniscus height drove the formation of the resulting oblique and hexagonal lattices with controlled orientation. The crystals exhibited features similar to planes of the boron nitride and zinc sulfide atomic structures. The diffraction properties of both colloidal crystal structures were demonstrated via selected area diffraction for laser light in the visible region.

Introduction

Non-spherical based colloidal crystals have the potential to advance several mesoparticle applications. For example, photonic crystals from non-spherical colloids have been shown in calculations to lift symmetry induced degeneracies,[1-4] which promotes photonic bandgaps at lower refractive index contrasts. Single wavelength lasing with controlled polarization[5] was also attributed to the shape anisotropy of non-

* *Published: I. D. Hosein, C. M. Liddell, "Convectively Assembled Asymmetric Dimer-Based Colloidal Crystals",* Langmuir*, 2007, 23 (21), pp 10479–10485. – Reproduced by permission of The American Chemical Society.*
http://pubs.acs.org/doi/abs/10.1021/la7007254

spherical bases at the lattice points. Additionally, non-spherical based colloidal arrays in both 2D and 3D could lead to advances in the nanofabrication[6] of complex devices and in the production of microlens arrays.[7,8] In general, colloidal crystals can model the properties of atomic or molecular crystals,[9] as well as other systems in condensed matter[10] and statistical physics.[11] Ordered arrays with non-spherical bases would make crystal structures accessible for study, which have higher complexity than can be achieved with spherical particles. However, the crystallization process of non-spherical colloidal is not well understood, and experimental achievements of ordered structures have been limited in the literature.

In concentrated colloidal suspensions, crystallization occurs to maximize the free volume entropy and minimize the free energy of the system.[12] In the case of nonspherical particles, the orientational freedom of the particles in suspension can increase the entropy and may favor disordered structures. However, simulations have suggested that ordered structures could be formed from colloidal discs, rods and ellipsoids.[13-16] The drive to maximize particle free volume dominates and leads to theoretical structures with both positional and orientational order. The free volume entropy more than offsets the loss of orientational entropy for these ordered structures.[17, 18] Nonetheless, the majority of experimental studies on nonspherical particles report liquid crystalline structures[5,19 -21] with only a few suggesting the possibility of long-range crystallinity.[17, 20] This may be due to kinetic effects in the self-assembly process that inhibit the system from reaching thermodynamically favored ordered states. While spherical colloids crystallize under a wide variety of non-equilibrium conditions (i.e. sedimentation, convective deposition, filtration), anisotropic particles require tight control of particle alignment as well as orientation during the self-assembly process.

To achieve this aim, Xia and co-workers suggested that positionally ordered

non-spherical colloids could be orientationally ordered in suspension using an applied field.[22] Whitesides and co-workers[23] assembled colloidal plates (~10μm, beyond the colloidal regime in size) into multilayer stacks of ordered columnar structures by hydrophobic-hydrophilic interactions. Kulak et al.[24] attempted to assemble rod shape zeolite nanocrystals in water droplets dispersed in toluene, by the addition of sodium dodecylsulfate (SDS). Two layers of nanocrystals on the surface of the droplet oriented and ordered to minimize the electrostatic repulsion induced by the negatively charged anionic surfactant, however the interior of the colloidsome structure remained disordered. Liu et al.[25] also produced locally ordered monolayer films from lead zirconate titante cubes (2-3μm in size) using a Langmuir-Blodgett method to assemble monolayers from particles dispersed in a non-polar solvent over a water surface. Another method recently demonstrated to restrict the particle orientations during self-assembly is confinement in a region with a dimension comparable to the particle size. For example, Lee et al. applied a convective assembly scheme where hexagonal nanoplates were confined in a thin wetting layer on a substrate. The plates remained oriented with hexagonal faces parallel to the substrate, but only local positional order was achieved due in part to the polydispersity of the nanoplates.[26]

In convective assembly, the solvent flux from a bulk particle suspension into a thin wetting film provides a constant flow of particles to the crystallization region at the meniscus. This can produce a continuous film as the meniscus sweeps across the substrate.[27] The formation of 2D arrays has been studied extensively for spherical particles on solid and liquid surfaces.[28-31] Arrays can also be formed in the meniscus region on substrates inclined[32] or perpendicular to the suspension surface.[33] Crystallization begins when the thickness of the wetting layer containing the particles becomes approximately equal to the particle diameter. Along with solvent flow, attractive interparticle capillary forces promote assembly into ordered arrays.[34]

Convective techniques have also been extended to include the assembly of multilayer films, with the number of layers controlled by the particle volume fraction in the suspension.[35] For film deposition, substrates could either be withdrawn from the suspension mechanically[33] or held fixed with the meniscus allowed to recede.[35] The substrate withdrawal rate, relative humidity and temperature were used to control the rate of crystallization as these effect the rate at which the meniscus recedes. Through heating the suspension to abate particle settling, the convective assembly process was also applied to particles with large sizes (>800nm) or high density.[36-39]

Here, we report the self-assembly of asymmetric dimer-shaped particles using a heat assisted convective assembly technique. Thin colloidal films were deposited on clean hydrophilic substrates, from suspensions with concentrations between 0.025-0.100 wt%. Asymmetric dimers can be synthesized from polystyrene spheres by seeded emulsion polymerization, i.e., a daughter lobe forms due to phase separation from a crosslinked seed.[40] The dimers in the present study were 3μm in length, with 1.5μm and 2μm (diameter) interpenetrating lobes. The particle orientations were defined in terms of the direction of the particle longitudinal axis, as either in- or out of plane with respect to the substrate surface.

One motivation for assembling the particle shape is the predictions of complete photonic bandgaps in crystals from dimers.[1, 3] Beyond this photonics application, fundamental studies are also of interest to clarify the effects producing 2D or 3D non-spherical colloid-based materials with unique degrees of structural variation.

Experimental

Particle suspensions were prepared with 18.2 MΩ ultrapure water (Barnstead, NanoPure Diamond). Ten to twenty microliters of 10 wt% polystyrene dimer suspension (Magsphere Inc., Pasadena, CA) was added to 2 mL of water. The

suspension was placed in a vial and sonicated for 1 minute to ensure complete dispersion of the particles. The vial was cleaned with water and ethanol, and dried under a flow of nitrogen gas prior to use. Silicon and glass substrates were soaked in freshly prepared piranha solution (18M H_2SO_4 and 30 wt% H_2O_2 solution, in a 2:1 v/v mixture) for 30 minutes, rinsed several times with water, and dried under nitrogen. Glass substrates were exposed to oxygen plasma for 10 minutes to increase their hydrophilicity before use. The substrates were dipped vertically into the polystyrene suspensions and were held in place by two binder clips. The setups were left overnight in an oven at 65 °C, for assembly to occur and for the liquid to completely evaporate. Scotch tape was used to anchor the binder clips to ensure the substrate position was stable when the vials were transferred and handled. The films were sputtered with gold before characterization with SEM. The SEM images were obtained with an LEO 1550 field emission scanning electron microscope.

Selected area laser diffraction was performed using a Renishaw (Gloucestershire, UK) inVia Raman system with a Leica DMLB optical microscope and a 785nm diode laser (Renishaw, Model HPNIR785, 300mW). Diffraction images were taken with a digital camera (Angstrom Sun Tech., Acton MA, Model CFM-USB-3) mounted under the sample.

Results and Discussion

For relatively low particle concentrations (ϕ ~ 0.05wt%) domains of 2D order were obtained within the monolayer colloidal films. Figure 3.1a shows SEM images of the arrays of particles aligned in plane and parallel to one another, forming an oblique lattice within each grain. The polycrystalline film of asymmetric dimers extends for tens of microns over the surface of the substrate. Large-scale non-equiaxed domains, with dimensions approximately 100μm by 20μm were produced,

with the longer grain dimension parallel to the particle longitudinal axis. The fast Fourier transform (FFT) of a single domain (Figure 3.1c) shows a clear spot pattern, and confirms the oblique lattice. The well defined spots up to 5th order, also indicate the quality of packing and order in the single crystal domain. Figure 3.1d shows the FFT corresponding to the entire field of Figure 3.1a. The elliptical diffraction rings display non-uniform intensity characteristic of preferred orientation in the polycrystalline film. Particles were preferentially aligned parallel to the direction of drying, and rows consisting of the aligned particles formed along the drying front as it receded. Particle alignment along the direction of drying may arise from the hydrodynamic field, as solvent flow induces body torques on the particles.[41] Increasing the particle concentration to ~0.075wt% led to ordered arrays with particle orientation predominantly out-of-plane, as shown in Figure 3.1b. The particles were arranged on a hexagonal lattice. Domain sizes up to several tens of microns were obtained. The 6-fold symmetry and high degree of crystalline order is reflected in the FFT spot pattern shown in Figure 3.1e, where peaks up to 3rd order are clearly present.

Figure 3.2a and Figure 3.2b show high magnification SEM images of ordered arrays of particles aligned in-plane. The oblique lattice structure has lattice vectors a_1 and a_2 ($|a_1| \approx 1.84\mu m$, $|a_2| \approx 2.62\mu m$, $\theta \approx 70°$). Correlated nearest neighbor orientation (i.e. small lobe of one particle adjacent to the large lobe of its nearest neighbor) occurred randomly in the crystal. The distribution in particle orientation was 7.5°, as measured by taking the standard deviation from a mean direction for 100 particles in an SEM image. The structure is significantly more ordered than the amorphous film (Figure 3.5b). The particle orientational freedom was considerably reduced, not only to the in-plane orientation, but also to particle orientations within a small range of angles. The colloidal crystal is analogous to an atomic sheet of the (001) plane in the boron nitride (BN) crystal structure (Figure 3.2c), but with closer packing.[42] Another difference is

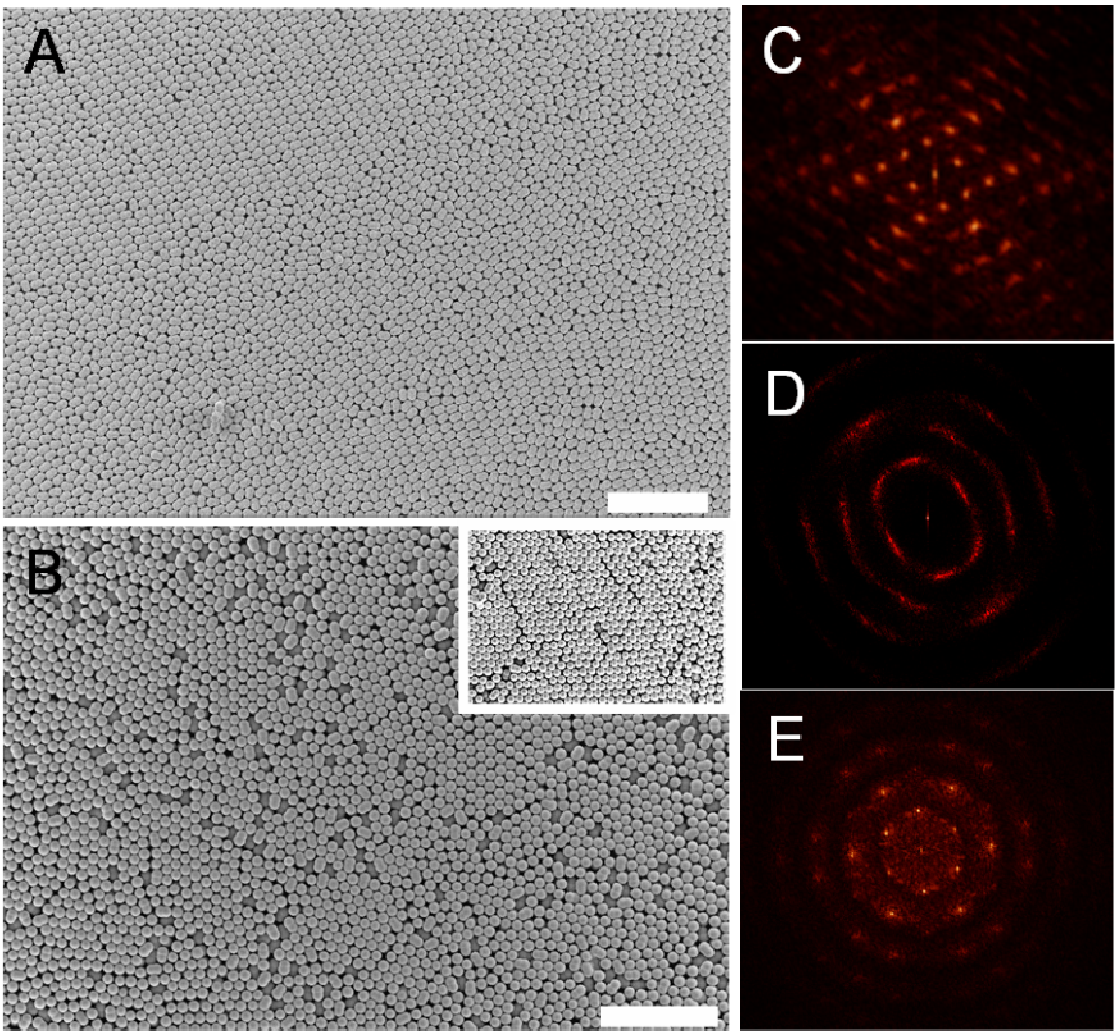

Figure 3.1. Large area monolayers of asymmetric dimers. A) Polycrystalline film of in-plane oriented particles ordered on an oblique lattice. B) Film of out-of-plane oriented particles showing hexagonal packing. Inset shows a close up of a single crystal domain. C) FFT of a single crystal domain from the film shown in A). D) FFT of entire film shown in A). E) FFT of inset of B). Scale bars represent 20μm.

that the position of lobes on the "boron" and "nitrogen" sites is random in the colloidal crystal.

Figure 3.3a and Figure 3.3b show high magnification SEM images of ordered arrays of particles aligned out-of-plane. A hexagonal structure ($|a| \approx 1.90\mu m$, $\theta \approx 60°$) was observed. These crystals also formed with the lines of particles parallel to the drying front. Compared to atomic AB-type crystals, the 2D structure is similar to the

(001) and $(\bar{1}\bar{1}1)$ planes of the wurtzite and sphalerite zinc blende structures, respectively. Particle orientation with respect to these crystal planes is <001> for hexagonal and <111> for cubic ZnS. The correlation between large and small lobes of nearest neighbors in the "Zn" and "S" sites was random.

A further increase in concentration (ϕ ~ 0.1wt%) generally led to two layers of disordered particles oriented in-plane. However, an ordered region having the out-of-plane hexagonal structure was observed in the transition region between the first and second layers (Figure 3.5g). The transition region showed a continuous change in orientation of the particles from parallel-to perpendicular to the substrate. Thereafter, the hexagonal structure grew for a few microns, before transitioning to the two layer in-plane disordered structure. Transitions returning from two layers back down to one layer exhibited a much more abrupt change from the out-of-plane to the in-plane orientation. For particle concentrations ϕ > 0.1wt% thick amorphous films were produced.

The optical diffraction study of the films was conducted using an optical microscope with monochromatic laser light (λ = 785nm) coupled through the objective lens. At low magnification a small collimated beam with a spot size of approximately 70μm in diameter was produced, allowing the examination of local regions in the film. Figure 3.4a and Figure 3.4b show the diffraction patterns from films deposited on glass substrates (0.075wt%). A ring pattern (Figure 3.4c and Figure 3.4d) characteristic of polycrystalline structure was obtained from both monolayers of in-plane and out of plane oriented particles. The preferred orientation of the large grains in the polycrystalline structure for the oblique lattice led to an elliptical rather than a circular diffraction ring (observed for the hexagonal lattice). The patterns abruptly changed to sharp spot patterns when the laser beam scanned over large-scale single crystal regions. For example, Figure 4e shows the single

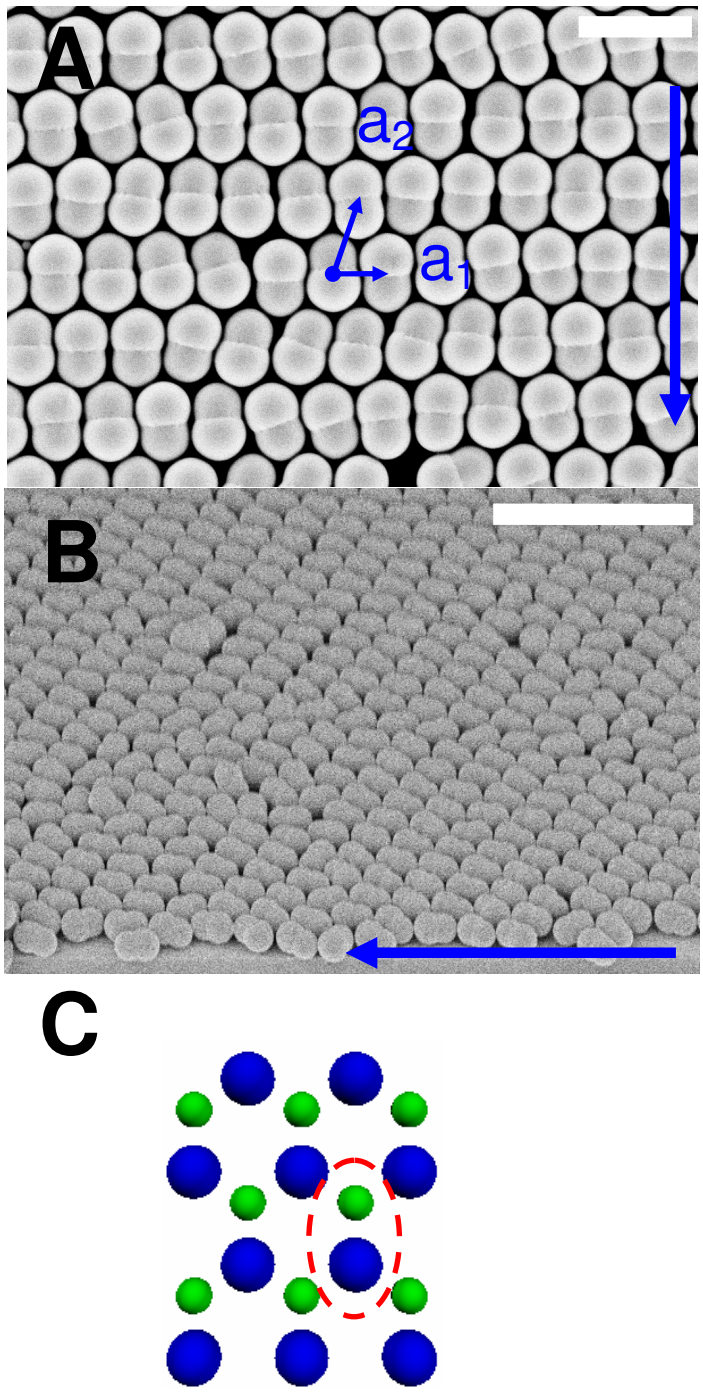

Figure 3.2. Self-assembled asymmetric dimers, oriented in-plane. (A) Top view and (B) cross-sectional images of 2D arrays. Scale bars represent 2μm and 10μm, respectively. Drying directions indicated by large arrows. (C) Atomic sheet on the crystal plane of the BN crystal structure, boron (green) and nitrogen (blue).

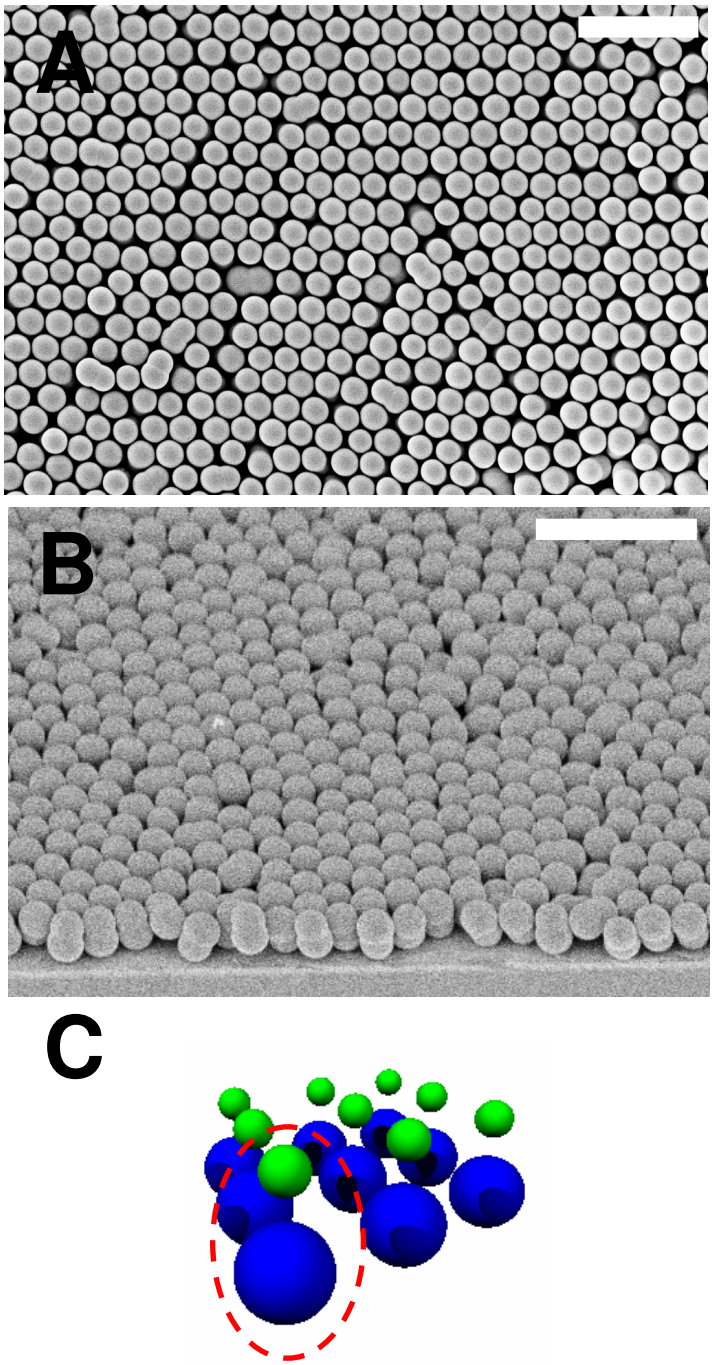

Figure 3.3. Self-assembled asymmetric dimers, perpendicular to substrate. (A) Top view and (B) cross-section images of crystals from particles aligned out-of-plane. Scale bars are 10μm and 8μm, respectively. (C) (001) atomic crystal plane of the wurtzite crystal structure, Zn (green) and S (blue).

crystal pattern produced from an oblique lattice. The pattern reflected the 2-fold symmetry of the 2D crystal structure. Similarly, Figure 3.4f shows the diffraction pattern with 6-fold symmetry indicative of the hexagonal lattice. The sharp 6-spot patterns confirmed domain sizes on the order of tens of microns, since the domain size is comparable to the beam spot size. Higher order diffracted beams were also visually observed (Figure 3.4a and Figure 3.4b).

The diffraction angles observed in experiment were compared with the theoretical calculations predicted by modeling the structures as 2D gratings. The diffraction pattern corresponds to the reciprocal lattice of the crystal structure, and each diffraction spot can be assigned miller indices (*h,k*). The reciprocal lattice vector to each point in the reciprocal lattice is given by:

$$\vec{G}_{hk} = h\vec{b}_1 + k\vec{b}_2 \qquad (1)$$

where $\vec{b}_1$ and $\vec{b}_2$ are the reciprocal lattice basis vectors. These were determined from the real space lattice vectors observed in the SEM images. The line spacing d_{hk} corresponding to each diffraction spot was determined from the magnitude of the reciprocal lattice vector:

$$d_{hk} = \frac{1}{\left|\vec{G}_{hk}\right|} \qquad (2)$$

where the line spacing is the perpendicular distance between rows of particles in the crystal. The theoretical diffraction angles were calculated from the grating equation,[34, 44]

$$\frac{\lambda}{d_{hk}} = n_1 \sin\theta - n_2 \sin\theta_i \qquad (3)$$

where λ is the wavelength, θ is the diffraction angle, θ_i is the angle of incidence, and n_1 and n_2 are the refractive indices of the media adjacent to the film (air above, n_1=1 and glass substrate below). Equation (3) incorporates Snell's law so that θ and θ_i represent the light incident on and exiting the film, respectively. Both angles are

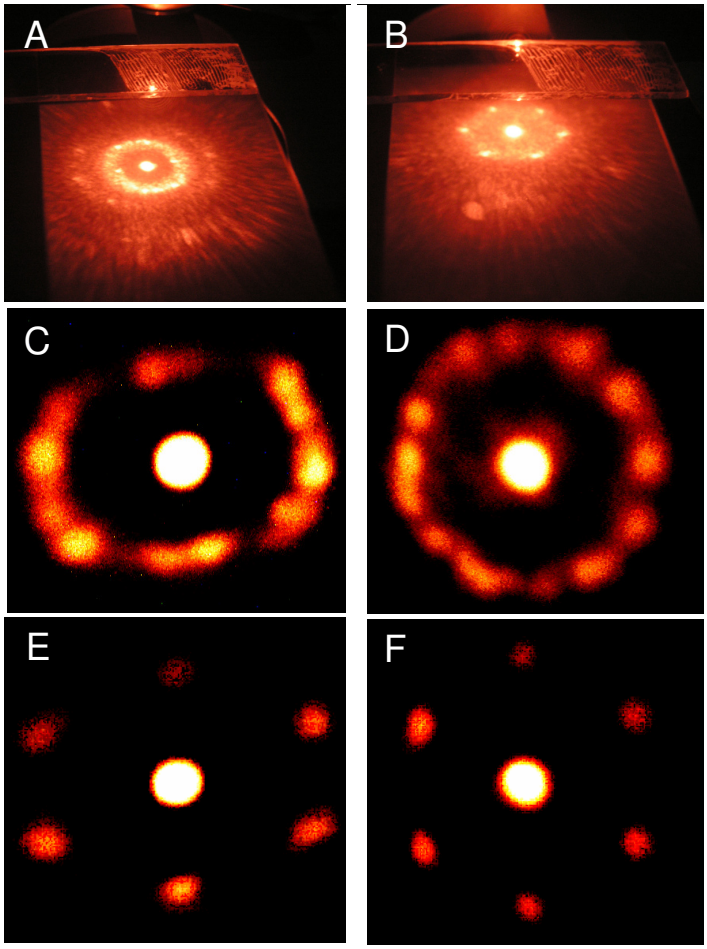

Figure 3.4. Optical diffraction patterns. A) Diffraction pattern from crystalline regions of in-plane oriented particles. B) Diffraction pattern from crystalline region of out-of-plane oriented particles. C) Polycrystalline monolayer of in-plane oriented particles. D) Polycrystalline monolayer of out–of- plane oriented particles. E) Single crystal oblique lattice of in-plane oriented particles. F) Single crystal hexagonal lattice of out-of-plane oriented particles.

measured from the surface normal. For light at normal incidence (i.e., $\theta_i = 0°$) the equation simplifies to the von Laue relation,

$$\frac{\lambda}{d_{hk}} = \sin\theta \qquad (4)$$

Figure 3.1 summarizes the experimental and calculated diffraction data.

Lattice constants were determined from the line spacings calculated with the experimental diffraction angles using equation (4). The diffraction angles corresponding to first order diffraction spots (i.e. those closest to the m=0 transmission spot, shown in Figure 4e and f) were used. The lattice constants were calculated as 1.86μm and 2.60μm for the oblique lattice, and 1.92μm for the hexagonal lattice, in agreement with the lattice constants observed in the SEM images. The Miller indices for each diffraction spot are also given in Table 3.1. Higher order diffraction from *(h, k)* lines is indicated by miller indices *(nh, nk)* where n is the order of the diffraction.

The oblique and hexagonal crystal structures were formed at the drying front as a result of the controlled particle concentration in the bulk solution, confinement at the meniscus region and the drive to maximize the geometric packing efficiency.[45] Figure 3.5 summarizes the concentration and confinement effects on the colloidal structures formed. The structure dependence on particle concentration arises from the correlation between the particle flux (controlled by particle concentration) and the position of the crystal growth front along the sloping meniscus (Figure 3.5a).[46] At low particle concentrations (ϕ < 0.05wt%) the transported particles begin to pack in the meniscus region having height comparable to the particle diameter. The dimers orient in-plane due to the surface tension effects of the local meniscus around the protruding particles[34] (Figure 3.5b). When the concentration becomes sufficient (ϕ ~ 0.05wt%) attractive capillary forces facilitate crystallization of the in-plane oriented particles onto an oblique lattice (Figure 3.5c). At higher particle concentration (0.05wt% < ϕ < 0.075wt%), the rate that particles enter the drying front exceeds their addition to the in-plane monolayer film assembly, (e.g. the meniscus recedes slower than monolayer crystallization occurs). A steady state is again reached where the meniscus height is larger and thicker films can be deposited.[46] The meniscus height is intermediate between that for films of one and two particle layers oriented in-plane. Out-of-plane

Table 3.1. Summary of optical diffraction data.

Crystal Type	Calcd. Diffraction Angle (°)	Exptl. Diffraction Angle (°)	Miller Indices	SEM Lattice Constant (μm)	Diffraction Lattice Constant (μm)
Oblique	18.6	18.8	(0,1), (0,-1)	1.84	1.86
	27.0	26.7	(1,0), (-1,0), (1,1), (-1,1)	2.62	2.60
	39.6	37.9	(0,2), (0,-2)	-	-
	40.1	39.2	(1,2), (1,-1), (-1,1), (-1,-2)	-	-
	58.6	58.2	(2,1), (-2,-1)	-	-
Hexagonal	28.5	28.2	(0,1), (0,-1), (1,0), (-1,0), (1,1), (-1,-1)	1.90	1.92
	55.7	53.6	(1,-1), (-1,1), (1,2), (2,1), (-1,-2), (-2,-1)	-	-
	72.6	70.7	(0,2), (2,0), (0,-2), (-2,0), (2,2), (-2,-2)	-	-

particles on a hexagonal lattice (Figure 3.5d) pack this region most efficiently. As particle concentration increases to $\phi > 0.075$wt% the growth front shifts to a meniscus with height comparable to the two layer in-plane oriented structure. The two layer film grows as a more open structure (Figure 3.5e) and finally as a dense disordered film (Figure 3.5f). A local region of the colloidal film where structural transitions are apparent is provided in Figure 4g. Changes in crystal structure to achieve more efficient packing of the meniscus have been observed in spherical colloidal crystal systems, where square 2D packing occurred in the transition region between one and two layers.[46-51] In contrast to the hexagonal packing of the asymmetric dimers in the transition region in the present study, the square packing observed for spherical colloids did not extend over large areas.[46, 50] This is probably due to the less favorable

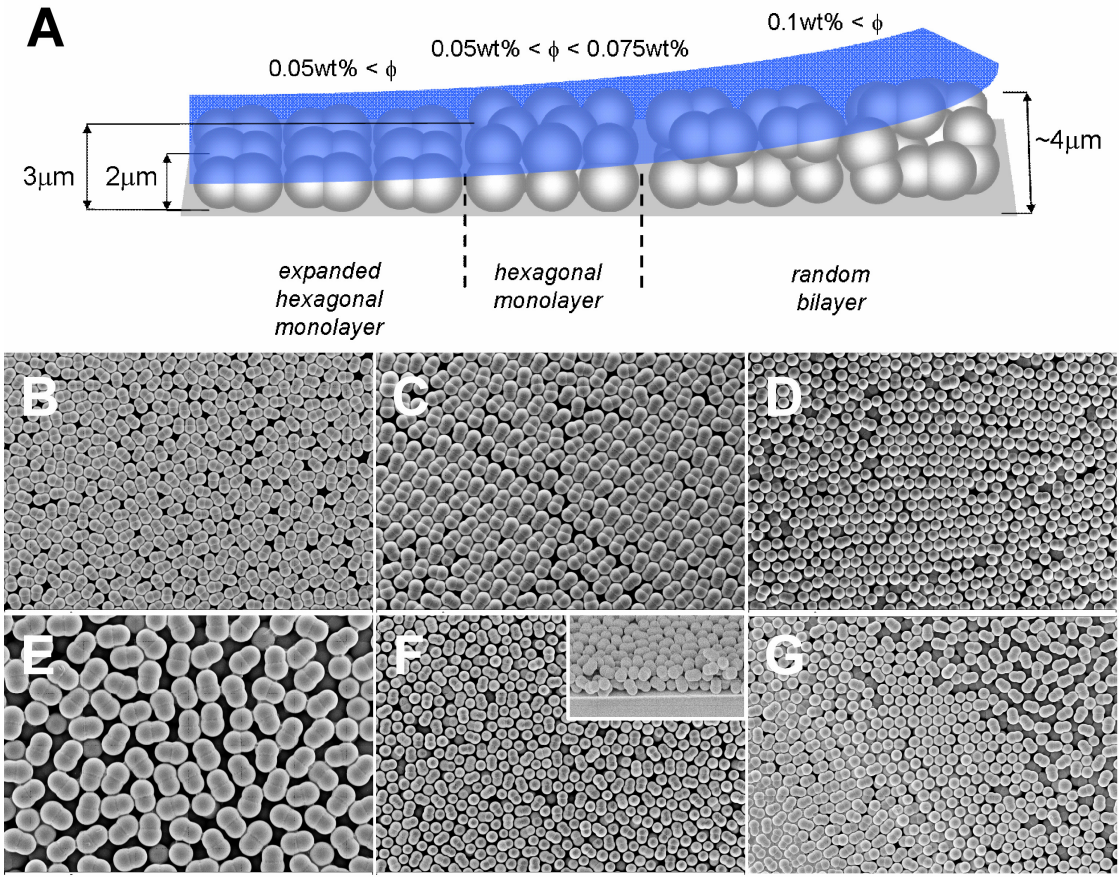

Figure 3.5. Structures formed from asymmetric dimers as a function of concentration. A) Schematic of the packing arrangements depending on the location along the meniscus slope (blue). B) Amorphous monolayer formed at $\varphi < 0.05$wt%. C) Ordered monolayer of in-plane particles at $\varphi \sim 0.05$wt%. D) Ordered monolayer of out-of-plane aligned particles at $\varphi \sim 0.075$wt%. E) Two layer thick disordered structure, with second layer exhibiting a loosely packed structure, at 0.1wt%. F) Two layer dense disordered structure, at 0.1wt%. Inset: Cross-sectional image. G) Transition region between one and two layers.

open packing of the square lattice.

From the mass balance of solvent evaporation, solvent flow and deposition at the drying front, a simple expression[33] has been derived for the film height h in terms of the system parameters:

$$h = \frac{\beta l}{(1-\varepsilon)} \frac{\varphi}{(1-\varphi)} \quad (5)$$

β is the ratio of the mean particle speed to the mean speed for the solvent to enter the drying front. For submicron sized particles with low density β is 1. Additionally, l is

the meniscus height over which evaporation occurs, (1-ε) is the packing density of a monolayer (i.e., ε is the porosity) and φ is the volume fraction of particles in the suspension. Figure 3.6 shows a plot of the film thickness versus suspension concentration. A linear relationship between film height and particle concentration is apparent, indicating that, regardless of the structure of the film, the film thickness could be predicted systematically from particle concentration (in accordance with equation 5).

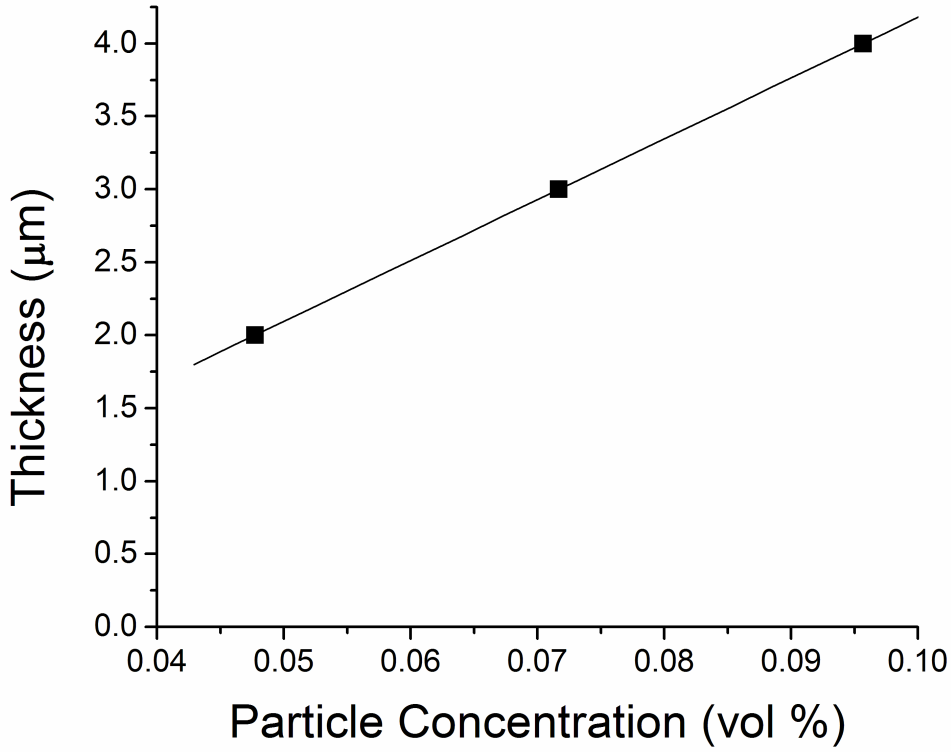

Figure 3.6. Thickness versus particle concentration.

Conclusion

Colloidal structures containing 2D ordered packing were formed in thin films of convectively assembled asymmetric dimers. Particles were selectively oriented in-plane or out-of-plane with respect to the substrate, analogous to crystal planes of the

BN and ZnS atomic crystal structures. Structural changes were tuned via the concentration of the particle suspension. Optical characterization showed strong diffraction properties for crystals with hexagonal and oblique lattices. The structural diversity observed may be driven by the most efficient packing of the meniscus region. This work suggests that convective assembly is an appropriate technique to achieve a range of structures with complex architectures and symmetries from non-spherical colloid shapes.

REFERENCES

1. Xia, Y.; Gates, B.; Li, Z. *Adv. Mater.* **2001** *13*, 409-413.
2. Leung, K. M.: Liu, Y. F. *Phys. Rev. Lett.* **1990**, *65*, 2646-2649.
3. Li, Z.; Wang, J.; Gu, B. *Phys. Rev. B*. **1998**, *58*, 3721-3729.
4. Ngo, T. T.; Ghebrebrhan, M.; Joannopoulos, J. D.; Liddell, C. M. *Appl. Phys. Lett.* **2006**, *88*, 241920-3.
5. Noda, S.; Yokoyama, M.; Imada, M.; Chutinan, A.; Mochizuki, M. *Science* **2001**, *293*, 1123.
6. Brown, A. B. D. ; Rennie, A. R. ; Ferroro, C. ; Narayanan, T. *Eur. Phys. J. B* **1998**, *11*, 481.
7. Lu, Y.; Yin, Y.; Xia, Y. *Adv. Mater.* **2001**, *13*, 34-37.
8. Hayashi, S.; Kumamoto, Y.; Suzuki, T.; Hirai, T. *J. Colloid Interface Sci.* **1991**, *144*, 538.
9. Arora, A. K.; Tata, B. V. R. *Ordering and phase transitions in charged colloids*; Wiley: New York, 1996.
10. Sood, A.K. *Solid State Phys.* **1991**, *45*, 1.
11. Babic, D.; Schmitt, C.; Bechinger, C. *Chaos* **2005**, *15*, 026114-6.
12. Berry, R. S.; Rice, S. A.; Ross, J. *Physical Chemistry 2nd Edition*; Oxford University Press: New York, 2000.
13. Trizac, E.; Bocquet, L.; Agra, R.; Weis, J.-J.; Aubouy, M. *J. Phys. C*. **2002**, *14*, 9339-9352.
14. Savenko, S. V.; Dijkstra, M. *Phys. Rev. E*. **2004**, *70*, 051401-7.
15. Marko, J. F. *Phys. Rev. A*. **1989**, *39*, 2050-2062.
16. Stroobants, A.; Lekkerkerker, H. N. W.; Frenkel, D. *Phys. Rev. A*. **1987**, *36*, 2929-2945.
17. Frenkel, D. *Theor. Chem. Acc.* **2000**, *103*, 212-213.

18. van Rojj, R. *Eur. J. Phys.* **2005**, *26*, S57–S67.

19. van der Kooij, F. A.; Lekkerkerker, H. N. W. *J. Phys. Chem. B*. **1998**, *102*, 7829-7832.

20. Brown, A. B. D. ; Rennie, A. R. *Phys. Rev. E.* **2000**, *62*, 851-862.

21. Mohraz, A.; Solomon, M. J. *Langmuir*, **2005**, *21*, 5298-5306.

22. Lu, Y.; Yin, Y.; Xia, Y. *Adv. Mater.* **2001**, *13*, 415-420.

23. Clarke, T. D.; Tien, J.; Buffy, D. C.; Paul, K. E.; Whitesides, G. M. *J. Am. Chem. Soc.* **2001**, *123*, 7677 – 7682.

24. Kulak, A.; Lee, Y.J.; Park, S.; Kim, H. S.; Lee, G. S.; Yoon, K. B. *Adv. Mater.* **2002**, *14*, 526-529.

25. Liu, X.; McCandlish, E. F.; McCandlish, L. E.; Mikulka-Bolen, K.; Ramesh, R.; Cosandey, F.; Rossetti Jr., G. A.; Riman, R. E. *Langmuir,* **2005**, *21,* 3207-3212.

26. Lee, J. A.; Meng, L.; Norris, D. J.; Scriven, L. E.; Tsapatsis, M. *Langmuir* **2006** *22*, 5217-5219.

27. Yamaki, M.; Matsubara, K.; Nagayama, K. *Langmuir* **1993**, *9*, 3154-3158.

28. Duskin, C. D.; Yoshimura, H.; Nagayama, K. *Chem. Phys. Lett.* **1993**, *204*, 455-460.

29. Denkov, N. D.; Velev, O. D.; Kralchevsky, P. A.; Ivanov, I. B.; Yoshimura, H.; Nagayama, K. *Langmuir* **1992**, *8*, 3183.

30. Dimitrov, A. S.; Dushkin, C. D.; Yoshimura, H.; Nagayama, K. *Langmuir* **1994**, *10*, 432-440.

31. Dimitrov, A. S.; Yamaki, M.; Nagayama, K. *Langmuir* **1995**, *11*, 2682-2688.

32. Dimitrov, A. S.; Nagayama, K. *Chem. Phys. Lett.* **1995**, *243*, 462-468.

33. Dimitrov, A. S; Nagayama, K. *Langmuir* **1996**, *12*, 1303-1311.

34. Nagayama, K. *Colloids Surf. A: Physiochem. Eng. Aspects* **1996**, *109*, 363-374.

35. Jiang, P.; Bertone, J. F.; Hwang, K. S.; Colvin V. L. *Chem. Mater.* **1999**, *11*, 2132-2140.

36. Vlasov, Y. A.; Bo, X. Z.; Sturm, J. C.; Norris, D. J. *Nature* **2001**, *414*, 289-293.

37. Ye, Y. H.; LeBlanc, F.; Hache, A.; Truong, V. *Appl. Phys. Lett.* **2001**, *78*, 52-54.

38. Wong, S.; Kitaev, V.; Ozin, G. A. *J. Am. Chem. Soc.* **2003**, *125*, 15589-15598.

39. Hosein, I. D.; Liddell, C. M.; *Langmuir* **2007**, *23*, 2892 -2897.

40. Okubo, M.; Katsuta, Y.; Matsumoto, T. *J. Polym. Sci.: Polym. Lett. Ed.* **1982**, *20*, 45.

41. Huang, Y.; Duan, X.; Wei, Q.; Lieber, C. M. *Science*, **2001**, *291*, 630-633.

42. Wycoff, R. W. G. *Crystal Structures* Vol. 1; Wiley: New York, 1963; p. 63.

43. Palmer, C. Diffraction Grating Handbook 5th Ed.; Thermo RGL: New York, 2002, Ch. 2.

44. Born, M.; Wolf, E. Principles of Optics 4th Ed.; Pergamon Press: London, 1970; Ch. 8.

45. Velikov, K. P.; Christova, C. G.; Dullens, R. P. A.; van Blaaderen, A. *Science* **2002**, *296*, 106-109.

46. Dushkin, C. D.; Lazarov, G. S.; Kotsev, S. N.; Yoshimura, H.; Nagayama, K. *Colloid Polym. Sci.* **1999**, *277*, 914-930.

47. Pieranski, P.; Strzelecki, L.; Pansu, B. *Phys. Rev. Lett.* **1983**, *50*, 900-903.

48. Van Winkle, D. H.; Murray, C. A. *Phys. Rev. A.* **1986**, *34*, 562-573.

49. Murray, C. A.; Van Winkle, D. H. *Phys. Rev. Lett.* **1987**, *58*, 1200-1203.

50. Prevo, B. G.; and Velev, O. D. *Langmuir* **2004**, *20*, 2099-2107.

51. Meng, L.; Wei, H., Nagel, A.; Wiley, B. J.; Scriven, L. E.; Norris, D. J. *Nano Lett.* 2006, 6, 2249-2253.

CHAPTER 4

ROTATOR AND CRYSTALLINE FILMS VIA SELF-ASSEMBLY OF SHORT-BOND LENGTH COLLOIDAL DIMERS*

Abstract

Nonspherical particles of pear-like and spherocylinder shape were organized into diverse two-dimensional (2D) structures, including the orientationally disordered rotator. Dry films with hexagonal, oblique, and centered rectangular symmetry were obtained by using convective assembly to condense and confine the system in a thin meniscus region. Monte Carlo simulations confirmed the transition from fluid to rotator simply as a function of system density and short-bond length particle morphology.

Self-assembly processes are regarded as prime platforms for the cost efficient fabrication of materials structured on micro- to nanoscales— for example, tissue engineering scaffolds which allow high resolution optical monitoring of cell proliferation in situ,[1] SERS (surface enhanced Raman scattering) substrates for high sensitivity chemical and biosensors,[2] "hypersonic crystals" with phononic band gaps for on-chip thermal management,[3] and photonic band gap materials for optical microcircuitry and solid state lighting, to name a few. Often the building blocks for assembly are colloidal particles, because their size (100nm to ~1 micron) enables the patterning of functional materials on the length scales necessary to exhibit desired

* *Published: Ian D. Hosein, Bettina S. John, Stephanie H. Lee, Fernando A. Escobedo and Chekesha M. Liddell, "Rotator and crystalline films via self-assembly of short-bond-length colloidal dimers", J. Mater. Chem., 2009, **19**, 344. – Reproduced by permission of The Royal Society of Chemistry http://www.rsc.org/Publishing/Journals/JM/article.asp?doi=b818613h*

optical or mechanical properties. Recent advances in the synthesis of monodisperse shape- or surface anisotropic[4] ("patchy") colloids provide the opportunity to address one of the most daunting challenges[5] facing the field, producing a diverse range of ordered structures using simple secondary interactions. In particular, computational simulations and mechanical models suggest that upon system compression (densification) nonspherical dimer colloids should undergo disorder-order and order-order phase transitions to unconventional solid structures, including base-centered monoclinic crystals, degenerate aperiodic crystals, rotator or plastic crystals, etc. based on free energy minimization.[6-10] Using ultra-small angle x-ray scattering, Mock et al. additionally identified body-centered tetragonal (BCT) crystals in suspensions of spherocylinder-shaped dimers above a volume fraction of 0.45.[11] Solvent evaporation from a thin meniscus region at room temperature produced the dry BCT-structured bulk colloidal film.

The three-dimensional bulk structures have been suggested as novel auxetic (negative Poisson ratio) materials for piezoelectric actuators in nano-electromechanical devices (NEMS)[12] or for enhanced de-fouling filters, since the pores would open both along and transverse to the direction of an applied tensile load.[13] Such unique functionality is also expected in two-dimensional (2D) monolayer films of anisotropic particles, if the solvent-free molecular crystal-type phases can be permanently captured. For example, remarkable negative refraction and imaging properties characteristic of photonic crystal superlensing were found for a flat lens with the rotator structure.[14]

Here, we report the 2D rotator and 2D orientationally-ordered phases of pear-shaped and spherocylinder dimer colloids deposited on glass or silicon substrates by evaporation induced self-assembly. Pear-shaped particles have been prepared by raising the temperature of monomer-swollen cross-linked polystyrene seed spheres,

causing the monomer to phase-separate from the seed particle as a bulge rather than a corona, when the seed has undergone a hydrophilic surface treatment.[15,16] The monomer bulge polymerizes, resulting in an anisotropic particle. The pear-shaped particles used in this work had highly-fused constituent lobes [~1.5μm, small lobe diameter (D_s); ~1.75μm, large lobe diameter (D_l); and bond length of ~575nm (L, center-to-center distance of the lobes)] and were obtained from Magsphere (Pasadena, CA). The particle lobe anisotropy is described by a (1-σ*) value of 0.14, where σ* is D_s/D_l , and the degree of lobe fusion is described by the relative bond length value, $L^*=L/D_l$, of 0.33. To grow particulate films, substrates were immersed in suspensions of the nonspherical particles at a 14° incline from horizontal and the solvent was evaporated at 50°C. Varying the particle concentration in the suspensions led to several structural arrangements. Above 0.075wt% an amorphous multilayer formed. Between 0.05wt% and 0.075wt% a monolayer of hexagonally-packed particles was obtained with their major axes aligned normal to the surface of the substrate (Figure 4.1c). Dilution in the range from 0.05wt% down to 0.025wt% produced a monolayer of pear-shaped particles oriented in-plane with respect to the substrate surface and densely packed either into an oblique crystal (Figure 4.1b) or a hindered rotator solid (Figure 4.1a). The lattice parameters measured from scanning electron microscopy (SEM) images of each structure are summarized in.

Differences in the 2D film symmetry and ordering are reflected in the fast Fourier transforms (FFT) of the SEM images (Figure 4.1d-f). In the case of the oblique crystal, the symmetry of the FFT is relatively insensitive to the distinction between the small and large lobes of the particles. The 2-fold rotation axis about the FFT pattern center is present despite the frequent particle misorientation by an angle of π, so that there is actually little persistence in the location of the small (large) lobe tiling of the lattice sites in real space. Instead of the plane group, c1m1, consistent

with pear-shaped dimers all having the same lobe orientation, the plane group describing the structure in Figure 4.1b is p1. A significant overall particle shape effect is apparent however, in regions of the FFT which show spots elongated along directions corresponding to those near the short axis of the particles. The well-defined spots can be distinguished out to large reciprocal distances. The FFT of the rotator, in contrast, shows strong low order spots and diffuse regions further from the origin of the reciprocal lattice. Additionally, the distortion from hexagonal packing, as evidenced by the length difference between the basis vectors of the reciprocal lattice, is subtle for the rotator in comparison to that for the oblique crystal, where the particle directors are parallel with one another. The FFT for particles with major axes roughly perpendicular to the substrate exhibits 6-fold symmetry in the maxima, which is consistent with the p6mm (ideal) plane group of the crystal.

The ideal p6mm symmetry and positional order was more readily achieved with spherocylinder-shaped dimers oriented out-of-plane, since they presumably experience smaller oscillations and tilts on the lattice sites at close packing than do the pear-shaped particles with their significant lobe asymmetry. Our preparation of polystyrene spherocylinders [i.e., cylinders of length L capped on both ends with hemispheres of diameter D, giving $(1-\sigma^*)=0$, $L^*=0.28$] is detailed in the methods section. FFTs (Figure 4.2d-f) for monolayers of spherocylinders indicated longer range positional order in all three film structures, i.e., less diffuse scatter and strong maxima maintained for large reciprocal lattice vectors. The orientationally ordered crystal of in-plane spherocylinders displayed the plane group symmetry, c2mm, as expected from closest-packing considerations. The 2-fold symmetry of the FFT accurately represents the symmetry element found in the crystal.

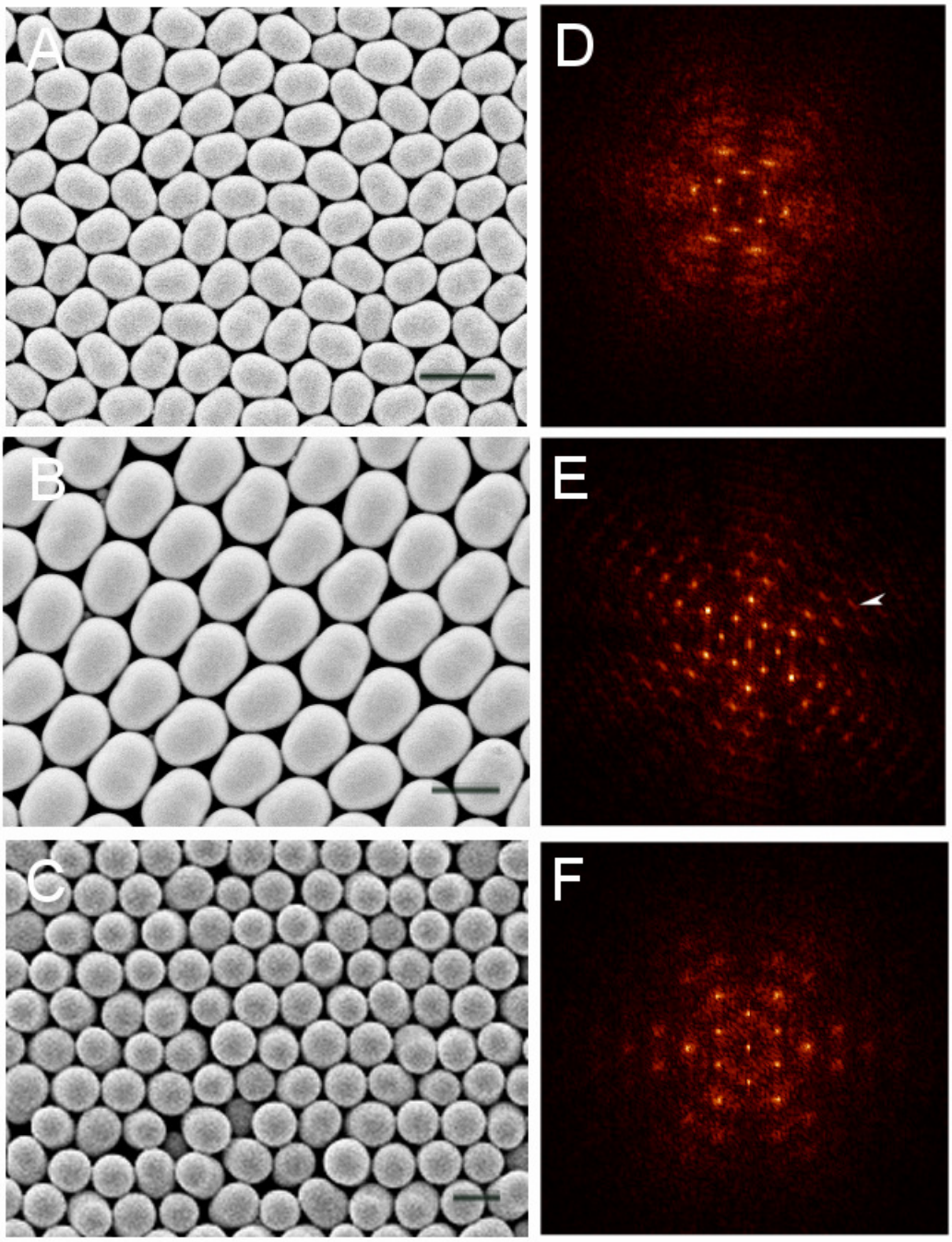

Figure 4.1. Monolayer films of pear-shaped particles. a) rotator, b) oblique, and c) hexagonal structures. Scale bars represent 3 μm in a) and 2 μm in b) and c). d-f) FFT of the adjacent SEM image. Example of spot elongation due to shape effect designated by white arrow. Rotator and oblique grains were deposited from 0.05wt% suspension and hexagonal grains from 0.075wt% suspension.

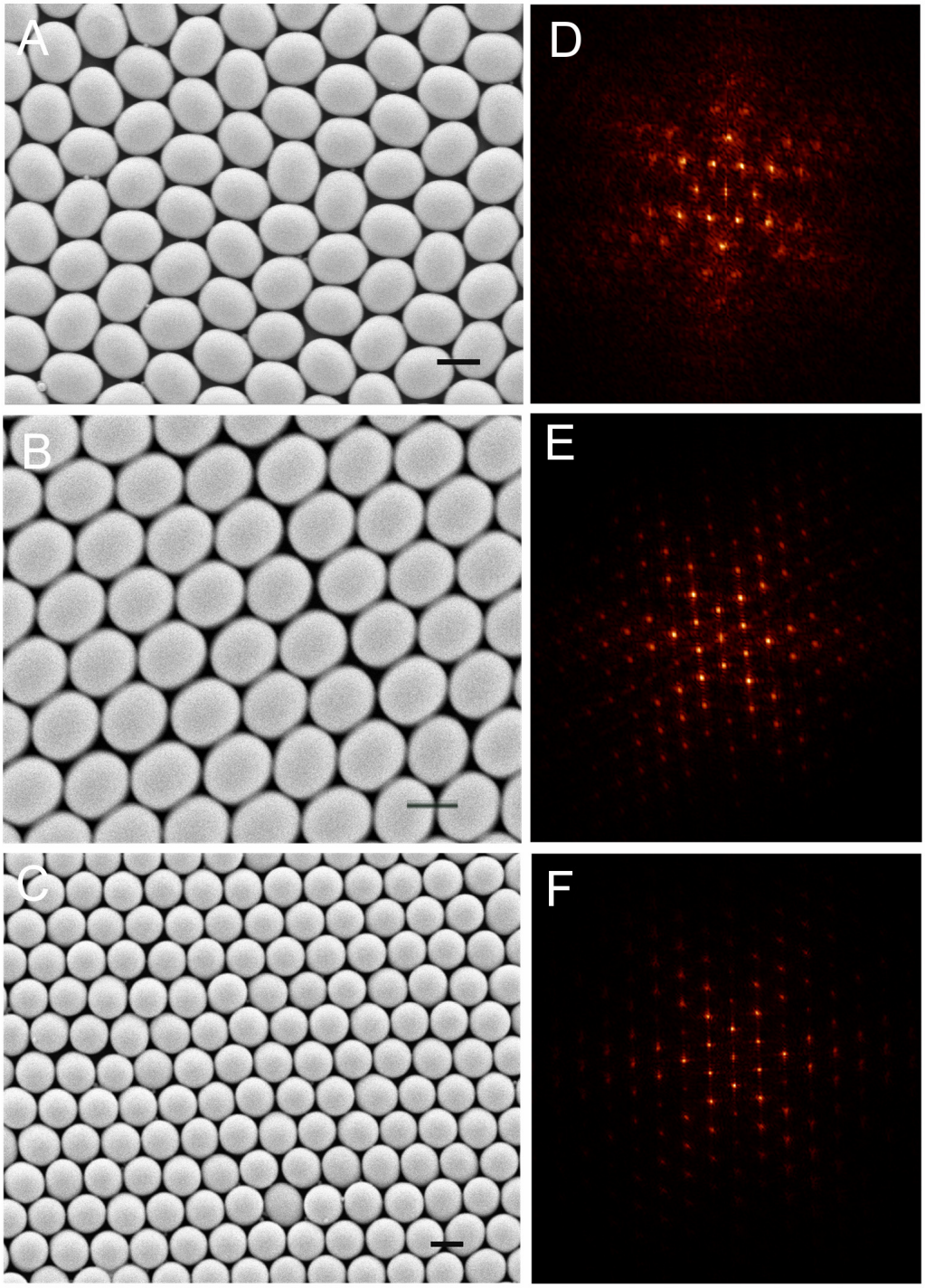

Figure 4.2. Monolayer films of spherocylinders. a) rotator, b) centered-rectangular, and c) hexagonal structures. Scale bars, 1 μm. d-f) FFT of the adjacent SEM image. Rotator and centered-rectangular grains were deposited from 0.05wt% suspension and hexagonal grains from 0.075wt% suspension.

Table 4.1. Lattice Parameters from Convective Assembly of Pear-Shaped Particles.

Structure	Lattice Vector* (μm)	Interaxial Angle (°)
Crystal (in-plane)	a_1 = 1.72 (0.06), a_2 = 2.08 (0.09)	65.5 (5.4)
Rotator	a_1 = 1.97 (0.17), a_2 = 1.99 (0.14)	63.0 (3.7)
Crystal (out-of-	$a_1 = a_2$ = 1.92 (0.09)	60 (2.7)

Selected area diffraction patterns (Figure 4.3) taken at normal incidence (θ_i) using a 488nm or a 785nm wavelength (λ) laser coupled through the objective lens of an optical microscope confirmed that strong coherent scattering maxima with characteristic symmetry could be obtained from the dry particulate films. The rows of particles function like a 2D diffraction grating and the position of peaks conformed to the grating equation,

$$\frac{\lambda}{d_{hk}} = n_1 \sin\theta - n_2 \sin\theta_i ,$$

where d_{hk} is the spacing between rows having Miller indices hk, θ is the diffraction angle measured from the surface normal, and n_1 and n_2 are the refractive indices of the media adjacent to the film (i.e., air and glass, respectively).[17] The 2-fold symmetry of the first order diffraction peaks in Figure 4.3d (pears) and Figure 4.3f (spherocylinders) suggest regions of particles lying with major axes parallel to the substrate surface, in either distorted hexagonal rotator or oblique/centered-rectangular structures. Figure 4.3e (pears) and Figure 4.3g (spherocylinders) show patterns with 6-fold symmetry consistent with the hexagonal packing of the out-of-plane particle alignments.

We previously found hexagonal out-of-plane and in-plane oblique structures for dimers with mildly-fused constituent lobes (L*=0.63) and small lobe anisotropy [(1-σ*)=0.25] using convective assembly.[18] Surface tension provides a "wedge-like" meniscus profile that restricts the height at the growth front of colloidal crystals. Nonspherical particles reorient to pack most efficiently in the region defined by the

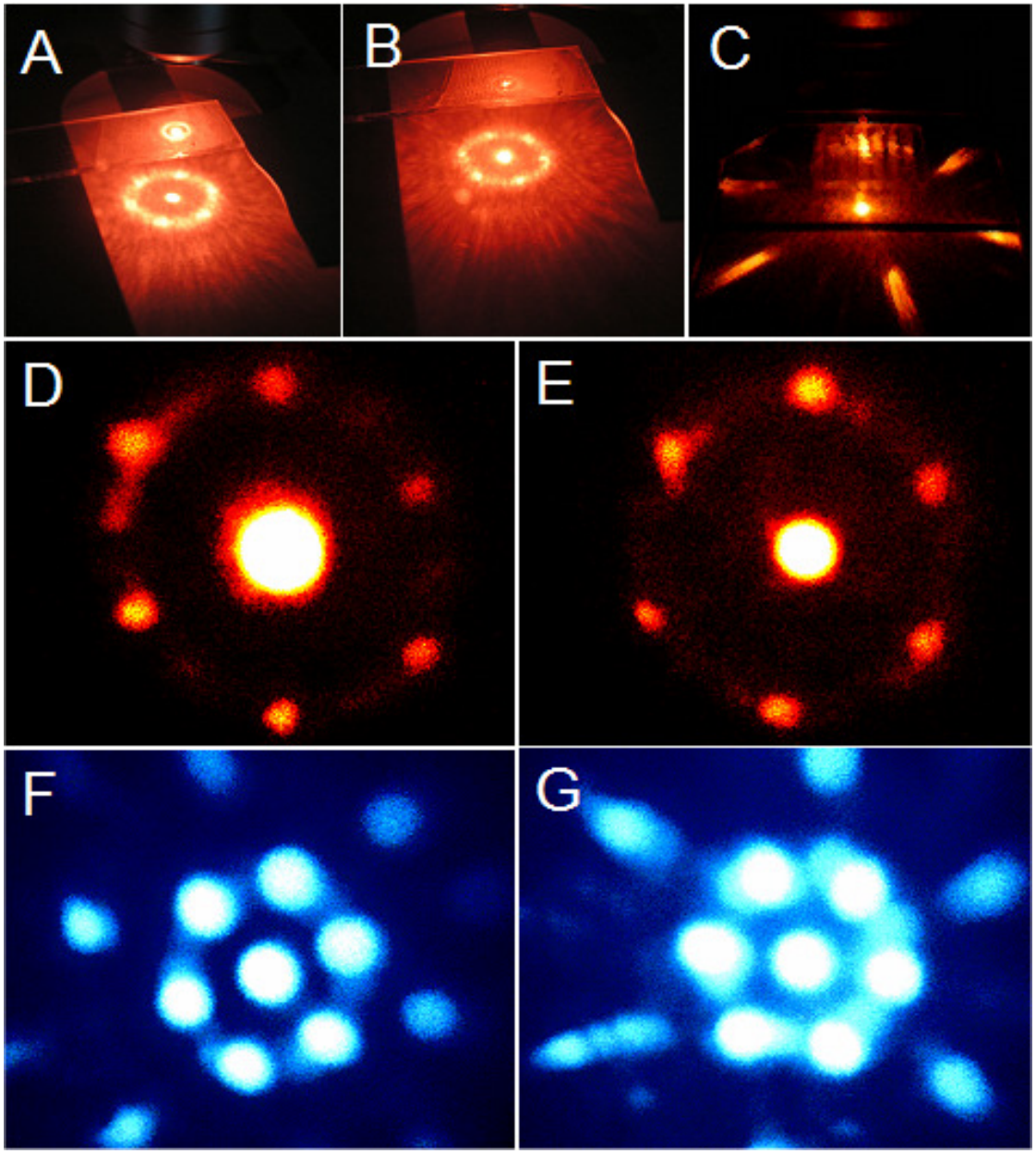

Figure 4.3. Selected area laser diffraction patterns from monolayer films. a) and d) pear shaped-particles, in-plane. b) and e) pear-shaped particles, out-of-plane. c) spheres, 989 nm diameter (Polysciences). f) spherocylinders, in-plane. g) spherocylinders, out-of-plane.

meniscus as it sweeps the substrate. Simulation studies on the phase behavior of dimers with a low degree of fusion between constituent lobes of different size suggest that orientationally-ordered structures form at high particle density and melt directly to the fluid phase.[7,8] Dimer shapes that are more globular (low L*), in contrast, were

determined by simulation to have a stable intermediate rotator phase before the transition into fluid.[7,10,19] Although several of the results from the literature were determined for 3D structures, that a rotator phase was isolated in the convectively assembled monolayers of pear- and spherocylinder-shaped dimers and not for the mildly lobe-fused dimer case is in general consistent with the predictions. To specifically investigate the disorder-order phase behavior of pear-shaped dimers confined to two dimensions (and in-plane), we performed Monte Carlo simulations in the isothermal-isobaric ensemble.[20] The simulations assume only "hard" core interactions and structure transitions via brownian motion or thermal fluctuations.

A comparison of structures from this simple limiting case with the experimental hindered rotator films provides a reference point to establish whether the complex interplay of forces involved in convective assembly[21-24] drives the structure significantly away from the configuration that would be obtained under equilibrium conditions. The pear-shaped dimer model was constructed as two overlapping spheres with $(1-\sigma^*)=0.1$ and $L^*=0.33$. The equation of state mapping the system pressure versus particle density [as the fraction of the surface coverage (SC) by particles] is shown in Figure 4.4. A fluid-solid phase transition occurred near SC~0.76, where the bond-orientational order parameter, ψ_6, jumps sharply upward (Figure 4.4, inset). ψ_6 measured the amount of hexagonal bond order based on the particle center of mass positions (numbering N) and was computed according to the expression,

$$\psi_6 = \left| \frac{1}{N} \sum_{N} \left(\frac{1}{N_b} \sum_{k=1}^{N_b} \exp(i6\theta_k) \right) \right|,$$

where N_b is the number of nearest neighbors and θ_k is the angle made by the nearest neighbor bond vector with an arbitrary fixed reference axis. Snapshots of the simulated structures confirmed an isotropic phase at low SC and a translationally-ordered rotator structure with hexagonal symmetry (Figure 4.5) at densities greater

than that at the melting point. On compression of the isotropic phase, the rotator structure was obtained with little hysteresis in the equation of state. The corresponding equation of state for spherocylinders is provided in the supplemental materials.

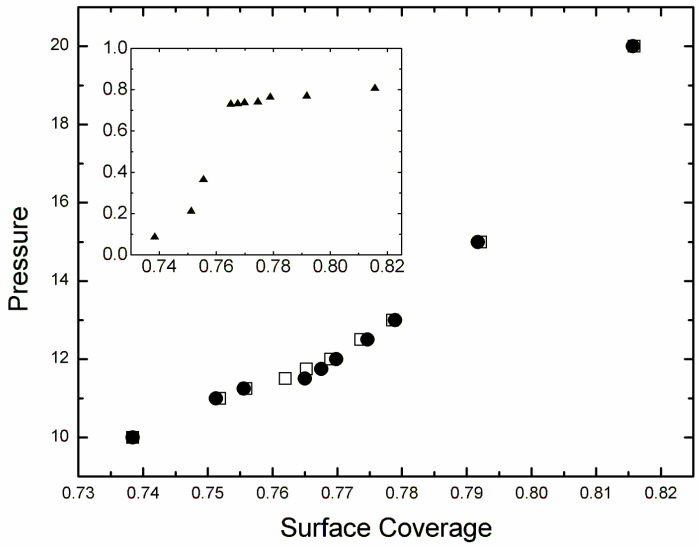

Figure 4.4. Simulated equation of state for pear-shaped particles from expansion (square) and compression (filled circle) runs. Inset shows the variation of ψ_6 order parameter with system density expressed as the surface coverage.

The radial distribution function, g(r), was plotted as a quantitative descriptor of the translational symmetry in the simulated and experimental rotator structures (Figure 4.6a). The g(r) is proportional to the probability of finding a dimer center of mass in a thin spherical shell at a distance r from a reference particle. For these comparisons, we calculated SC~0.86-0.87 for the experimental systems and used SC~0.81-0.82 for the simulated structures. The latter range was chosen to avoid the order-order transition to structures with a common orientation in the particle directors that was previously suggested (for homonuclear dimers) near density values approaching closest-packing.[19] In this way, we can compare the experimental hindered rotator structures with the simulated rotator structures in which the particles continue to rotate over 'time' (i.e., the time correlation of the orientations decays to zero).

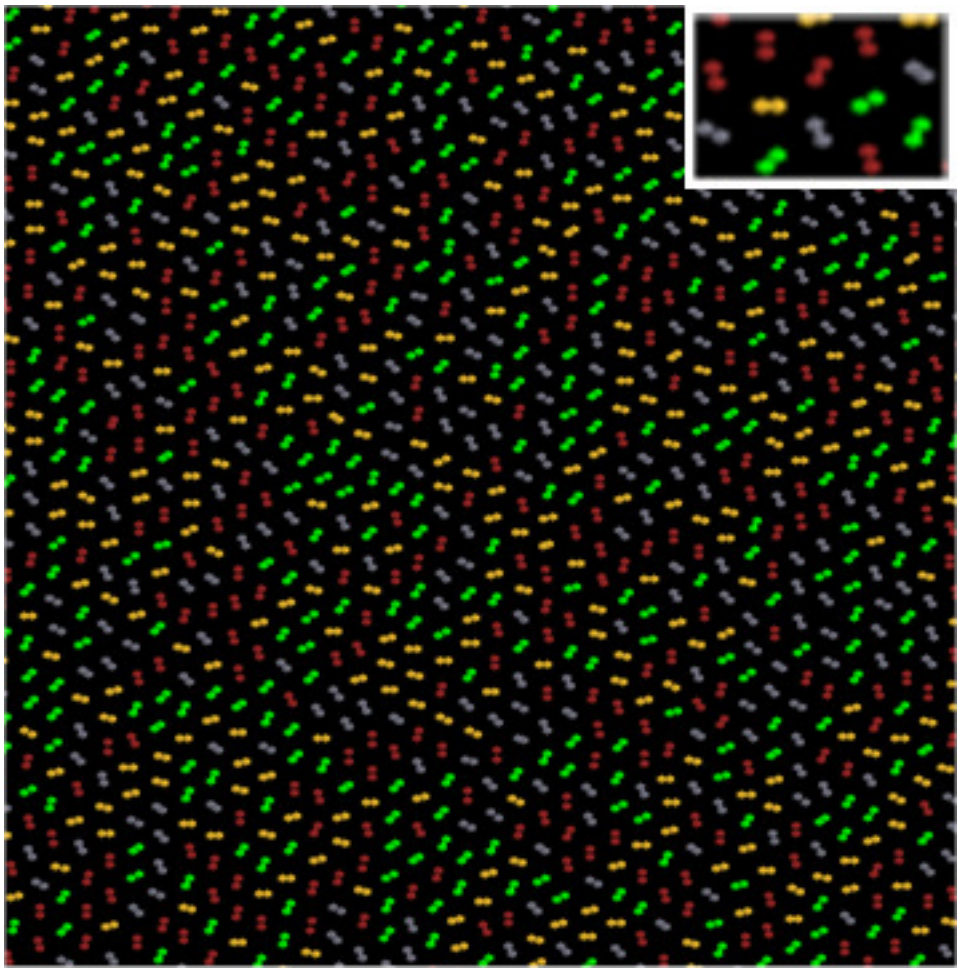

Figure 4.5. Simulated snapshot for 2D rotator structure of pear-shaped particles at SC=0.816. Colors indicate particle director orientations in ~36° ranges. Shape parameters of the dimer simulated are (1-σ*)=0.1 and L*=0.33. Lobe asymmetry is not rendered in the snapshot and lobe radius is an arbitrary unit.

The translational symmetry was greater for the simulated arrangements than for either of the convectively assembled films. The clear peaks and valleys in g(r) that are associated with positional order persisted to larger radial values consistent with higher quality long range order. This may be partially a reflection of the perfect size and shape uniformity of the simulated model particles. The location of the first three peaks for the experimental monolayer film of the pear-shaped colloids agreed well with the simulated structure, indicating an average distance to the first three nearest neighbors that was characteristic of the pear-shape based rotator structure. However,

we also note that the more irregular pear-like particle samples led to a reduced height of the peak reflecting the local configuration of first nearest neighbors (first peak). For the spherocylinder building blocks, g(r) showed more discrete peaks before reaching its asymptotic value of 1 as compared to the experimental film of pear-shaped particles, which implied better positional order in the fabricated spherocylinder colloid-based monolayer. The positions of the first six peaks determined from the spherocylinder assembly simulation agreed well with those from the spherocylinder films that were self-organized under controlled drying.

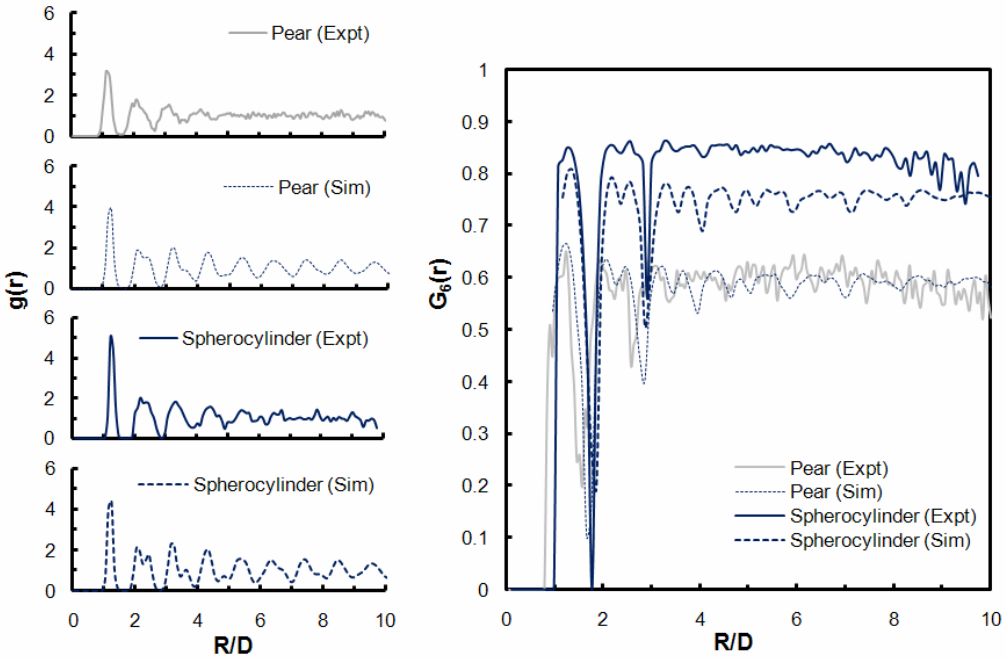

Figure 4.6. a) Radial distribution functions and b) bond-orientational correlation functions for 2D rotator structures of pear- and spherocylinder-shaped particles. Calculations made at SC=0.82 for simulated pear-shaped particles, SC=0.86 for pear-shaped particles in experiment, SC=0.81 for simulated spherocylinders, and SC=0.87 for spherocylinders in experiment.

The bond-orientational correlation function, $G_6(r) = \langle \psi_6(0)\psi_6(r) \rangle$, was also investigated for the rotator structures to further quantify the orientational symmetry (Figure 4.6b). Bond-orientation correlations were maintained over a long spatial range for both spherocylinders and pear-shaped colloids in simulation, though minor decay

at long range was evident for the experimental films as grain boundaries were approached. Furthermore, the local hexagonal bond order illustrated by the upper envelope of G_6 in the graphs was greater for spherocylinders than for pear-shaped particles. The magnitude of G_6 should retain a constant value of 1 for perfect crystalline hexagonal bond-order, whereas an exponential drop in G_6 to 0 with increasing r would indicate an isotropic fluid.[25] The spherocylinder G_6 plateau is somewhat higher in the experimental system than in the simulated one. This may arise from the high SC and fixed orientations in the dried sample, in contrast to the lower SC and dynamically rotating particles in the simulated system. The improvement in G_6 is not seen for the pear-shaped particles because the effect is presumably overwhelmed by the more polydisperse sample. We also calculated ψ_6 values of 0.79 and 0.81 for the experimental and simulated pear-based structures, respectively, and ψ_6 values of 0.88 and 0.87 for the experimental and simulated monolayer of the spherocylinders, respectively. In comparison, monodisperse "polyhedral" PMMA particles with random shape perturbations yielded a 2D ψ_6 value of 0.85 and PMMA spheres gave a 2D ψ_6 value of 0.95 when assembled by sedimentation into hexagonal structures.[26]

Capturing the rotationally-disordered structures in dry film form enables their use to pattern new meso-structures in functional materials. To this end, conformal amorphous germanium shells were grown on a spherocylinder-based monolayer with rotator structure by electron beam physical vapor deposition from a solid Ge source at a rate of 3.5Å/s. Figure 4.7 shows hollow hemi-spherocylinder Ge units after the nonspherical polystyrene colloids were removed from the film by oxygen plasma etch for 15 minutes. The concave side of a Ge film edge is shown in Figure 4.7b. Similarly, the crystal with centered-rectangular symmetry was "inverted" with Ge and is shown in Figure 4.7c. The high refractive index (n=4.1) and transparency of

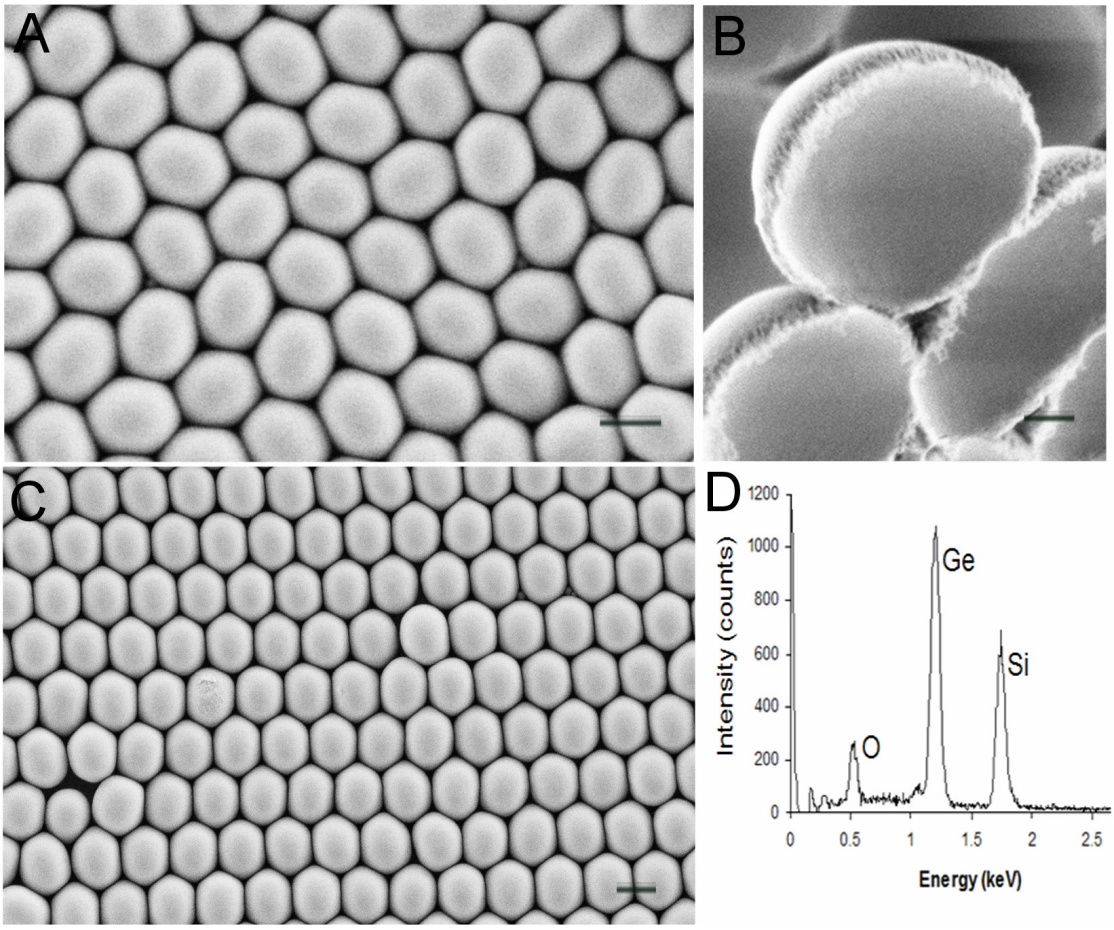

Figure 4.7. Germanium films of hollow hemi-spherocylinder units arranged in a) rotator and c) centered-rectangular structures. Scale bars, 1 □m. b) Concave side of Ge spherocylinder units showing hollow morphology. Scale bar, 200 nm. d) Elemental analysis by energy dispersive X-ray spectroscopy confirming germanium deposition.

crystalline Ge at wavelengths >1850nm may make these materials relevant in IR optical applications upon annealing.[27, 28]

In summary, the present report illustrates that introducing shape anisotropy in colloidal building blocks promotes the formation of diverse phases and broadens the film architectures readily accessible by a simple assembly approach. The experimental hindered rotator structures were found to be similar to those expected at thermodynamic equilibrium as predicted by simulation. Essentially both processes impart confinement, a controlled densification of the system and reversible

interparticle contacts during the assembly of the phase so that many local configurations can be sampled. While we focused on preparing dry film structures in this report, other assembly methods such as confinement cells in conjunction with particle surface modifications[29] could be utilized to develop nonspherical colloidal models of dynamic properties such as fast ion conduction in rotator structures— for example, as analogs of plastic crystal solid electrolyte materials.[30]

Supporting Information

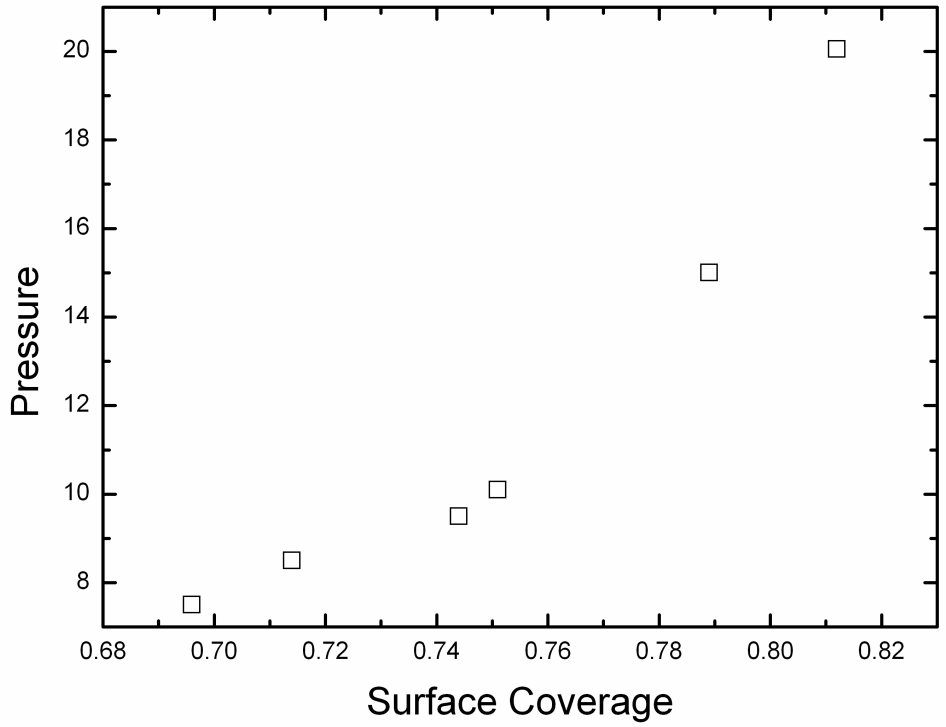

Figure 4.8. Simulated equation of state for spherocylinders in compression run. The break in the curve between SC=0.72 and 0.74 is indicative of a disorder-order phase transition.

Table 4.2. Lattice Parameters from Convective Assembly of Spherocylinders.

Structure	Lattice Vector* (μm)	Interaxial Angle (°)
Crystal (in-plane)	a_1 = 1.27 (0.03), a_2 = 1.47 (0.07)	62.2 (2.9)
Rotator	a_1 = 1.35 (0.07), a_2 = 1.39 (0.07)	60.7 (3.1)
Crystal (out-of-	$a_1 = a_2$ = 1.25 (0.04)	60.0 (2.2)

Experimental

Particle Synthesis

Nonspherical polystyrene colloids were prepared using a seeded polymerization method as described previously.[16] First, spherical PS cross-linked with 7.6% divinylbenzene (DVB, 55% isomer, Aldrich) were synthesized in a two-step process to a final size of 870 nm (coefficient of variation, CV=2.9%). The particle surfaces were coated with a hydrophilic acrylic acid layer[15] at a density of 1.78×10^{-21} g/nm^2, dialyzed overnight, and titrated to a pH of roughly 6.2 before subsequent use. To form the spherocylinders, 0.5 g of the seed particles were mixed with 1.5 mL styrene monomer, DVB55 (1 vol %), free radical initiator (V-65B, 1wt %, Wako), and 10 mg of hydroquinone inhibitor (HQ, Aldrich) and 8 mL of a 1wt% poly(vinyl alcohol) aqueous solution (PVA, 87-89% hydrolyzed, $8.5 \times 10^4 - 1.24 \times 10^5$ g·mol^{-1}, Aldrich). The suspension was allowed to swell for 24 hours at room temperature and polymerized at 70^{o}C for over 12 hours in a shaker bath operating at 120 rpm.

Sample Preparation

Particle suspensions were prepared with 18.2 MΩ ultrapure water (Barnstead, NanoPure Diamond). A stock 10 wt% polystyrene dimer suspension (Magsphere Inc., Pasadena, CA) was diluted to make 16mL aqueous suspensions with concentrations varied between 0.025 and 0.1 wt%. The suspensions were placed in glass petri dishes (2" diameter, 0.5" height) and sonicated for 1 min to ensure complete dispersion of the particles. The Petri dishes were cleaned with water and ethanol and dried under a flow

of nitrogen gas prior to use. Silicon and glass substrates were soaked in freshly prepared piranha solution (18M H_2SO_4 and 30 wt% H_2O_2 solution in a 2:1 v/v mixture) for 30 min, rinsed with water, and dried under nitrogen. Glass substrates were exposed to oxygen plasma for 10 min to increase their hydrophilicity before use. The substrates were immersed at an inclination (~14°) in the particle suspensions. Setups were left overnight in an oven at 50 °C for particle assembly to occur and for the liquid to completely evaporate. Ge deposition was carried out using a CVC SC4500 E-gun Evaporation System. The system pressure was 2×10^{-7} torr and the deposition rate was approximately 3.5 Å/s. The substrate temperature was maintained at 20 °C. The polymer template was removed with a flow of oxygen plasma for 15 min using a Branson/IPC P2000 Barrel Etcher.

Characterization

Scanning electron microscopy images were obtained with an LEO 1550 field emission scanning electron microscope at 1 kV. The films were sputtered with gold before characterization. The software WSxM version 3.0 Beta 7.5 (Nanotec Electronica) was used to generate fast Fourier transform images. Selected area laser diffraction was performed using a Renishaw inVia Raman system (Gloucestershire, U.K.) with a Leica DMLB optical microscope and either a 785nm diode laser (Renishaw, model HPNIR785, 300 mW) or a 488nm multi-line single mode Ar-Kr ion gas laser (Melles Griot, 43 Series Ion laser, model 543-AP-A01). Diffraction images were taken with a digital camera (Angstrom Sun Tech., model CFM-USB-3) mounted under the sample. The energy dispersive X-ray spectrometer (Bruker, Quantax, XFlash 3000 SDD, GmbH Berlin, Germany) accessory to the SEM was used for elemental analysis.

Detailed descriptions and schematics of the plane groups (c1m1, p1, c2mm, p6mm) used to specify the 2D crystal structures can be found in The International Tables of

Crystallography.[31]

Monte Carlo (MC) Simulations

In Monte Carlo (MC) simulations, dimers were allowed to find their equilibrium free energy minimum state using translation, rotation and volume moves at constant osmotic pressure and temperature. The system comprised 2000 pear-shaped dimers confined to a 2D surface. A non-overlap criterion was enforced among spheres belonging to different dimers. The system was expanded from a dense configuration with all lobes on a rectangular lattice such that the unlike (in size) lobes were next to each other. The system was expanded from its initial configuration by decreasing the pressure in steps. Approximately 2-4 x 10^6 MC cycles were used to equilibrate the system at each pressure. Each cycle was conducted with N/2 moves that displaced a randomly chosen dimer in 2D, N/2 moves that rotated a randomly chosen dimer on the surface and one volume move to adjust the volume of the simulation box. For compression runs, dimers were placed randomly in a box at very low density as the initial state and the pressure was raised stepwise. The acceptance of trial moves was based on the Metropolis criteria; for example, particle displacement and rotation moves were accepted with a probability given by $e^{-\beta[U(n)-U(o)]}$ where $\beta = 1/k_B T$, U(n) is the energy of the system after the move, and U(o) is the energy of the system before the move.[20] The equilibrated configurations were visualized using Rasmol. The equation of state was mapped by plotting the dimensionless osmotic pressure (P*) as a function of surface coverage (SC), with SC defined as the fraction of the total area of the simulated monolayer surface occupied by dimers, $SC = NA_{particle} / A_{monolayer}$, where N is the number of particles, $A_{particle}$ is the projected area occupied by a particle and $A_{monolayer}$ is the monolayer surface area. Additionally, P* was calculated from Pa^3/ε, where a is the minimum distance between dimer centers of mass and ε is an arbitrary

energy parameter. The procedures described above were applied to simulate spherocylinders under compression with the exception that the spherocylinder was modeled as two highly fused spheres of equal diameter, i.e., L*=0.25 and (1-σ*)=0. To study the time correlation of the dimer orientation, the orientations of the dimers at the end of predefined intervals (100,000 MC cycles) were stored and an autocorrelation function was calculated for each interval. The orientation correlation function is defined as $< \cos(\theta_j(0)) \cos(\theta_j(i)) >$ where $\theta_j(i)$ is the angle made by the dimer j with the x-axis at the end of time interval i.

REFERENCES

1. Y. Zhang, S. Wang, M. Eghtedari, M. Motamedi and N. A. Kotov, *Adv. Funct. Mater.*, 2005, **15**, 725-731.

2. D. M. Kuncicky, S. D. Christensen and O. D. Velev, *Appl. Spectr.*, 2005, **59**, 401-409.

3. T. Gorishnyy, J.-H. Jang, C. Y. Koh and E. L. Thomas, *Appl. Phys. Lett.*, 2007, **91**, 121915-1 - 121915-3.

4. S.-M. Yang, S.-H. Kim, J.-M. Lima and G.-R. Yi, *J. Mater. Chem.*, 2008, **18**, 2177-2190.

5. M. Maldovan, C. K. Ullal, W. C. Carter and E. L. Thomas, *Nat. Mater.*, 2003, **2**, 664-667.

6. K.W. Wojciechowski, *Phys. Rev. B*, 1992, **46**, 26-39.

7. C. Vega, E. P. A. Paras and P. A. Monson, *J. Chem. Phys.*, 1992, **96**, 9060-9072.

8. M. Marechal and M. Dijkstra, *Phys. Rev. E*, 2008, **77**, 061405-1 – 061405-10.

9. A. C. Branka and K. W. Wojciechowski, *Phys. Rev. Lett.*, 1983, **50**, 846-849.

10. P. Bolhuis and D. Frenkel, *J. Chem. Phys.*, 1997, **106**, 666-687.

11. E. B. Mock and C. F. Zukoski, *Langmuir,* 2007, **23**, 8760-8771.

12. K. W. Wojciechowski, K. V. Tretiakov and M. Kowalik, *Phys. Rev. E*, 2003, **67**, 036121-1 – 036121-14.

13. A. Alderson, J. Rasburn, S. Ameer-Beg, P. G. Mullarkey, W. Perrie and K. E. Evans, *Industrial & Engineering Chemistry Research,* 2000, **39**, 654-665.

14. Z. Feng, X. Zhang, S. Feng, K. Ren, Z.-Y. Li, B. Cheng and D. Zhang, *J. Opt. A: Pure Appl. Opt.,* 2007, **9**, 101-107.

15. E. B. Mock, H. De Bruyn, B. S. Hawkett, G. S. Gilbert and C. F. Zukoski, *Langmuir*, 2006, **22**, 4037-4043.

16. J. W. Kim, R. J. Larsen and D. A. Weitz, *J. Amer. Chem. Soc.* 2006, **128**, 14374-14377.

17. I. D. Hosein and C. M. Liddell, *Langmuir*, 2007, **23**, 8810-8814.

18. I. D. Hosein and C. M. Liddell, *Langmuir,* 2007, **23**, 10479-10485.

19. K. W. Wojciechowski, *Phys. Lett. A*, 1987, **122**, 377-380.

20. D. Frenkel and B. Smit, *Understanding Molecular Simulation. From Algorithms to Applications*, 2nd ed.; Academic Press: New York, 2002.

21. K. Nagayama, *Colloids Surf. A*, 1996, **109**, 363-374.

22. Y. A . Vlasov, X. Z. Bo, J. C. Sturm, D. J. Norris, *Nature,* 2001, **414**, 289-293.

23. Y.H. Ye, F. LeBlanc, A. Hache, V. Truong, *Appl. Phys. Lett*. 2001, **78**, 52-54.

24. S. Wong, V. Kitaev, G. A. Ozin, *J. Am. Chem. Soc*. 2003, ***125***, 15589-15598.

25. R. A. Segalman, A. Hexemer, R. C. Hayward and E. J. Kramer, *Macromolecules,* 2002, **36**, 3272-3288.

26. R. P. A. Dullens, M. C. D. Mourad, D. G. A. L. Aarts, J. P. Hoogenboom and W. K. Kegel, *Phys. Rev. Lett.*, *2006*, **96**, 028304-1 - 028304-4.

27. H. Mıguez, F. Meseguer, C. Lopez, M. Holgado, G. Andreasen, A. Mifsud and V. Fornes, *Langmuir*, 2000, **16**, 4405-4408.

28. R. G. Shimmin, R. Vajtai, R. W. Siegel and P. V. Braun, *Chem. Mater.*, 2007, **19**, 2102-2107.

29. M. E. Leunissen, C. G. Christova, A.-P. Hynninen, C. P. Royall, A. I. Campbell, A. Imhof, M. Dijkstra, R. van Roij and A. van Blaaderen, *Nature*, 2005, **437**, 235-240.

30. D. R. MacFarlane and M. Forsyth, *Adv. Mater.*, 2001, **13**, 957-966.

31. *The International Tables of Crystallography*, Volume A: Space-Group Symmetry, Fourth Edition; Kluwer Academic Publishers, Dordrecht, 1996.

CHAPTER 5

CONTROLLED MONOLAYER STRUCTURE FROM ASYMMETRIC DIMER COLLOIDS BY DIP COATING

Abstract

Monolayer films from polystyrene dumbbell colloidal particles were fabricated on silicon substrates by computer controlled dip coating. The principle process parameters were particle suspension concentration and crystallization rate. Dumbbell shapes with different degrees of fusion were characterized. Systematically varying the concentration and substrate withdrawal rate determined the particle orientation and monolayer structure. The convective assembly equation was used to predict the deposition parameters for each structure. Parameter maps were constructed, relating the monolayer structure type to the assembly parameters.

Introduction

Two-dimensional self-assembly of particle-based structures is an attractive fabrication method for rapidly and cost-effectively producing materials and devices, which has been exploited in nano-sphere lithography[1], photonic devices,[2, 3, magnetic memory storage [4] and biosensing technology [5]. However, the diversity of structures attainable is highly dependent on the particle building block used. Spherical particles, currently the primary colloidal basis employed, produce only close-packed arrangements in two dimensions [6, 7]. Enabling the technique to produce more complex structures is required.

Changing the shape of the colloidal particle has the potential to broaden the diversity of self-assembled monolayer structures achievable. A non-spherical particle

system's tendency towards high packing density favors the formation of structures with both positional and orientational order. The free volume entropy gained by the system more than offsets the loss in orientational entropy. As examples, computational studies show that disc[8], rod[9], ellipsoidal[10], pentagon[11] and dumbbell[12-16] shaped particles can form ordered structures with higher structural complexity than attainable for spheres. However, the realization of such structures has been challenging and experimental developments trail behind the predictions.

Convective assembly is one method to assemble colloidal particles into ordered two-dimensional structures, and was recently demonstrated to produced 2D ordered arrays from hexagonally shaped nanoplates[28], hemispherical caps[29] and dumbbell shaped colloids [30, 31]. Highly fused dumbbells assembled into a two-dimensional rotator structure when oriented parallel to the substrate surface. The particles crystallized on two-dimensional oblique lattices, reducing the symmetry of the structure to 2-fold from the conventional 6-fold seen in spherical systems. Crystallization on hexagonal lattices was also observed when particles oriented perpendicular to the substrate using this controlled drying approach.

Specifically, convective assembly entails the ordering of particles in the meniscus region of a solvent wetted surface. Particle crystallization in a thin wetting layer follows a process similar to densifying the particle system in confined regions between solid surfaces [17]. Under confinement, the system undergoes a free volume Alder transition [18], with the particles arranging in the most densely packed configuration between the substrate and meniscus (i.e. air-liquid interface). Spherical particles produce hexagonal close packing in the monolayer when the confining height is comparable to the particle diameter[26]. Stacking in an ABC fashion of these layers (i.e. cubic close packing) has been observed for confinement heights greater than the particle diameter, with tetragonal packing in the transition between layers [19-22].

The intermediate tetragonal phase more closely conforms to the meniscus height in the transition region [26] between layers of the same planar structure, however it persists for only a few lattice constants due to mechanically instability. Molecular dynamics and Monte Carlo simulations have also confirmed such phases under confinement [24, 25].

Confining meniscus heights have been primarily exploited to produce crystals with a tunable number of layers [17, 23]. Furthermore, the correlation of structure and film height with the convective assembly parameters was investigated [27], in the multilayer regime for spherical colloids. Under fixed temperature and humidity conditions, concentration values were determined for crystallizing the colloidal monolayers, bilayers and trilayers as well as the transitional tetragonal phase.

In the monolayer regime, where unlike spheres non-spherical particles produce more than one self-assembled structure, the correlation of the convective assembly parameters with the film structure and height has not been examined. The present study of asymmetric dimer-shaped colloids examines the role of the deposition parameters to induce a variety of packing arrangements and particle orientations in the monolayer films. 'Peanut' and 'pear'-shaped dimers with more highly fused lobes were examined to observe the shape effect on the assembly parameters. The orientation of the particles with respect to the long axis is referred to as in-plane and out-of-plane for orientation parallel and perpendicular to the substrate, respectively. Operational 'structure maps' are developed for the particles in the monolayer regime. The self-assembly of particles is also examined in a pinned meniscus region on a flat surface by optical microscopy (OM), to further illustrate the structure formation along the meniscus slope.

Background

Convective assembly refers to the evaporation facilitated process of particle accumulation and arrangement on a surface in the location of the wetting region of the meniscus near the solvent contact line. Evaporation in this region induces a flow of solvent and particles from the bulk, allowing the process to continue as the meniscus sweeps the substrate. Under steady state conditions the mass balance of solvent and particle fluxes leads to an equation [17] for the rate of crystallization (v_c),

$$v_c = \frac{\beta L v_e}{(1-\varepsilon)} \frac{\varphi}{t_i(1-\varphi)}$$

where L is a characteristic meniscus length over which evaporation occurs, v_e, is the rate of solvent evaporation, ε is the porosity of an assembled monolayer, t_i is the particle film thickness of structure of type i, and φ is the particle volume fraction in suspension. For 2D structures it is reasonable to assume the evaporation is negligible. In the case of mechanically withdrawn substrates, the crystallization rate is equal to the withdrawal rate v_w. The term $\beta L v_e$ can be grouped into one experimental fit parameter K [26],

$$v_c = \frac{K}{(1-\varepsilon)} \frac{\varphi}{t_i(1-\varphi)} \qquad (1)$$

In case of multilayer colloidal crystals, t_i is directly related to the number of layers k, $t_i = kd$, where d is the thickness of one layer. However, in the monolayer regime the film thickness depends on the orientation of the particle and the vertical height it renders from the surface of the substrate. For the case of a dumbbell, the film thickness of in-plane and out-of-plane structures would be, respectively, the diameter of the large lobe and the total length of the particle along the long axis. Given these values and the porosity of the packing arrangements they produce, the structural data can be fit to a set of operational curves based on equation 1. See supporting information for porosity determination.

Experiment

Materials

Concentrated suspensions (~10wt) of pear- and peanut-shaped colloids were obtained from Magsphere Inc. (CA, USA). The particle solutions were used as received.

Suspension and Substrate Preparation

Particle suspensions were prepared with 18.2 MΩ ultrapure water (Barnstead, NanoPure Diamond). 3.5mL of each suspension was placed in a separate vial and sonicated for 1 minute to ensure complete dispersion of the particles. The vial was cleaned with water and ethanol, and dried under a flow of nitrogen gas prior to use. Silicon substrates were soaked in freshly prepared piranha solution (18M H_2SO_4 and 30 wt% H_2O_2 solution, in a 2:1 v/v mixture) for 30 minutes, rinsed several times with water, and dried under nitrogen.

Dip Coating

Particle films were dip coated on to silicon substrates using a computer controlled dip coating system (Nima DC Mono 75) with an immersion speed of 1 mm/min (16.66μm/s) and withdrawal speeds between 0.05-0.9 mm/min (0.33μm/s-15μm/s). Dispersion of the particles in the solvent was maintained through magnetic stirring (~60rpm).

Meniscus Pinning Observation

Pinned meniscus regions wetting flat substrates were produced in glass Petri dishes (2" diameter 0.5" deep). The dish was plasma cleaned for 10min prior to use. 400μL of a 0.125vol% suspension was spread over the Petri dish surface and allowed

to dry at room temperature while mounted on the microscope stage for observation.

Imaging

Optical microscope (OM) images were taken with a digital camera mounted on an Olympus BX51 microscope with reflected light. Scanning electron microscope (SEM) images were obtained with a Zeiss ultra high resolution field emission scanning electron microscope. The films were sputtered with gold before SEM characterization.

Results & Discussion

Monolayer structure

Both particles showed three distinct large scale structures within the range of concentrations and withdrawal rates investigated. Figure 5.1 shows OM and SEM images of the films deposited from 8 vol% peanut suspensions at decreasing withdrawal rates. The insets show Fast Fourier Transforms (FFT) of the SEM images. At high withdrawal rates the substrate was covered with a continuous monolayer of particles oriented in-plane (Figure 5.1a). The structure was largely amorphous as indicated by the characteristic amorphous ring pattern in the in FFT. Small crystalline regions (~15um) were observed, consisting of both orientational order and positional order on an oblique lattice. The FFT pattern of these local regions showed oblique symmetry, confirming the symmetry of these local real space structures.

When the withdrawal rate was decreased, a change in the film structure was observed from a continuous in-plane particle monolayer to a periodic stripe pattern consisting of two different structural regions. One region consisted of out-of-plane

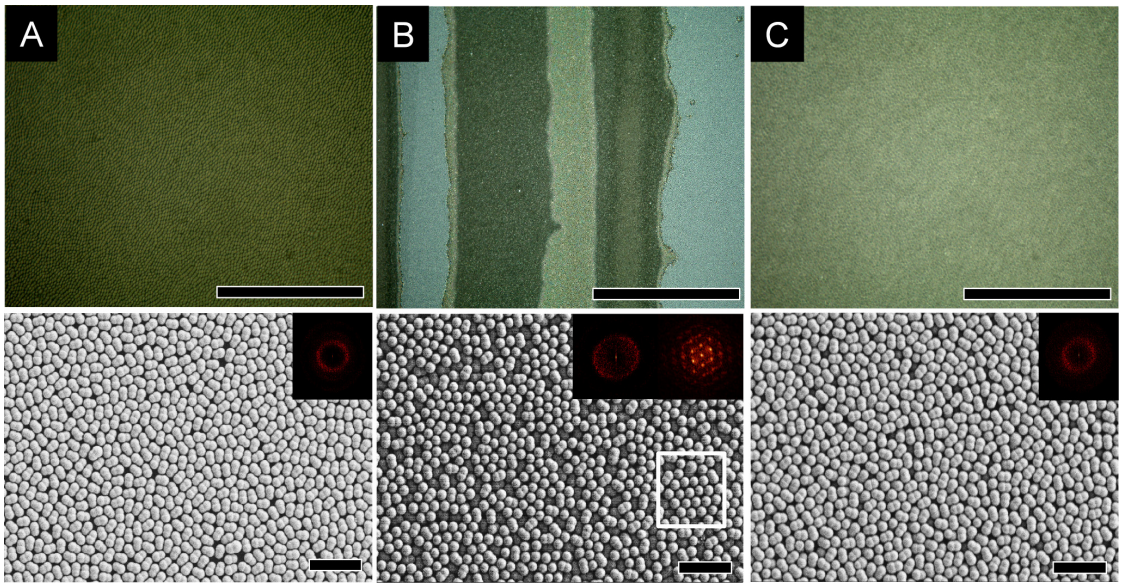

Figure 5.1. OM and SEM images of the peanut monolayers assembled from 8vol% suspensions at decreasing withdrawal rates. A) Continuous monolayer of in-plane oriented particles, B) Stripes consisting of out-of-plane particles or bilayer. The colors of the regions are blue, greenish yellow and dark green for the in-plane monolayer, out-of-plane monolayer and bilayer, respectively. C) Continuous bilayer. Corresponding SEM are shown below each photo. Insets show FFTs of the images. White outline indicates the region use to determine a local FFT. OM and SEM scale bars represent 500μm and 10μm, respectively.

oriented particles assembled on a hexagonal lattice (Figure 5.1b). The FFT indicates the hexagonal symmetry of the region. The single crystals in the region were approximately 10 interparticle distances wide. The second structure was a disordered bilayer. Both structures existed as adjacent regions within a stripe extending to both sides of the substrate. Interchanging between the two structures was also observed in stripes. The space separating adjacent stripes was covered with the in-plane particle oriented monolayer. The striping is attributed to the stick-slip motion of the assembly front due to pinning of the solvent contact line[32] or due to differences in wetting from the inhomogeneous surface caused by the deposited material.[33] The spacing between and width of the stripes did not change significantly with change in the withdrawal rate.

Further decrease in the withdrawal rate produced a continuous bilayer structure

(Figure 5.1c). This structure was also amorphous as confirmed by the corresponding FFT image. The particles had complete orientational freedom in the structure. Figure 5.2 shows OM and SEM images for the pear assemblies produced from 7 vol% suspensions. A similar trend was observed in the film structure as with the peanuts, with the structure changing from in-plane to out-of-plane (striping) to bilayer with decreasing withdrawal rate. The monolayer of the in-plane pears had positional order with hexagonal symmetry and no orientational order, characteristic of a two-

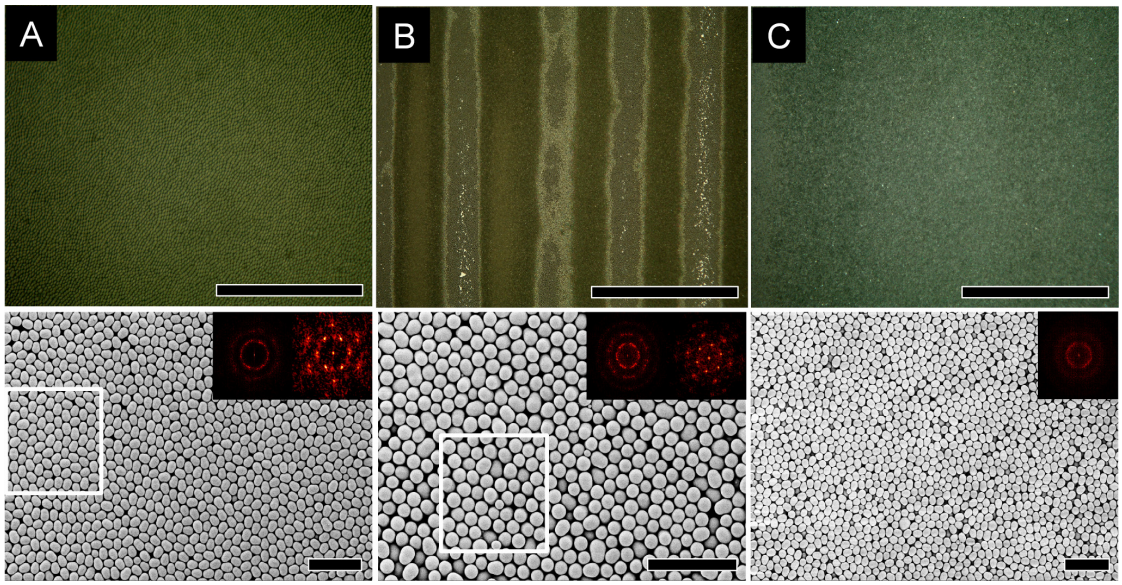

Figure 5.2. OM and SEM images of the pear monolayers assembled from 8vol% suspensions. A) Continuous monolayer of in-plane oriented particles, B) Stripes consisting of out-of-plane particles or bilayer. The colors of the regions are blue, greenish yellow and dark green for the in-plane monolayer, out-of-plane monolayer and bilayer, respectively. C) Continuous bilayer. Corresponding SEM are shown below each photo. Insets show FFTs of the images. White outline indicates the region use to determine a local FFT. OM ansd SEM scale bars represent 500μm and 10μm, respectively.

dimensional rotator structure. Small regions were observed with a fully crystalline state (positional and orientational order) having oblique symmetry.

Examination of the SEMs (Figure 5.3) indicated that an unstable packing arrangement was present in the transition region from out-of-plane and to bilayer

structure. In this region, the pears packed on a square lattice characteristic of the tetragonal phase observed for spheres. The particles had no orientational order on the square lattice sites. The peanuts also showed a less densely packed disordered bilayer phase. These structures only persisted for a few lattice constants.

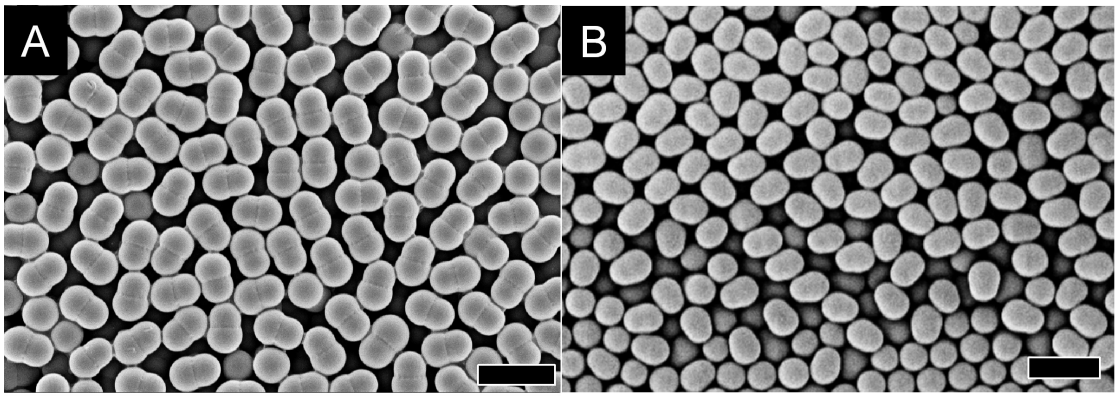

Figure 5.3. Colloidal structure in the transition region from out-of-plane to bilayer for A) peanut and B) pear. Scale bars are both 4μm.

The structural data was used to construct plots of the film structure as a function of deposition rate (v_w) and particle volume fraction in suspension (φ). Figure 5.4 show the operational 'phase diagrams' for both particles used in this study. The plotted curves show the expected withdrawal rates and particle concentrations to produce out-of-plane and bilayer structures based on equation 1. Cross-sectional SEM images were used to establish the bilayer thickness for determination of the bilayer curve. The heights and porosities of the structures are shown in Table 5.1. The curves confirmed the experimental data for film structure and their corresponding deposition parameters. The in-plane monolayer structure was predominant at low concentrations and high withdrawal rates (top left region of the parameter space) and tended towards out of plane and bilayer structure with higher concentration and lower withdrawal rate (bottom right of the parameter space). The withdrawal rate calculated from equation 1 represented the boundary in parameter space between parameters which produce in-

plane and out-of plane or out-of-plane and bilayer, indicating the onset of a different structure. The curves also represented the upper bounds of the withdrawal rate values, or in other words the highest rate at which each structure formed. Each structure persisted for lower withdrawal rates(down vertically, lower withdrawal rates) or for higher concentrations (left to right horizontally, higher concentrations) until the deposition parameters cross the next operational curve.

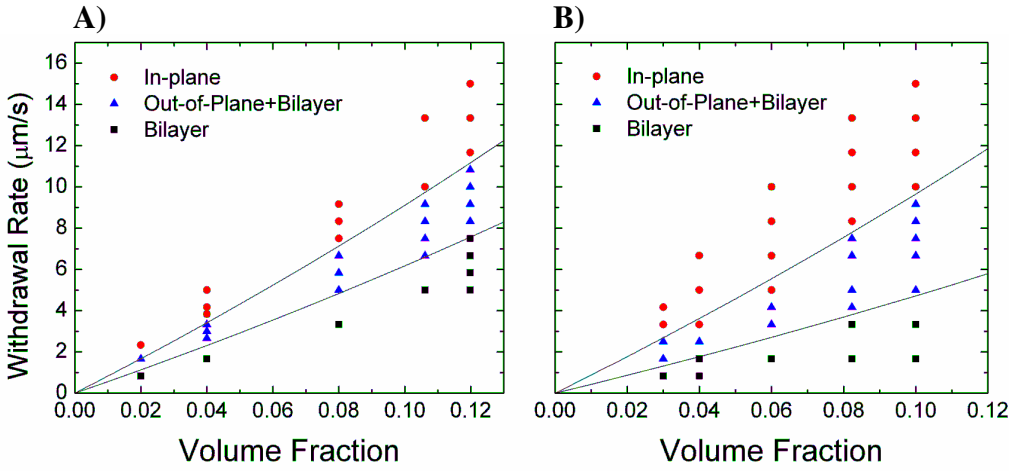

Figure 5.4. Operation 'phase diagrams' showing film structure as a function of withdrawal rate and particle suspension volume fraction. A) Peanut-shaped particles. B) Pear-shaped particles. The curves show the expected rate of deposition at each concentration where a particular monolayer structure is expected to form.: (●) in-plane monolayer, (▲) out-of plane monolayer and (■) for bilayer, determined from equation 1. The K fitting parameter is the same for both curves for each particle.

Table 5.1. Particle film characteristics.

Particle	Structure	Thickness (μm)	(1-ε)
Peanut	In-plane	1.87	0.47
	Out-plane	2.71	0.54
	Bilayer	3.99	
Pear	In-plane	1.55	0.41
	Out-plane	1.79	0.60
	Bilayer	3.4	

Data points between the two curves represent conditions lead to striping, and

the out-of-plane structure could not be isolated from the production of bilayer regions. The $h(1-\varepsilon)$ terms from equation 1 of each structure were close in value, consequently, it was difficult to differentiate between the structures via tuning the concentration. The stick and slip nature of the assembly also induced bilayer formation. Physically the meniscus stops moving and particles continue to fill into the region shifting the crystallization further away from contact line to regions where the meniscus height is greater, leading to thicker layers. The deposition of a single structure depends on the continuous sweep of the meniscus over the substrate. When the meniscus is pinned, according to equation 1, v_w tends to zero. To balance the equation, $h(1-\varepsilon)$ must increase, resulting in thicker films.

In comparison between the two particle shapes, the pear data required lower concentrations or higher deposition rates to achieve the same corresponding structures as the peanut, in agreement with equation 1. The particle size was smaller, and led to thinner films when oriented in-plane. As well, the more highly fused pear shape resulted in a smaller film height when oriented out-of-plane, and also for the bilayer.

In general the data coincided well with the predicted curves constructed from equation 1, showing that fluxes can be used to accurately predict the structural and thickness dependence on withdrawal rate and concentration in the *monolayer regime*. It also demonstrates that the monolayer structure can be controlled by tuning the assembly parameters in accordance with the operational curves.

The thin wetting layer of a pinned meniscus on a horizontal surface was examined during the influx of particles. A drop of suspension was placed on a substrate and allowed to spread over the surface until it reached a fixed radius. Over time with solvent evaporation the circular droplet contracted in radius, leaving a film on the surface of the substrate in the form of rings. The contact line of the solvent was observed to slip and move inward toward the center of the drop and only became

pinned in one new location. Immediately after pinning was established, the influx of particles into the region and their self-assembly was observed. In this region, the meniscus height above the surface increases in the direction away from the contact line. With the slope and shape of meniscus profile fixed during this pinning, the setup is similar to a fixed wedge-cell.

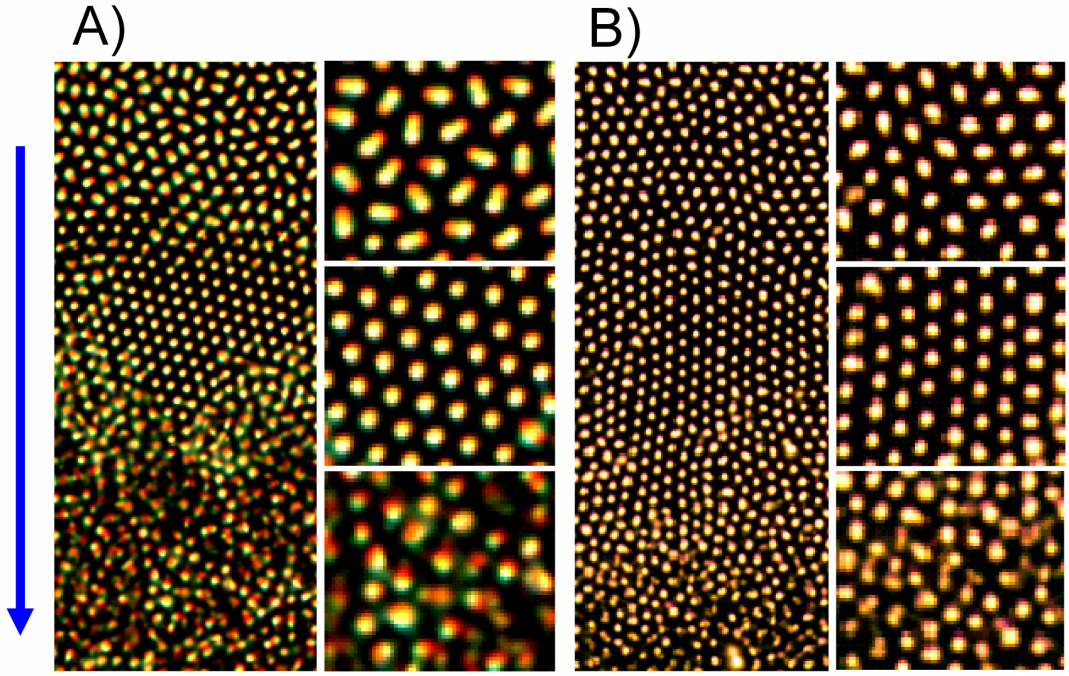

Figure 5.5. Optical microscopy of the confinement of particles at a pinned meniscus region on a horizontal surface. A) Peanut and B) Pear. Direction of increasing meniscus height is indicated by the arrow. The particles change orientation and pack differently to maximize packing density as the meniscus height increases, producing in-plane (top), out-of-plane (middle) and bilayer (bottom) structures. Second column of both A and B show higher magnification images of the structures.

Figure 5.5 shows optical microscopy images of the assembled structure for both pear and peanut shapes. As a result of the increasing meniscus height in this region (indicated by the arrow), all three particle packing arrangements were observed: in-plane, out-of-plane and bilayer. This directly shows the dependence of the structures on the confined height in the region. The particles were fixed in their positions with minimal Brownian motion. A small population of out-of-plane oriented particles

reoriented in-plane over time, most likely caused by a slight recession of the meniscus from solvent evaporation.

Conclusion

Colloidal monolayers with in-plane particle orientation, out-of-plane particle orientation and bilayer structure were formed by dip-coating particle films from pear and peanut shape particles. The monolayer structure was tuned via the concentration of the particle suspension and the withdrawal rate, and followed the steady-state flux convective assembly equation. Optical microscopy observation of a pinned meniscus region confirmed that the particle structure adjusted to conform to the meniscus height. This work provides insight into the use of convective assembly for monolayer structural control in the case of non-spherical colloidal self-assembly.

Supporting Information

Modeling Particle Volume & Film Porosity

The dumbbell shape was modeled as two overlapping spheres with radius R_1 and R_2 and center-to-center distance L, determined from SEM images. The volume of the lens shaped region where the spheres overlap is given by:

$$V_{lens} = \frac{\pi(R_1 + R_2 - L)^2\left(L^2 + 2LR_2 - 3R_2{}^2 + 2LR_1 + 6R_1R_2 - 3R^2\right)}{12L}$$

The particle volume is the sum of the spherical lobe volumes minus this volume,

$$V_{particle} = 4\pi\left(R_1{}^3 + R_2{}^3\right) - V_{lens}$$

The porosity of the films can be expressed as,

$$\varepsilon = 1 - V_{particle} / V_{unitcell}$$

where $V_{unitcell}$ is the volume of the unit cell occupied by one particle,

$$V_{unitcell} = A_{unitcell} h$$

where $A_{unitcell}$ is the average area occupied by one particle in the plane parallel to the substrate and h is the height of the unit cell. The diameter of the larger lobe and the length of the particle along its long axis are used for the in-plane and out-of-plane film heights, respectively. For a crystalline film, $A_{unitcell}$ is the area of the primitive cell of the 2D lattice produced by the particles. The porosity of the bilayer was assumed to be the same as in the in-plane structure (i.e. modeling it as the stacking of two oblique lattices).

Calculating the unit cell area for out-of-plane hexagonal lattice

In this case the lattice constant is assumed to be the diameter of the larger particle. Therefore, the unit cell area is $(\sqrt{3}/2)D_1^2$.

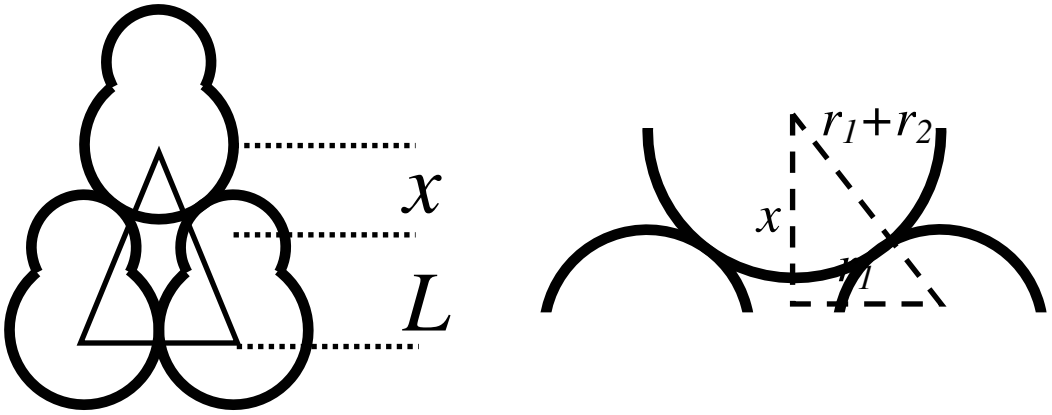

Figure 5.6. Schematic of close packing of dimer monolayer structure with in-plane particle orientation.

Calculating the unit cell area for in-plane oblique lattice

The crystal lattice in this case is oblique, and the shape of the primitive unit cell is a parallelogram. Figure S1 shows the close packing arrangement of three dumbbells and an enlarged view of the contact between the two small lobes of one particle with the large lobe of another. The triangle represents half of the unit cell, and

its area can be determined from the particle shape parameters. The area was determined by calculating the height of the triangle shown in Figure S1, which can be expressed as $x + L = \sqrt{r_2^2 + 2r_1r_2} + L$, and multiplying it by the base of the triangle, D_1. Therefore the area of the unit cell is $2D_1(\sqrt{r_2^2 + 2r_1r_2} + L)$.

REFERENCES

1. D. G. Choi, H. K. Yu, S. G. Jang, S. M. Yang, *J. Am. Chem. Soc.* **126**, (2004), 126, p. 7019.
2. R. Mafouana, J. L. Rehspringer, C. Hirlimann, C. Estournes, K. D. Dorkenoo, *Appl. Phys. Lett.* **85**, (2004), p. 4278.
3. Y. Zhao, I. Avrutsky, *Proceedings SPIE*, **4110**, (2000), pp. 177-181.
4. S. H. Sun, C. B. Murray, D. Weller, L. Folks, A. Moser, *Science* **287**, (2000), 1989.
5. O. D. Velev, E. W. Kaler, *Langmuir* **15**, (1999), pp. 3693-3698.
6. Y. Xia, B. Gates, Y. D. Yin, Y. Lu, *Adv. Mater.* **12**, (2000), p. 693.
7. P. Pieranski, *Contemp. Phys.* **24**, (1983), p. 25.
8. E. Trizac, L. Bocquet, R. Agra, J.-J Weis, M. J. Aubouy, *Phys. C* **14**, (2002), pp. 9339-9352.
9. S. V. Savenko, M. Dijkstra, *Phys. Rev. E* **70**, (2004), pp. 051401-7.
10. J. F. Marko, *Phys. Rev. A* **39**, (1989), pp. 2050-2062.
11. T. Schilling, S. Pronk, B. Mulder, D. Frenkel, Phys. Rev. E **71,** (2005), p. 036138.
12. K. W. Wojciechowski, *Phys. Rev. B* **46**, (1992), pp. 26–39.
13. C. Vega, E. P. A. Paras, P. A. Monson, *J. Chem. Phys.* **96**, (1992), pp. 9060–9072.
14. M. Marechal, M. Dijkstra, *Phys. Rev. E* **77**, (2008), pp. 061405-061414.
15. A. C. Branka, K. W. Wojciechowski, *Phys. Rev. Lett.* **50**, (1983), 846–849.
16. P. Bolhuis, D. Frenkel, *J. Chem. Phys.* **106**, (1997), pp. 666–687.

17. N. D. Denkov, O. D. Velev, P. A. Kralchevsky, I. B. Ivanov, H. Yoshimura, K. Nagayama, *Langmuir* **8**, (1992), pp. 3183-3190.

18. B. J. Alder, T. E. J. Wainwright, *Chem. Phys.* **27**, (1957), pp. 1208-1209.

19. B. Pansu, P. Pieranski, L. Strzelecki, *J. Phys. Paris* **44**, (1983), pp. 531-536.

20. B. Pansu, P. Pieranski, *J. Phys. Paris* **45**, (1984), 331-339.

21. P. N. Pusey, W. Van Megen, *Nature* **320**, (1986), pp. 340-342.

22. C. A. Murray, D. H. Van Winkle, *Phys. Rev. Lett.* **58**, (1987), pp. 1200-1203.

23. P. Jiang, J. F. Bertone, K. S. Hwang, V. L. Colvin, *Chem. Mater.* **11**, (1999), pp. 2132-2140.

24. M. Schmidt, H. Lowen, *Phys. Rev. Lett.* **76**, (1996), pp. 4552-4555.

25. R. Zangi, S. A. Rice, *Phys. Rev. E* **61**, (2000), 660-670.

26. C. D. Dushkin, G. S. Lazarov, S. N. Kotsev, H. Yoshimura, K. Nagayama, *Colloid. Polym. Sci.* **277**, (1999), pp. 914-930.

27. B. G. Prevo, O. D. Velev, *Langmuir* **20**, (2004)**,** pp. 2099-2107.

28. J. A. Lee, L. Meng, D. J. Norris, L. E. Scriven, M. Tsapatsis, *Langmuir*, **22**, (2006). pp. 5217-5219.

29. I. D. Hosein, C. M. Liddell, *Langmuir* **23**, (2007), pp. 8810-8814.

30. I. D. Hosein, C. M. Liddell, *Langmuir* **23**, (2007), pp. 10479–10485.

31. I. D. Hosein, B. S. John, S. H. Lee, F. A. Escobedo, C. M. Liddell, *J. Mater. Chem.* **19**, (2009), pp. 344 – 349.

32. E. Adachi, A. S. Dimitrov, K. Nagayama, *Langmuir* **11**, (1995), pp. 1057-1060.

33. M. Abkarian, J. Nunes, H. A. Stone, *J. Am. Chem. Soc.* **126**, (2004), pp. 5978-5979.

CHAPTER 6

CONVECTIVE ASSEMBLY OF THREE-DIMENSIONAL DIMER AND SPHEROCYLINDER BASED COLLOIDAL CRYSTALS

Abstract

Dumbbell and spherocylinder shaped colloids were convectively assembled from aqueous particle suspensions under ambient conditions into three-dimensional multilayer colloidal structures. Surface and cross-sectional analysis confirmed that highly fused particles produced rotator phases, while less fused particles assembled into crystalline phases. The particles were oriented parallel to the substrate plane. Fast fourier transform analysis and back-reflection laser diffraction patterns indicated the stacked layers had oblique symmetry.

Introduction

Self-assembly based fabrication provides advantages in the rapid, cost-effective and energy efficient production of materials with structures and architectures inaccessible with conventional fabrication schemes.[3] This method is particularly attractive for assembling mesosized (~100nm-1μm) particles, which are too small for mechanical manipulation but too large to harness molecular interactions. This size regime is also the signature scale for structured materials and devices with advanced optical, magnetic and biological properties.[1-7]

Currently, spherical particles are used to produce self-assembled structures with mesoscale features. However, theoretical and experiment studies show that structural diversity of spherical particle systems is limited to close packing of high lattice symmetry arrangements,[8] such as hexagonal close-packed (HCP), cubic

close-packed (CCP) and random hexagonal close-packed (RHCP) crystals. Achieving different structures has been proposed by using more complex strategies such as inducing anisotropic particle-particle interactions via particle surface modification,[9-11] applying external fields on the particle system during assembly,[12-15] assembling binary colloidal systems,[16] and employing more advanced assembly techniques.[17-19]

Particles with shape anisotropy show a rich diversity of phases,[20-23] that may allow for materials with high structural complexity and improved properties. For example, photonic crystals fabricated from non-spherical particles lift symmetry induced denegeracies in the band structure, allowing wider and stable bandgaps to open between lower lying photonic bands at lower refractive index contrasts.[24, 25] Moreover, Monte Carlo simulations predict that non-spherical particle systems lead to different particle arrangements with reduced lattice symmetries. The simulated phases form as a result of a step-wise increase in the system density, after allowing for equilibration in each step.[26] At increased system densities, maximization of the free volume entropy is favored over orientational entropy, and leads first to structures with translational order but complete orientational freedom of the particle directors (i.e. known as a plastic crystal), and finally to both translational and orientational ordered structures. In spherocylinder and dumbbell colloids the center to center distance and sphere diameter ratio (L/D) also determine the final structure. For example, if $L/D < 0.37$ both rotator and crystalline phase are found, while above this value only crystalline phases are observed.[27] The rotator phase or the plastic crystal consists of randomly oriented particles with their center of mass approximately positioned on a RHCP lattice. The crystalline phases of spherocylinder and dumbbell shapes are orthorhombic and base-centered monoclinic, respectively.

To date, experimental reports of ordered non-spherical particle self-assembly

at the mesoscale have been limited. The 3D formation of both rotator and crystalline phases from dumbbell shapeD particles was examined in suspensions using ultra-small x-ray scattering.[28] Crystalline phases have also been produced in dry form.[28,29] Additionally, large-scale 2D arrays of dumbbells were reported, in which particle orientations could be adjusted via tuning the assembly parameters (i.e. volume fractions of solid).[30]

In this study, spherocylinder and dumbbell shaped colloids are assembled into colloidal thin films on glass and silicon substrates at a crystallization rate of approximately 0.5mm per day using a controlled drying method. Rotator and crystalline structures are produced depending on the particle shape aspect ratio, or L/D. The crystalline structures are characterized by SEM, FIB cross-section imaging and UV laser diffraction. The experimental data confirms that phases predicted by Monte Carlo simulations can be accessed using this technique.

Experiment

Particles

Asymmetric dimers were prepared via a multi-step seeded emulsion polymerization technique. Monodisperse polystyrene (PS) latex (~ 250 nm) crosslinked with 3% divinylbenzene (DVB, 55%, Aldrich) were first synthesized as described previously,[28] and surface treated with either vinyl acetate (VA, Aldrich) or acrylic acid (AA, Aldrich) at a density of 3.56×10^{-21} g/nm^2. The dispersion was dialyzed for at least 24 hours against deionized water (Millipore, 18.2 MΩ-cm) and adjusted to a pH of ~6.2 prior to subsequent use. To produce dimers, seed particles (0.5 g) were swelled with 1.5 to 2.5 mL of monomer (consisting of 97% PS and 3% DVB), 5 mg hydroquinone (Aldrich), 8-12 mL of a 1% poly(vinyl alcohol) (PVA, 87-89% hydrolyzed, Aldrich) solution, toluene (Aldrich), and 37.5-75.0 mg of the 2,2'-

azobis(2,4-dimethyl valeronitrile) (V-65, Wako Chemicals Inc.) initiator overnight.[31] Polymerization was carried out at 70 or 80 ^{o}C in a shaker bath operating at 120rpm for 24 hours. Particle solutions were washed by repeated centrifugation and re-dispersal into deionized water. For samples with added toluene, washes were done in methanol before transitioning to pure deionized water. Table 6.1 summarizes the synthesis parameters for each particle shape. The spherocylinder shaped particles were prepared by a previously reported procedure.[29]

Assembly

Particle suspensions were prepared with 18.2 MΩ ultrapure water (Barnstead, NanoPure Diamond) and were approximately 1% volume fraction particles. Three milliliters of each particle suspension was placed in a separate vial and sonicated for one minute to ensure complete dispersion of the particles in the solvent. The vial was cleaned with water and ethanol, and dried under a flow of nitrogen gas prior to use. Silicon and glass substrates were soaked in freshly prepared piranha solution (18M H_2SO_4 and 30 wt% H_2O_2 solution in a 2:1 v/v mixture) for 30 minutes, rinsed several times with water, and dried under nitrogen. Glass substrates were exposed to oxygen

Table 6.1. Particle synthesis parameters.

Sample Name	**Coating type**	**Monomer (mL)**	**Toluene (mL)**	**1% PVA (mL)**	**V-65 (mg)**	**Temp (^{o}C)**
nanoSDPS 5:1 AA	Acrylic acid	1.5	0.0	8	37.5	70
nanoSDPS 7:1 AA	Acrylic acid	2.5	0.0	12	75.0	70
nanoSDPS 5:1 VA	Vinyl acetate	1.5	0.0	8	37.5	70
nanoSDPS 7:1 VA	Vinyl acetate	2.5	0.0	12	75.0	70
nanoSDPS 5:1 AA Toluene	Acrylic acid	1.5	0.5	8	37.5	80
nanoSDPS 5:1 AA no Toluene	Acrylic acid	1.5	0.0	8	37.5	80

plasma for 10 minutes to increase their hydrophilicity before use.

The substrates were dipped vertically into the particle suspensions and held in place by two binder clips. The setups were left on a sturdy table and the solvent allowed to completely evaporate at ambient conditions (T ≈ 23°). For the spherocylinder shape particle, dispersion in the solvent was maintained via a magnetic stirring (~30rpm) on a slow speed stirrer (Corning, Product# SS4I).

Imaging

The scanning electron microscopy (SEM) images of all films were obtained with a Zeiss ultra high resolution field emission scanning electron microscope. The films were sputtered with gold before imaging.

Silica Infiltration

Colloidal films were baked in an isotemp oven at 85°C for 2 hours to increase their mechanical stability and substrate adhesion. A silica sol solution was prepared consisting of 7mL ethanol, 1mL tetraethylorthosilicate (TEOS), 0.2mL H_2O, 25uL HCl (acid catalyst). The films were dipped into the sol solution using a computer controlled dip coating system (Nima DC Mono 75) at an immersion and withdraw speed of 1 mm/min. The samples were fumed with ammonia vapor in a sealed jar for 30 minutes immediately after dip coating. To facilitate the slow hydrolysis and condensation of the silica, the films were then suspended over the surface of 1mL of water in a glass vial and placed in oven at 65°C until the water completely evaporated. The polymer cores were removed via oxygen plasma etching for 10 min.

Focused Ion Beam Milling

Ion milled cross sections and images were obtained using a Strata 400 STEM

DualBeam system. Samples were milled using a liquid Gallium source with an accelerating voltage of 30kV and beam current between 93-280pA.

Laser Diffraction

Selected area laser diffraction, in back reflection mode, was performed using a Helium-Cadmium 325nm wavelength laser light. The laser beam diameter of 2mm was expanded to approximately 2cm using a beam expander before being transmitted through the optics setup. The beam was passed through an adjustable iris (Thorlabs, Part # IDM/25) in order to control the intensity of light impinging on the sample. The laser beam was then passed through a bi-convex UV fused silica lens (Thorlabs, Part # LB4003, f = 30cm) to focus it onto the sample. The sample was placed on a stage consisting of a XYZ translation stage (Thorlabs, Part # PT3) mounted onto a rotation platform (Thorlabs, Part # PR01), which allowed different regions of the film to be analyzed at different angles of incidence.

Results & Discussion

Figure 6.1 shows SEM images of the as synthesized non-spherical dimers. The shape of the asymmetric dimers is described by the normalized bond length parameter $L^* = L/2r_l$ and the lobe symmetry $S = r_s / r_l$, where L is the center to center distance between the lobes, and r_l (r_s) is the radius of the larger (smaller) lobe, determined from SEM images of the particles. The spherocylinder is also characterized based on its L* value, where L represents the length of the cylindrical body and r the radius of the hemispherical caps on both ends of the cylinder. Table 6.2 summarizes the particle size and shape parameters.

Table 6.2. Particle shape characteristics.

Dimers

Sample	Lobe 1 Dia. (nm)	Lobe 2 Dia. (nm)	Bond Length (nm)	Asymmetry	L/D
1	315	378	84	0.17	0.22
2	316	440	124	0.28	0.28
3	318	384	118	0.17	0.31
4	243	279	96	0.13	0.34
5	325	366	170	0.11	0.47
6	254	315	149	0.19	0.47
7	315	400	225	0.21	0.56

Spherocylinder

Sample	Lobe 1 (nm)	Lobe 2 (nm)	Bond Length	Asymmetry	L/D
8	1140	1140	317	0	0.28

The spherocylinders assembled into three-dimensional multilayer arrays with long-range positional order (Figure 6.2a). The particle long axes were oriented parallel to the layers and had a narrow distribution in the director orientations. The Fast Fourier Transform (FFT) of the film surface produced a spot pattern having oblique symmetry, indicating that the particles were positioned on an oblique lattice in each layer. The 3D lattice could be inferred to be monoclinic, based on the stacking of these oblique layers (Figure 6.2b).[32] Although simulations predict this particle shape to produce rotator phases based on its low L* value (0.28), the additional effects such as the solvent flow and templating from the deposited film likely facilitate the arrangement of particles onto an ordered lattice with orientational order.

Short bond length dumbbells with L^* less than 0.37 also produced multilayer arrays with large scale positional order (Figure 6.3a). The particle orientations were restricted to the plane of each layer without any orientational order. This observed

structure (with positional ordered and orientational disordered) resembles the rotator phase, but is not completely equivalent to the generalized rotator structure, in that particle orientations are not completely random. This distinction can be visualized in the FFT of the surface which produced a spot pattern having oblique symmetry. Here, the obliqueness confirms the orientation restriction on the particles in the layered planes. Perfect rotational freedom in a layer should produce a 6-fold symmetry pattern having lattice spacing equal to the rotating diameter of the particle (i.e., the total particle length along the major axis). This structure is clearly more densely packed, at the cost of orientational freedom, which results in the lattice being anisotropically compressed, with respect to the ideal hexagonal rotator structure.

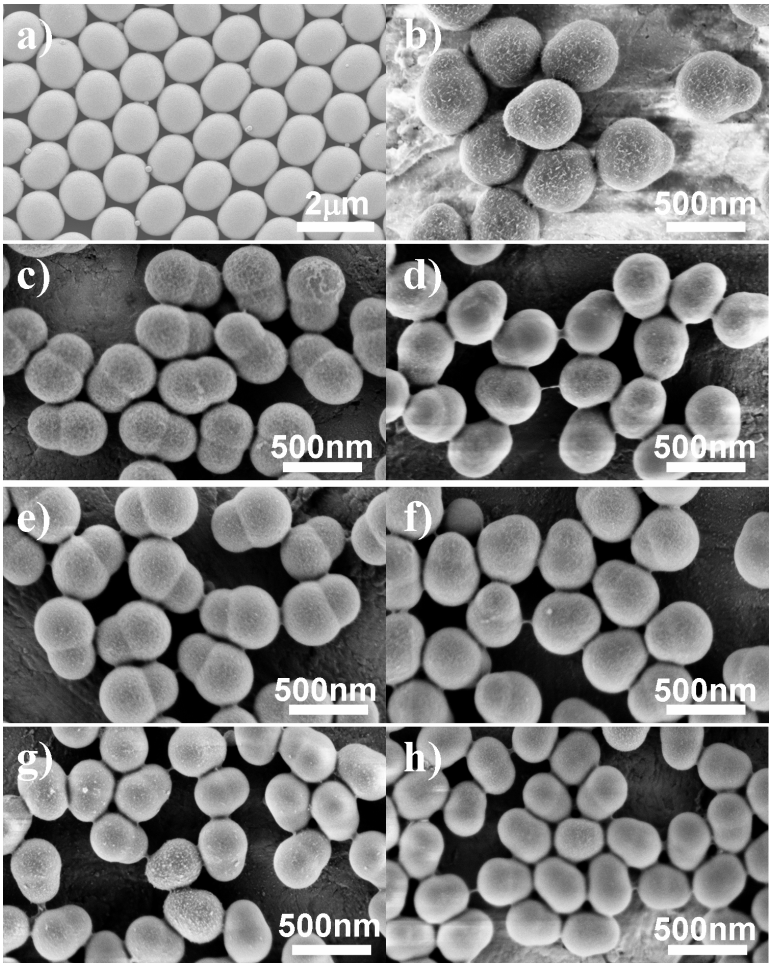

Figure 6.1. SEM images of non-spherical particles, A) Spherocylinder and B)-H) dumbbell shaped particles with a variety of symmetries and normalized bond lengths.

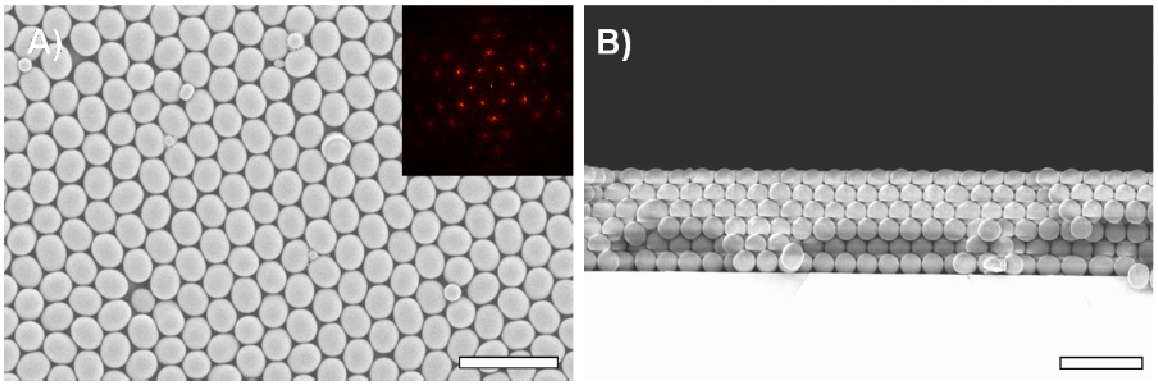

Figure 6.2. SEM images of spherocylinder based assembly. A) Surface of the film. Inset shows the FFT of the imaged. B) Film cross-section. Scale bars represent a) 4μm and b) 5μm.

Close examination of the particle orientations revealed that particle directors were restricted to the in-plane stacked layers. Particle morphologies with a sufficiently low L* and S, so as to resemble a sphere with a protruding "nub", can be stabilized in a "degenerate" type state,[32] where the large lobes pack on a close-packed RHCP lattice and protrusions fit randomly into the interstitial spaces. This phase is stable for particle shapes with $S \leq -1 + 2\sqrt{1-\sqrt{3}L^* + L^{*2}}$,[32] a condition which is not satisfied by any samples examined in this study.

Dumbbells with L* greater than 0.37 produced crystalline films having both long range positional and orientational order (Figure 6.3b). The FFT displays sharp peaks corresponding to an oblique symmetry and the three-dimensional structure consists of stacked 2D oblique crystal layers. In general, this stacking arrangement either produces base-centered monoclinic, triniclinic, or base-centered orthorhombic crystal structures.[33] The oblique lattice has a centered rectangle non-primitive unit cell with lattice vectors t_1 and t_2 along the sides of the cell, which are stacked into either of the three crystal structures depending on the third lattice vector t_3.[34] Local regions of rectangular packing were also observed in the surface images for both low and high L* values (Figure 6.3c and d), with orientational order exhibited in the structure with L* > 0.37. The corresponding FFT spot patterns of the surface images

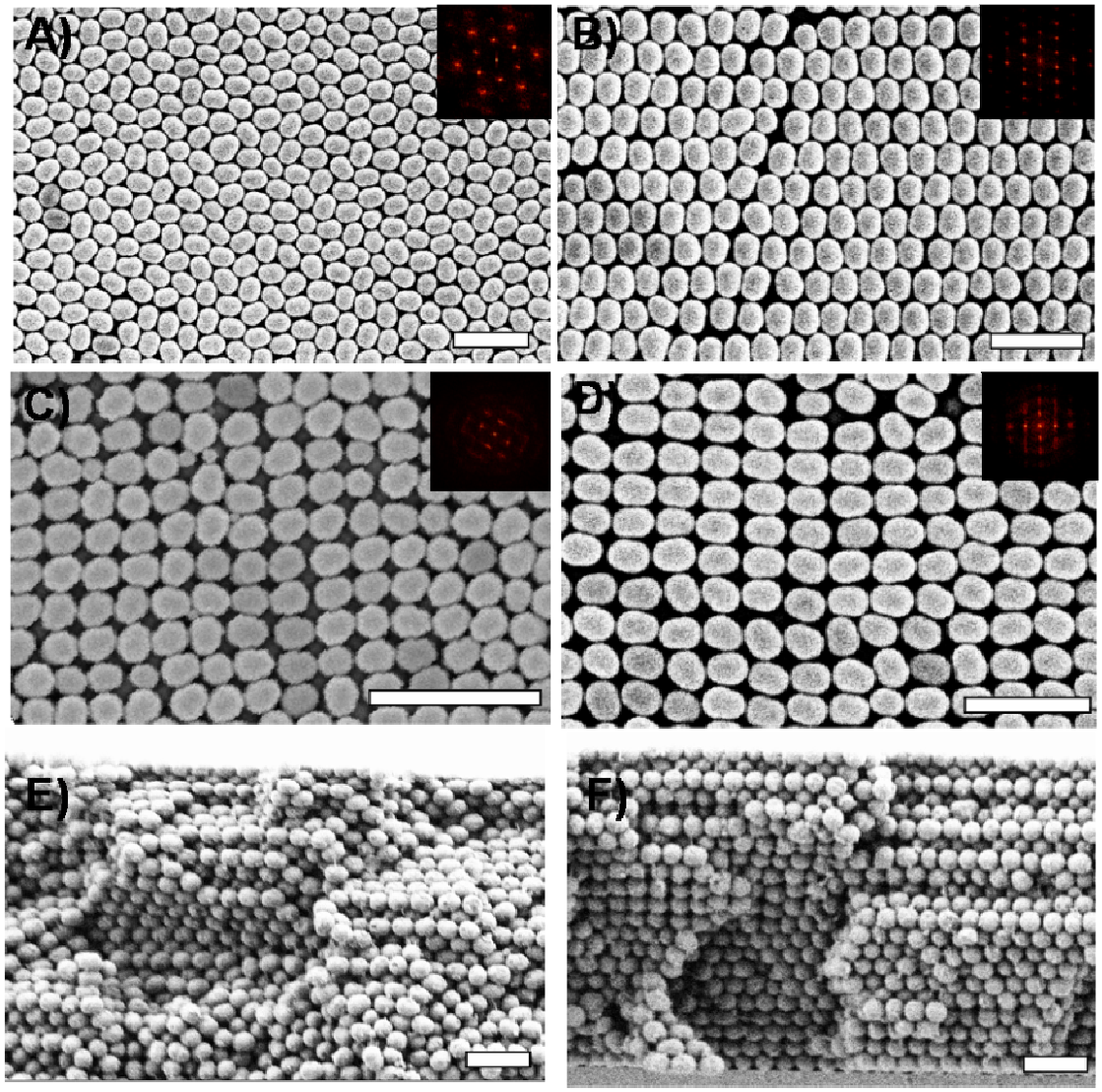

Figure 6.3. SEM images of dumbbell based assemblies. A) Surface image of a rotator structure. B) Surface image of the crystalline structure with centered rectangle unit cell. C) Surface image of positional order with rectangular packing for $L^* < 0.37$. D) Surface image of positional and orientation order on a rectangular lattice for $L^* > 0.37$ Insets show FFT patterns of the surface images. E) and F) are film cross-sections for rotator and crystal, respectively. Scale bars represent A) 1μ, B) 2μm C) 4 and 1μm for D) E) and F).

confirmed the real-space rectangular symmetry of ordering.

To closely investigate the 3D ordering, inverted silica replicas of the crystals were used to obtain carefully cut cross-sections by focused ion beam (FIB) milling. The cross-sections revealed the multilayer structure in both dimer and spherocylinder

based structures (Figure 6.4), and confirmed that orientations of the particle directors were parallel to the substrate. The orientational order in the dimer based crystals was sufficiently defined that cuts could be made both parallel (type A) and perpendicular (type B) to the particle orientation. Type B cuts made perpendicular to the particle long axis produced pores with a circular cross-sectional shape. In contrast, type A cuts made parallel to the long axis showed pores having the dimer shape. The cut pores along the spherocylinder cross-section had similar shape and size, indicating the particles were cut in the same direction relative to the major axis.

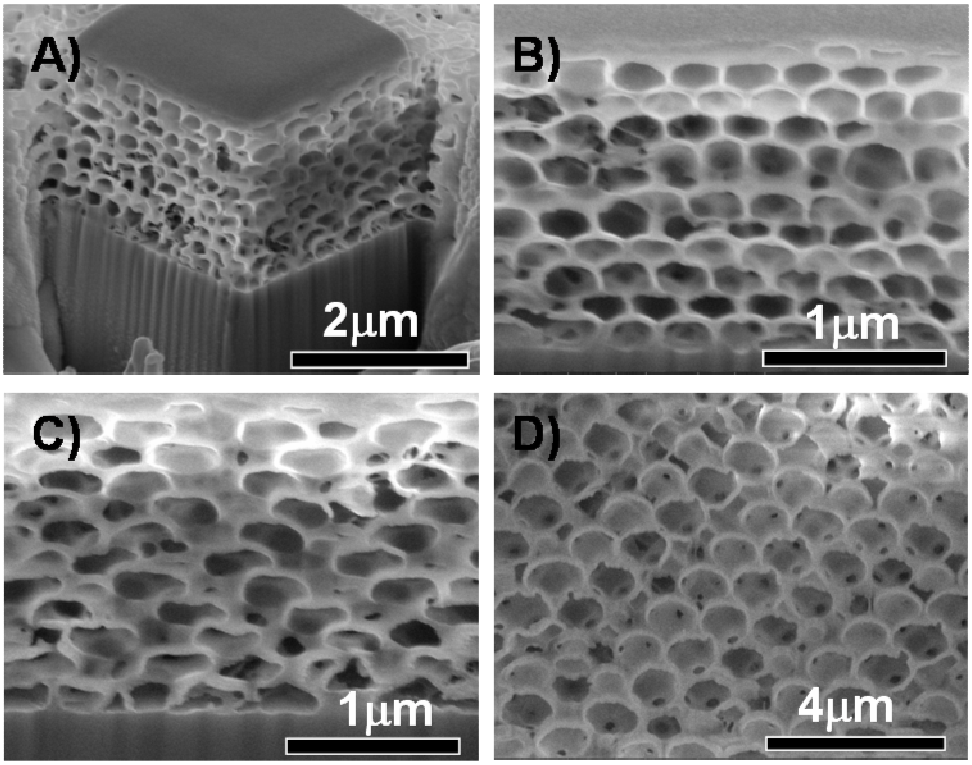

Figure 6.4. FIB milled cross-sections of the dimer and spherocylinder crystalline phases inverted in silica. A) Perspective image of the dimer based crystal slice along the particle long axis and perpendicular to it. B) Close up image of the dimer cross-section perpendicular to the particle long axis. C) Close up image of the dimer cross-section parallel to the particle long axis. D) Cross-section of the spherocylinder based crystal, cut approximately along the particle long axes.

The optical laser diffraction images for spherocylinder, dumbbell rotator and

dumbbell crystal are shown in Figure 6.5. All three diffraction patterns showed sharp spots that reproduced the symmetry of the crystal structure observed from surface SEMs and FFT analysis. The spherocylinder pattern contained more spots due to its larger lattice constant relative to the laser wavelength, allowing for more high order lattice planes to satisfy the diffraction condition. The dumbbell based crystalline films showed only two spots on opposite sides of the zeroth order reflected beam. This feature confirmed 2-fold rotational symmetry of the lattice, and further indicated that only certain reflection conditions were permitted. Single crystalline diffraction patterns were obtained from spot sizes of approximately 30μm, indicating that single crystal domains extended to this length scale. The strong coherent scattering evidenced by the sharp spot pattern was also an indication of the high quality crystals produced by the particles.

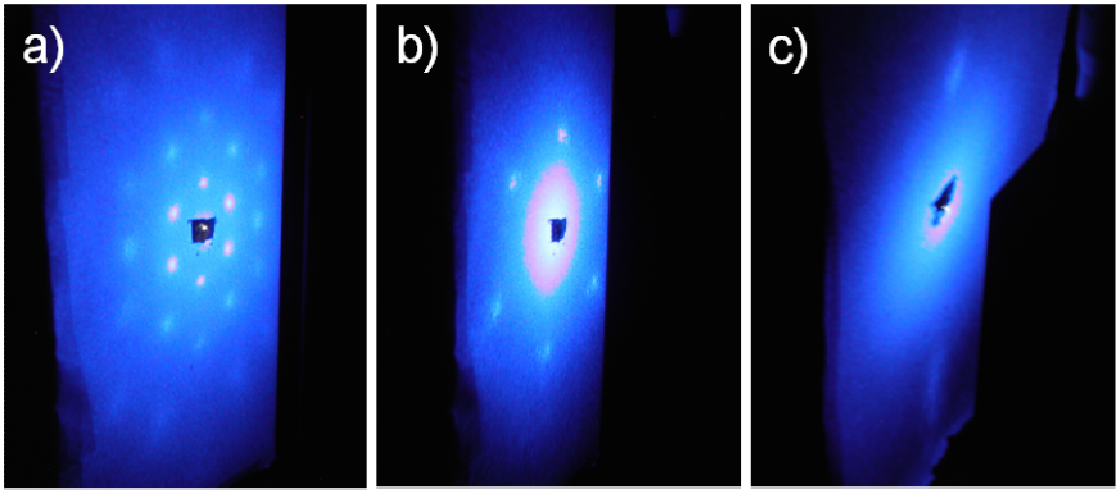

Figure 6.5. Optical laser diffraction patterns for A) Spherocylinder, B) Rotator and C) Crystal.

Table 6.3 summarizes the phases observed for each particle shape and its corresponding predicted structure, in order of increasing L^*. Normalized bond lengths producing the rotator and crystalline phases were demarcated by an L/D value of ~0.34, comparable to the computational value of ~0.37. Whereas convective assembly

is a dynamic (i.e. non-equilibrium) process, both the simulated particle system and the physical arrangement of particles at the meniscus tend towards a most densely packed state, which is one possible explanation for the agreement between the predicted and experimental structures.

Table 6.3. Summary of assembly results.

Dimers

Sample	L/D	Experiment	Theory
1	0.22	Rotator	Rotator
2	0.28	Rotator	Rotator
3	0.31	Rotator	Rotator
4	0.34	Rotator, Crystal	Rotator
5	0.47	Crystal	Crystal
6	0.47	Crystal	Crystal
7	0.56	Crystal	Crystal

Spherocylinder

Sample	L/D	Experiment Result	Theory
8	0.28	Rotator, Crystal	Rotator, Crystal

Conclusion

Multilayer colloidal structures were convectively assembled from dimer and spherocylinder shaped colloids. The dimers produced rotator and for L* values less than 0.34, and crystalline structures above 0.37. The spherocylinder (L*=0.28) assembled into a crystalline phase. Each particle layer had oblique symmetry as shown in FFT and laser diffraction analysis. This works holds promise in applying the convective assembly method to assemble a host of colloidal shapes into technologically-relevant structures.

REFERENCES

1. M. Boncheva, G. M. Whitesides, *MRS Bull.* **2005**, *30*, 736-742.
2. Birner, A.; Wehrspohn, R. B.; Gosele, U. M.; Busch, K. *Adv. Mater.* **2001**, *13*, 377-388.
3. Rybczynski, J.; Banerjee, D.; Kosiorek, A.; Giersig, M.; Ren, Z. F. *Nano Lett.* **2004**, *4*, 2037-2040.
4. Goncharov, A.; Zhukov, A. A.; Bartlett, P. N.; Ghanem, M. A.; Boardman, R.; Fangohr, H.; de Groot, P. A. J. *J. Magn. Magn. Mater.* **2005**, *286*, 1-4.
5. Chiu, D. T.; Wilson, C. F.; Ryttsen, F.; Stromberg, A.; Farre, C.; Karlsson, A.; Nordholm, S.; Gaggar, A.; Modi, B. P.; Moscho, A.; Garza-Lopez, R. A.; Orwar, O.; Zare, R. N. *Science* **1999**, *283*, 1892-1895.
6. Grosvenor, A. L.; Feltus, A.; Conover, R. C.; Daunert, S.; Anderson K. W. *Anal. Chem.* **2000**, *72*, 2590-2594.
7. Cooper, J. M. *Trends Biotechnol.* **1999**, *17*, 226-230.
8. Grzybowski, B. A.; Haag, R.; Bowden, N.; Whitesides, G. M. *Anal. Chem.* **1998**, *70*, 4645-4652.
9. Zhang, Z.; Glotzer S. C. *Nano Lett.* **2004**, *4*, 1407–1413.
10. Zhang, Z.; Keys, A. S.; Chen, T.; Glotzer, S. C. *Langmuir*, **2005**, *21* (25), 11547–11551
11. Gangwal, S.; Cayre, O. J.; Velev, O. D. *Langmuir* **2008**, *24*, 13312-13320.
12. Yethiraj, A; van Blaaderen, A. *Nature* **2003**, *421*, 513-517.
13. Hynninen, A.-P. Dijkstra, M. *Phys. Rev. Lett.* **2005**, *94*, 138303-138306.
14. Yethiraj, A.; Thijssen, J. H. J.; Wouterse, A.; van Blaaderen A. *Adv. Mater.* **2004**, *16*, 596-600.
15. Russel, W. B. *Nature*, **2003**, *421*, 490-491.

16. Sullivan, M.; Zhao, K.; Harrison, C.; Austin, R. H.; Megens, M.; Hollingsworth, A.; Russel, W. B.; Cheng, Z.; Mason, T.; Chaikin, P. M. *J. Phys.: Condens. Matter* **2003**, *15*, S11–S18

17. Leunissen, M. E.; Christova, C. G.; Hynninen, A.-P.; Royall, C. P.; Campbell, A. I.; Imhof, A.; Dijkstra, M.; van Roij, R.; van Blaaderen, A. *Nature* **2005**, *437*, 235-240.

18. Hynninen, A.-P.; Thijssen, J. H. J.; Vermolen, E. C. M.; Dijkstra, M.; van Blaaderen, A. *Nat. Mater.* **2007**, *6*, 202-205.

19. Jiang, P.; McFarland M. J. *J. Am. Chem. Soc.* **2004**, *126*, 13778–13786.

20. García-Santamaría , F.; Miyazaki , H.T.; Urquía , A.; Ibisate M., ; Belmonte, M.; Shinya , N.; Meseguer , F.; López C. *Adv. Mater.* **2002**, *14*, 1144 – 1147.

21. Glotzer, S. C. *Science* **2004**, *306*, 419-420.

22. van Blaaderen, A. *Nature* **2006**, *439*, 545-546.

23. Glotzer, S. C.; Solomon, M. J.; Kotov, N. A. *AIChE J.* **2004**, *50*, 2978-2985.

24. Yablonovitch, E.; Gmitter, T. J.; Leung, K. M. *Phys. Rev. Lett.* **1991**, *67*, 2295-2298.

25. Xia, Y.; Gates, B.; Li, Z.-Y. *Adv. Mater.* **2001**, *13*, 409-413.

26. Frenkel, D.; Smit, B. *Understanding Molecular Simulation. From Algorithms to Applications, 2nd ed.*; Academic Press: New York, 2002.

27. Vega, C.; Monson P. A. *J. Chem. Phys.* **1997**, *107*, 2696-2697.

28. Mock, E. B.; Zukoski, C. F. *Langmuir*, **2007**, *23*, 8760–8771.

29. Hosein, I. D.; Liddell, C. M. *J. Mater. Chem.* **2009**, *19*, 344–349.

30. Hosein, I. D.; Liddell, C. M. *Langmuir*, **2007**, *23*, 10479–10485.

31. Kim, J.-W.; Larsen, R. J.; Weitz, D.A. *J. Am. Chem. Soc.* **2006**, *128* (44), 14374-14377.

32. Gay, S. C.; Beale, P. D.; Rainwater, J. C. *Intl. J. Thermphys*. **1998**, *19*, 1535.

33. Hammond, C. The *Basics of Crystallography and Diffraction, 2nd Ed.* Oxford University: Oxford, 2001

34. Samuel M. Allen, Edwin L. Thomas, The Structure of Materials, Wiled, New York, 1999.

CHAPTER 7

PROBING DIMER SHAPE ANISOTROPY: A NONSPHERICAL COLLOIDAL APPROACH TO OMNIDIRECTONAL PHOTONIC BANDGAPS

Abstract

The photonic bandgaps of asymmetric dimer based FCC lattices are studied. Stable photonic bandgaps open for both direct and indirect dielectric structures, with a high dielectric of 12.25. Gaps were observed between the 2nd and 3rd, 5th and 6th, and 8th and 9th bands, as well as the presence of double bandgap band structures. By tuning the dimer basis shape, degeneracies observed in the band structure of the diamond and zinc blende cases were broken.

Introduction

In recent years monodisperse anisotropic colloidal building blocks have been prepared in high yield with the promise for photonic applications. Features such as annular control of the surface inhomogeneity of patchy particles,[1] bi-functional compartments of Janus particles,[2] and/or the geometry of non-spherical colloids [42-77] have been envisioned to promote the efficient self-assembly of complex patterned structures in the submicron to ~micron feature size regime for light control. Computational studies have inspired this strategy referred to as 'symmetry reduction', since close-packed arrays of spheres are limited as templates for materials that support wide and stable photonic band gaps. The quintessential example is dielectric spheres and air spheres arranged in a diamond lattice (with a two sphere basis) where the degeneracy at points of high symmetry in the Brillouin zone is lifted relative to the face-centered cubic structure, opening 2-3 bandgaps up to ~16% for a filling fraction

of 37% dielectric spheres and ~29% for a filling fraction of 81% air spheres at a refractive index contrast value (n_c) of 3.6 [6]. A 5-layer direct diamond structure was realized using a pick-and-place means (i.e., microrobotics) to build a binary body-centered cubic structure of silica and sacrificial polystyrene spheres, equivalent to two interpenetrating diamond lattices. Though the requirement of a minimum n_c of 2.0 to obtain a bandgap for spheres 'just touching' was not met,[6] the fabrication alone of a diamond structure from colloidal particles was ground breaking and has not since been achieved through other approaches.

Diamond-like or diamond-inspired structures are being pursued that seek to capitalize on the advantage of colloids for low cost self-assembly rather than direct site-by-site manipulation. Similar photonic properties were found from the dispersion relations for the 'tetrastack' structure based on tetrahedral 4-lobed colloidal clusters in a mechanically stable layered arrangement that mimics diamond connectivity, as the tetrahedra align along the <111> crystallographic direction. The model arrangement can also be regarded as a derivative of the pyrochlore lattice of corner-sharing tetrahedral.[7] 2-lobed motifs such as peanut-shaped particles of iron oxide have also been calculated to sustain 2-3 bandgaps in diamond-analog dimer structures starting at a relatively low n_c value of 2.4.[8] Zinc-blende type dielectric structures comprising two spheres of identical composition, but different radii as the basis on an FCC lattice have also been investigated for gap-forming properties.[9] Variation in the filling of the 'Zn' sublattice and the 'S' sublattice was done by decreasing one radius in the basis pair below the condition for contact and 2-3 bandgaps were found for f_{Zn}/f_S between 0.85 and 1.2. The asymmetric (or 'heteronuclear') dimers synthesized by seeded emulsion polymerization and phase separation [10-14] are ideal candidates for zinc blende-like colloidal assemblies where the building blocks remain tangent as their shape varies.

The present theoretical study systematically maps the photonic band structures for these dimer particles, modeled as partially interpenetrating sphere pairs in an FCC arrangement, as a function of the dimer morphology— specifically the degree of lobe fusion for the discrete dimers and the asymmetry between the lobes. Considering both direct and inverted cases, three bandgap locations 2-3, 5-6 and 8-9 were accessed by variation of the dimer shape parameters. We also find that a wide range of structures with heteronuclear dimer building blocks should be capable of producing bandgaps at low index contrast values down to 2.25.

Model and Calculation Methods

Several examples of the anisotropic polystyrene particle building blocks for dimer structures are illustrated in the scanning electron microscope images of Figure 1. By raising the temperature of monomer-swollen cross-linked polystyrene seed spheres modified with a hydrophilic surface (a grafted layer of polyacrylic acid),[12] we obtain the monomer phase-separation from the seed particle as a 'daughter' lobe rather than a corona. The dimer morphology is tunable from symmetric dimer lobes having equal radii to lobes with high degrees of asymmetry and from nearly completely overlapping lobes to mildly-fused lobes as the seed crosslinking density, monomer swelling ratio, amount of surface treatment, etc. is varied.[12,13] For the theoretical structures, the shape of the asymmetric dimers was described by the normalized bond length parameter $L^* = L/2r_l$ and the lobe symmetry $S = r_s / r_l$, where L is the center to center distance between the lobes, and r_l (r_s) is the radius of the larger (smaller) lobe. The model particle shape is spherical when $S \le 1 - 2L^*$ (i.e., the small lobe lies in the interior of the large lobe) and becomes two tangent spheres when $S = 2L^* - 1$. The region of dimer shape parameters L* and S satisfying the expression, $S \le -1 + 2\sqrt{1 - \sqrt{3}L^* + L^{*2}}$, consists of particles whose morphology resembles that of

a sphere with a protruding nub which will fit into the interstices of the large spherical lobes in a close-packed arrangement.[15] We consider only dimers with $S > -1 + 2\sqrt{1-\sqrt{3}L^* + L^{*2}}$ and $S > 2L^* - 1$ for optical band structure calculations to avoid the cases when the lobes no longer touch, are fused completely into one sphere, or have protrusions small enough to stabilize the interstice-based "degenerate" [15] crystal, where large lobes tile a triangular lattice and small lobes uniformly populate the pore spaces. Figure 7.1 shows the boundaries of the particle shape parameter space explored here for orientationally-ordered arrangements.

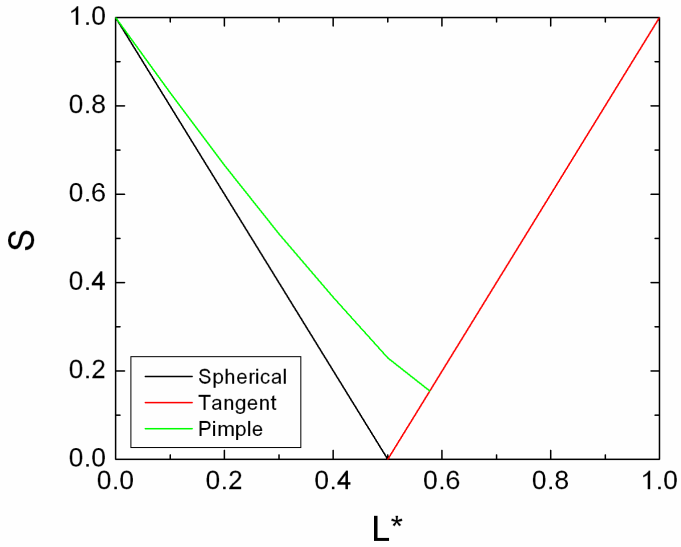

Figure 7.1. Particle parameter space.

Model particles were oriented in the $<11\bar{1}>$ direction with respect to the non-primitive FCC unit cell and were positioned with the center of the circular cross-section of the intersecting dimer lobes on FCC lattice sites (Figure 7.2a,b). The location p of this center point relative to the large lobe center of mass is given by: $p = \frac{L^2 - r_s^2 + r_l^2}{2L}$.

The large and small lobes were offset from the lattice site by p and p-L, respectively. At close packing, the lattice constant forms a triangle with a particle bond length L and

the center-to-center distance between the small lobe of one particle and the large lobe of a neighboring particle tangent to it. The angle between the latter two line segments is 109.5° and thus the lattice parameter a is determined by using the law of cosines, $|a| = \sqrt{L^2 + (r_1 + r_2)^2 - 2L(r_1 + r_2)\cos(109.5°)}$. In the case of two tangent lobes the symmetry group of the lattice point is that of the zinc blende crystal structure, $\bar{4}3m$ and is changed from the $m\bar{3}m$ symmetry of the FCC crystal structure.

Photonic band structures were numerically calculated based on the plane wave method in the full vectorial formulation [16], implemented using the MIT Photonic Bands Package [39]. The resolution and mesh size of the computation cell were 16 and 5, respectively. A convergence tolerance of 0.1% was used to determine the eigenfrequencies that propagate in each crystal structure. Band structures were computed for both the direct (i.e dielectric particles in an air matrix) and inverse cases with a dielectric contrast of 12.25, representing silicon and air composites.

The primitive lattice vectors for the FCC crystal structure were $a_1 = a\left(1/\sqrt{2},1/\sqrt{2},0\right)$, $a_2 = a\left(1/\sqrt{2},0,1/\sqrt{2}\right)$ and $a_3 = a\left(0,1/\sqrt{2},1/\sqrt{2}\right)$. The large lobe diameter was expressed in terms of the particle shape parameter $r_l = a/\sqrt{1 + S - 4L^*(1+S)\cos(109.5°) + 4L^{*2}}$. Defining $\gamma = \sqrt{1 + S - 4L^*(1+S)\cos(109.5°) + 4L^{*2}}$, the lobe radii values simplify to $r_l = a/\gamma$ and $r_s = Sr_l$. The offset of the large lobe from the lattice site in terms of a, γ, L* and S is $p = L^* a(S^2 + 1)/4\gamma$. The positions of the large and small lobe centers were respectively given by $p(a_1 + a_2 + a_3)/\sqrt{8}$ and $\left(p - 2L^* a/\gamma\right)(a_1 + a_2 + a_3)/\sqrt{8}$.

Results and Discussion

Complete photonic bandgaps were found in both direct and inverted structures. As the particle shape parameters were varied, the direct structures showed gaps between the

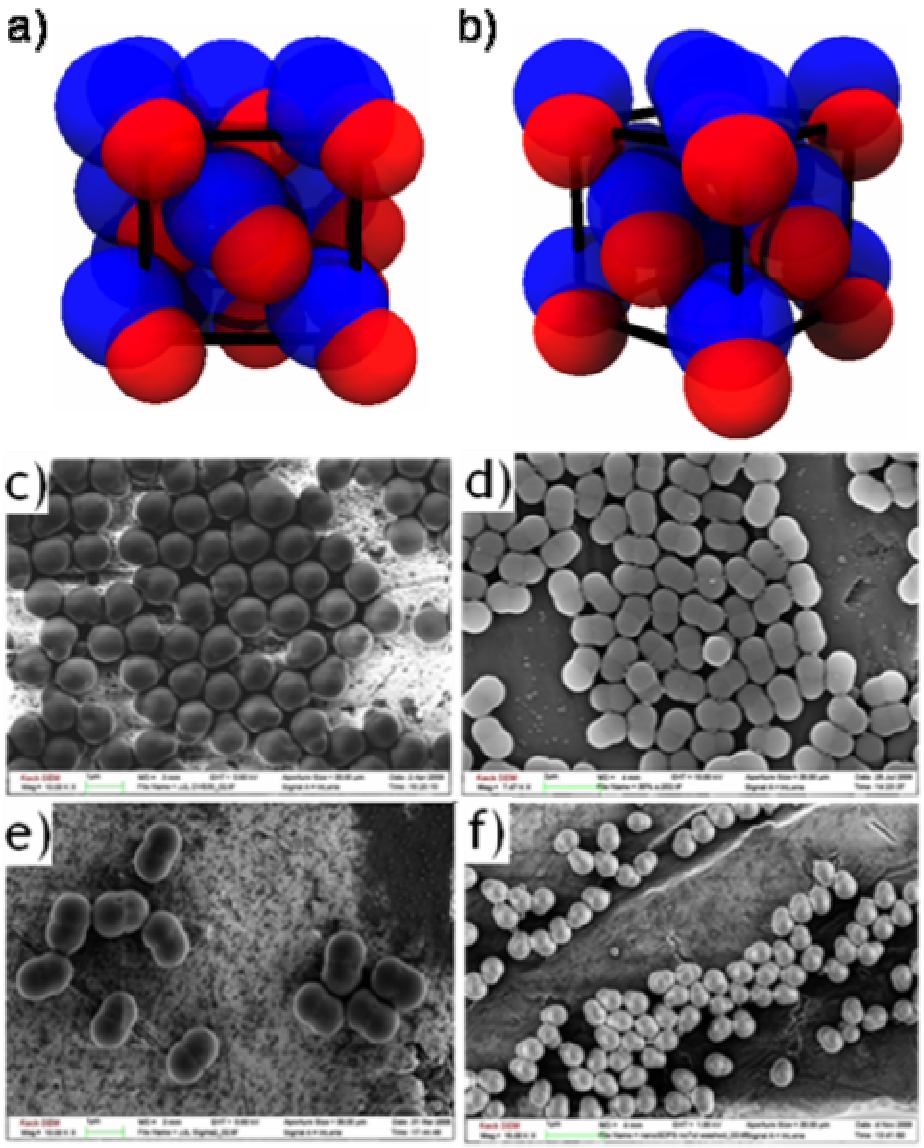

Figure 7.2. a-b) FCC dimer based structure, with S=0.8 and L*=0.5. Model particles are oriented in the $<11\bar{1}>$ direction. a) Unit cell viewed normal to (100) face. b) Perspective view of the unit cell. SEM images of colloids with parameters c) S=0.33, L*=0.51, d) _, e) S=0.78, L*=0.62, f) S=1, L*=0.67.

2nd and 3rd, 5th and 6th or 8th and 9th bands. Inverted structures showed gaps between the 2nd and 3rd or 8th and 9th bands. Regimes in particle parameter space also produced double gaps in the form of 2-3 and 5-6 or 2-3 and 8-9 bandgaps. Photonic band structures determined for dimer particle shapes that either maximized a band gap or

promoted structures with double gaps are shown in Figure 7.3. The largest gap between the 2nd and 3rd bands for the direct structure was that previously reported for the diamond structure (S=1 and L*=1). Figure 7.3a presents the band diagram for an additional local maximum within the particle parameter space explored for 2-3 gaps. The results are consistent with previous calculations which indicated that double gaps exist for structures of class $\bar{4}3m$ [18].

The twofold band degeneracy observed in diamond[6] and zinc blend[9] along the symmetry line from X to W is broken for the dimer basis. Figure 7.4 shows band structures along the X-W symmetry line for direct structures from symmetric-lobed particles (i.e. S=1) and with varying L*. Generally, decreasing the value of L* led to increased separation between band pairs that were degenerate originally. This narrows the size of the 2-3 gap with respect to the diamond case.

Figure 7.5 shows contour plots of the gap-to-midgap ratio versus particle shape for both direct and indirect structures for each bandgap location. The regions with zero gap represent either data points for particle shapes which yielded no gap or for particle shapes that were outside the region of interest for calculation (Figure 7.1). The plots show that a range of particle shapes yielded complete bandgaps between one of the three bandgap locations. The 2-3 gap for the inverted structure reached a value just short of that for the direct diamond. For the inverted structure, S=1 and L*=0 yields the gap width expected for the so-called inverted opal structure[19,20]. However, the gap was not maximed at this point, rather, a small asymmetry and elongation of the particle from the spherical shape (i.e. L*=0.03 and S=0.97) produced the greatest gap width. This latter point demonstrates small changes in the spherical shape can yield improvements to the bandgap properties.

Figure 7.3. Photonic band structures for FCC dimer-based a)-d) direct and e)-f) inverted structures. Particle shape parameters are a) L*=0.81, S=0.84, b) L*=0.79, S=0.58 c) L*=0.73, S=1 d) L*=0.78, S=0.64 e) L*=0.51, S=1, f) L*=0.03, S=0.97 and g) L*=0.18 S=0.84. Gap-to-midgap ratios are given in the plots. Band structures producing the greatest gap widths between the 2^{nd} and 3^{rd}, 5^{th} and 6^{th} bands, and 8^{th} and 9^{th} bands. c), d) and g) show double bandgaps.

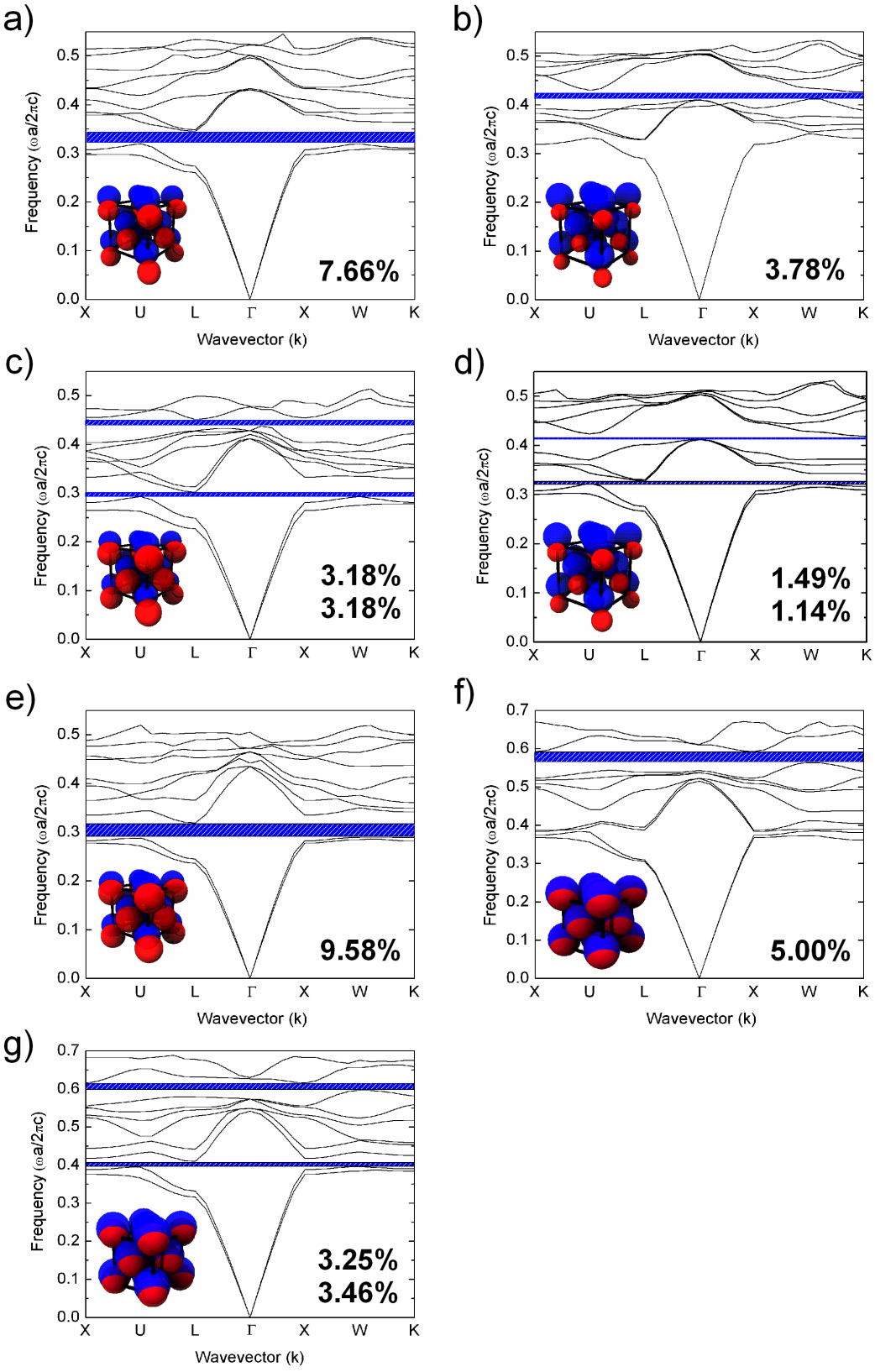
a)
b)
c)
d)
e)
f)
g)
Frequency (ωa/2πc)
Wavevector (k)
X U L Γ X W K
7.66%
3.78%
3.18%
3.18%
1.49%
1.14%
9.58%
5.00%
3.25%
3.46%

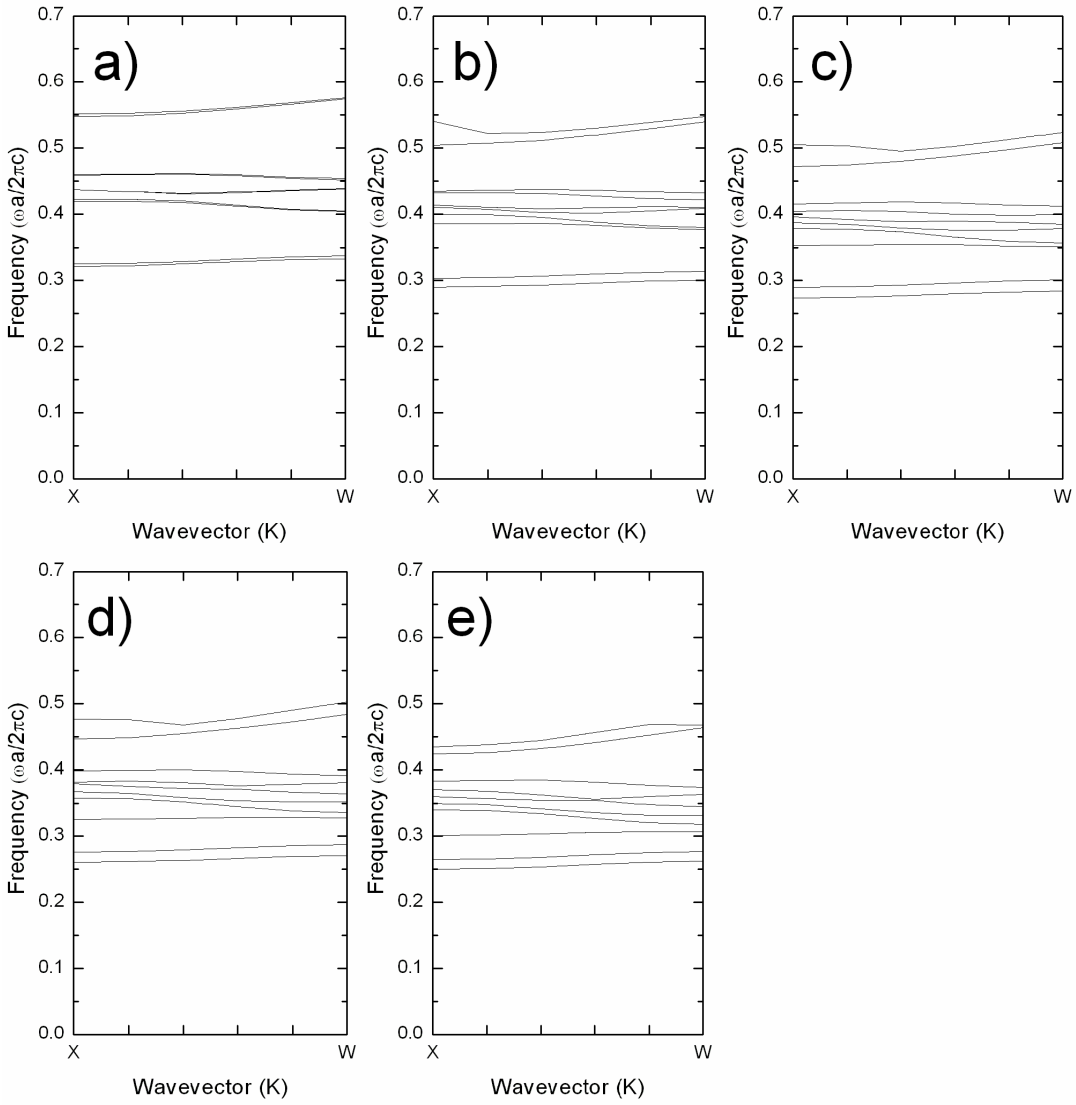

Figure 7.4. Band structures along the X-W symmetry line for direct structures of particles with S=1 and L* of a) 1.0 b) 0.9 c) 0.8 d) 0.7 e) 0.6.

Figure 7.6 shows contour plots of the threshold refractive index, n_c, versus particle shape. The threshold value is taken as the refractive index for creating a full photonic band gap with relative bandgap width of 1%. Table 7.1 summarizes these threshold values for direct and inverted structures for each bandgap location. The smallest n_c value found for the 2-3 gaps was 2.33 for direct structures and 2.25 for inverted structures.

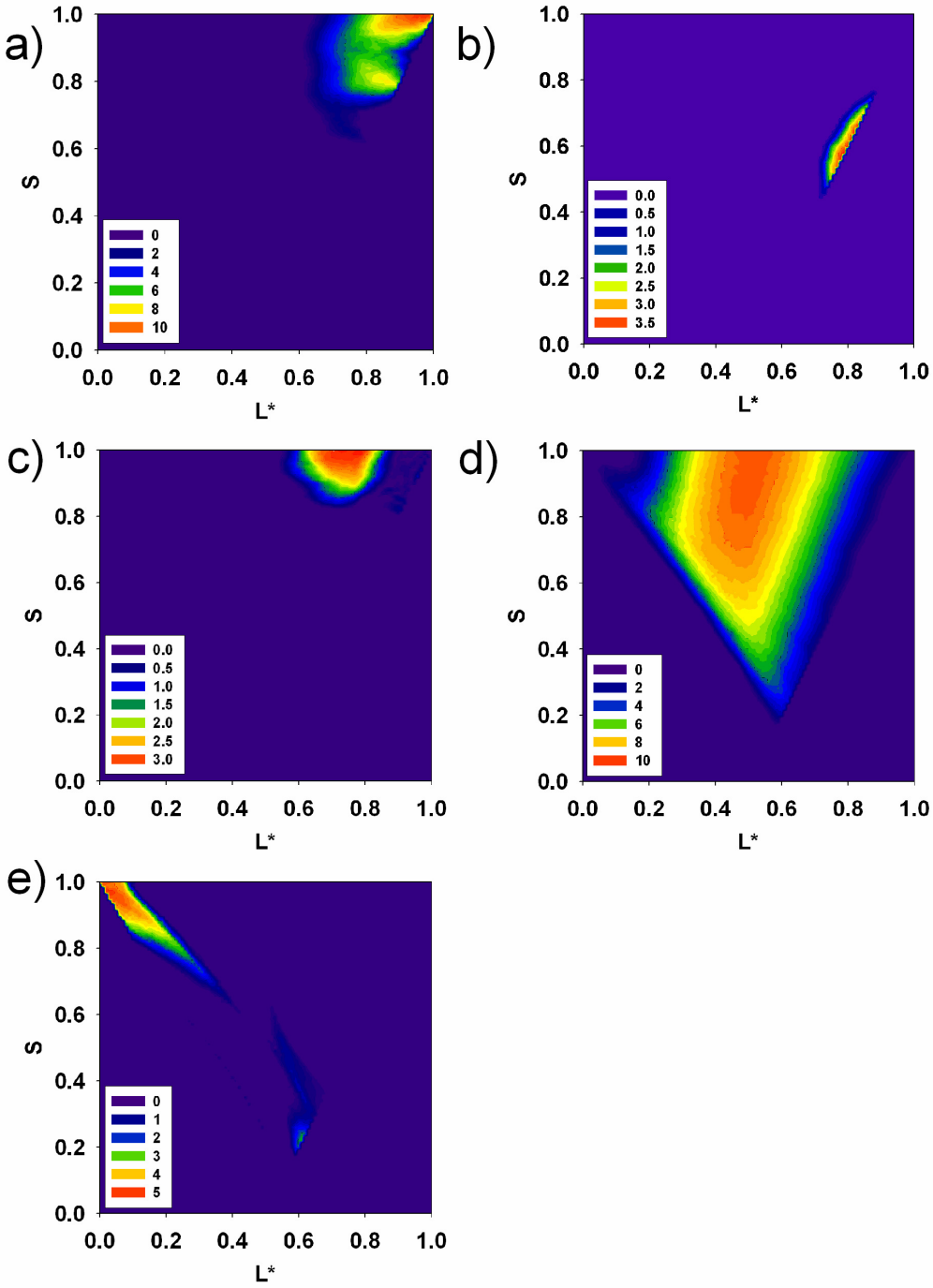

Figure 7.5. Contour plots of Gap-to-midgap ratio versus particle symmetry (S) and L* for a)-c) direct and d)-e) inverted structures, for gaps between the 2nd and 3rd bands: a) and d), 5th and 6th bands: b) and 8th and 9th bands: c) and e).

Table 7.1. Summary of photonic gap data.

	Gap Location	L*	S	Gap-to-Midgap Ratio (%)	nc
Direct	2nd-3rd	0.84	0.81	7.66	2.33
	5th-6th	0.79	0.58	3.78	3.29
	8th-9th	0.73	1.00	3.18	3.07
Inverted	2nd-3rd	0.51	1.00	9.58	2.25
	5th-6th	-	-	-	-
	8th-9th	0.03	0.97	5.00	3.07

Simeon et al [9] reported bandgap calculations for zinc blende structures of tangent spheres (i.e., along the S=2L*-1 line) and varying radius ratio, between 0.8 and 1. The existence of a 2-3 gap that was at its maximum for the diamond case and decreased with decreasing radius ratio was established. The present work is in agreement, and additionally covers a parameter space beyond the range used. Notably a 5-6 gap not previously determined as a function of radius ratio is found here.

Additionally, the photonic band structures were examined as a function of both filling fraction of high refractive index material and refractive index contrast for the particle shapes that maximized the gaps at close packing (Figure 7.7). The filling fraction was adjusted by varying the radius of the constituent lobes of the particle, while the lattice constant, *a*, remained fixed. In the direct case, this represents either sintering the particles or depositing thicker dielectric shells on the particle surfaces. Recoating macroporous inverted structures with additional high index material is one process that would produce pores with radii less than that for the close packing arrangements. In our optimization of inverted structures, bandgap values produced by structures made from high dielectric shells were shown to be smaller than those for structures made from complete filling of the particle interstitial space, thus only the latter was considered in the optimization. Experimentally, this means that volume templating

methods of inversion are favored over surface templating.[21]

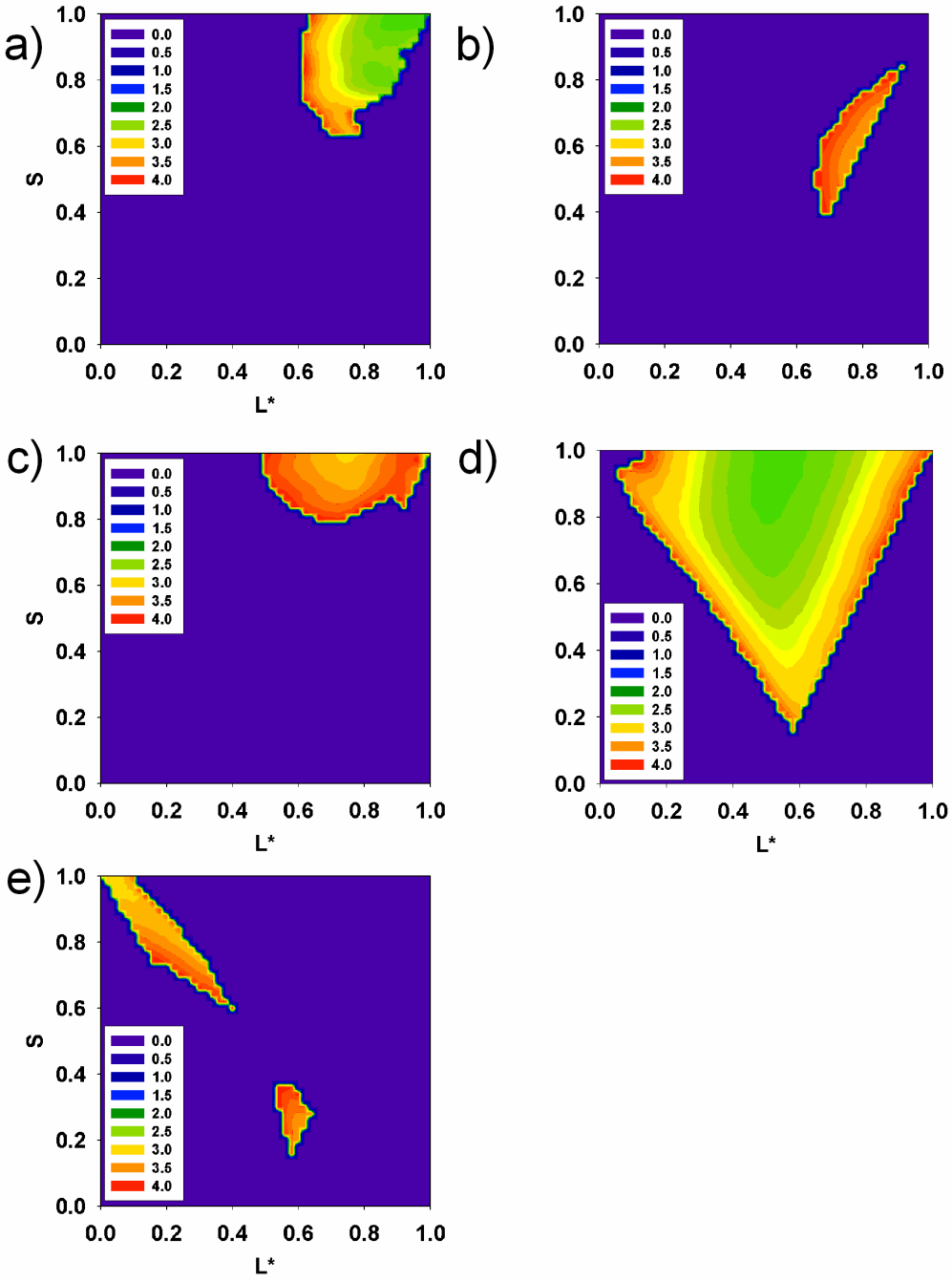

Figure 7.6. Contour plots of minimum refractive index n_c required to open a photonic bandgap versus particle symmetry (S) and L* for a)-c) direct and d)-e inverted structures, for gaps between the 2nd and 3rd bands: a) and d), 5th and 6th bands: b) and 8th and 9th bands: c) and e).

Figure 7.7 shows plots of the gap-to-midgap ratio (of the 2-3 gap) versus filling fraction and refractive index for both type of structures. For the direct case, a maximum gap of 8.93% was found at a filling fraction of 48.74%, while for the inverted case, the gap reached 21.95% at 22.23% filling. Increasing the index contrast for structures with filling fractions that maximized the gap (i.e. 48.74% and 22.23%, direct and inverted, respectively) showed that the maximum gap-to-midgap ratio saturated to values of approximately 13.2% and 32.1% for direct and inverted, respectively. The critical refractive index to open a gap for the direct and inverted case was approximately 2.17 and 2.03. These critical indices are lower than those for other proposed dielectric structures that could be fabricated from self-assembly of colloids such as the inverse skeleton structure (2.91) and face-centered cubic lattice of spherical shells connected by cylindrical tubes (2.30).[21, 23] Hillebrand et al. reported inverted diamond type structure of air spheres with connecting pores of tunable radius that could also yield large and stable gaps.[24] The structure could be produced by electrochemically etching prestructured silicon wafers. They also observed a decrease in gap width as the structure changed from the case of diamond. The latter critical index values computed in this study are sufficiently low to allow a diversity of refractive index materials to be used for the fabrication of dielectric structures. The filling ratio ranges for the existence of a complete bandgap were 35.74-69.70% and 6.24%-64.26% which are comparable to the ranges for the diamond case, indicating a comparable stability of the gap. It was found that when the particle shapes are optimized with respect to filling fraction gap widths and critical refractive index, values comparable to the diamond case could be found for a range of particle shapes. Table 7.2 summarizes the bandgap data, filling fraction and shape parameters in the optimization.

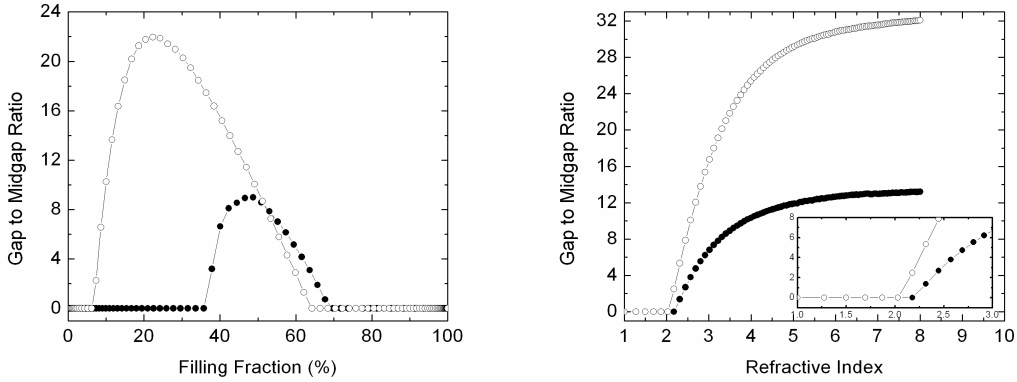

Figure 7.7. a) Gap to midgap ratio as a function of filling fraction for particle shape with L*=0.84 and S=0.81. b) Gap to midgap ratio as a function of refractive index contrast. Inset enlarges region of the plot near the critical refractive index.

Table 7.2. Summary of photonic gap optimization data.

	Gap Location	L*	S	Gap-to-Midgap Ratio (%)	f (%)	Nc*
Direct	2nd-3rd	0.84	0.81	8.98	48.74	2.03
	5th-6th	0.79	0.58	7.06	35.39	3.01
	8th-9th	0.73	1.00	8.39	18.69	2.69
Inverted	2nd-3rd	0.51	1.00	15.38	21.09	2.17
	5th-6th	-	-	-	-	-
	8th-9th	0.03	0.97	5.00	26.32	2.91

* n_c here represents the critical contrast to open a gap, i.e. a gap just greater than zero.

The ensemble of contour plots shown in Figure 7.5 showed that a large area of particle parameter space will yield dielectric structures with a complete bandgap. Optimization of the filling fraction of the dielectric structures, as well, resulted in even larger bandgaps than for close-packed structures and a wider particle parameter space for bandgaps. For example, along the line S=1 from L* = 0.5 to 1.0, for inverted structures, the gap size is shown to decrease with increasing L*, when the particles are close-packed. However upon optimization, the gap size monotically increased towards the maximum at the diamond case. The overall result being that the majority of particle shapes will produce a complete bandgap at one of the three locations

observed, either from a direct or inverted dielectric structure. Additionally, the larger spreads in complete bandgap regions in parameter space, will increase the likelihood of double bandgaps, as neighboring regions begin to overlap.

Conclusion

Photonic crystals structures with asymmetric dimer bases on an FCC lattice produced complete photonic bandgaps between the 2^{nd} and 3^{rd}, 5^{th} and 6^{th}, and 8^{th} and 9^{th}, for a range of particle shapes. Bandgaps were observed for both direct and indirect dielectric structures. The degeneracy in the bands along the X-W line can be broken by tuning the dimer shape The gaps are comparably stable to the diamond case, can produce gaps with comparable widths and open at lower refractive index contrasts than other proposed FCC dielectric structures.

REFERENCES

1. Zhang, Z.; Glotzer S. C. Nano Lett. 2004, 4, 1407–1413.
2. Gangwal, S.; Cayre, O. J.; Velev, O. D. Langmuir 2008, 24, 13312-13320.
3. Glotzer, S. C. *Science* **2004**, *306*, 419-420.
4. Glotzer, S. C.; Solomon M. J. *Nat. Mater.* **2007**, *6*, 557-562.
5. Glotzer, S. C.; Solomon, M. J.; Kotov, N. A. *AIChE J.* **2004**, *50*, 2978-2985.
6. Ho, K. M.; Chan, C. T.; Soukoulis, C. M. *Phys. Rev. Lett.* **1990**, *65*, 3152-3155.
7. Garcia-Adeva, A. J. *Phys. Rev. B* 73, 2006, 073107.
8. Xia, Y.; Gates, B.; Li, Z.-Y. *Adv. Mater.* **2001**, *13*, 409-413.
9. Simeonov, S.; Bass, U.; McGurn, A. R. *Physica B* **1996**, *228*, 245-250.
10. Sheu, H. R.; El-Aasser , M. S.; Vanderhoff, J. W. *Adv. Mater.* **2003**, *28*, 653-667.
11. Lu, Y.; Yin, Y.; Xia Y. *Adv. Mater.* **2001**, *13*, 415 - 420
12. Mock, E. B.; Zukoski, C. F. *Langmuir*, **2007**, *23* , pp 8760–8771.
13. Kim, J.-W.; Larsen, R. J.; Weitz, D. A. *Adv. Mater.* **2007**, 19, 2005-2009.
14. Lee, S. H.; Song, Y.; Hosein, I. D.; Liddell, C. M. *J. Mater. Chem.*, 2009, **19**, 350.
15. Gay, S. C.; Beale, P. D.; Rainwater, J. C. *Intl. J. Thermphys*. **1998**, *19*, 1535.
16. Johnson, S. G.; Joannopoulos, J. D. *Optics Express* **2001**, *8*, 173-190.
17. S.G. Johnson, J.D. Joannopoulos, The MIT photonic-bands package, http://ab-initio.mit.edu/mpb/.
18. Maldovan, M.; Ullal, C. K.; Carter, W. C.; Thomas E. L. *Nat. Mater.* **2003**, *2*, 664-667.
19. Blanco, A.; Chomski, E.; Grabtchak, S.; Ibisate, M; John, S.; Leonard, S. W.; Lopez, C.; Meseguer, F.; Miguez, H.; Mondia, J. P.; Ozin, G. A.; Toader, O.; van Driel, H. M. *Nature*, **2000**, *405*, 437-440
20. Vlasov, Y. A.; Bo, X. Z.; Sturm, J. C.; Norris, D. J. *Nature*, **2001**, *414*, 289.
21. Caruso, F. *Colloids and Colloid Assemblies*, Wiley: New York, **2003**.

22. W. Dong, H. J. Bongard, F. Marlow, Chem. Mater. 2003, 15, 568-574.

23. Chen, H.-B.; Zhu, Y.-Z.; Cao, Y.-L.; Wang, Y.-P.; Chi, Y.-B. Phys. Rev. B. 2005, 72, 113113.

24. Hillebrand, R.; Matthias, S.; Muller, F. *Phys. Rev. B* **2005**, *71*, 045125.

CHAPTER 8

PHOTONIC BANDGAPS OF THREE-DIMENSIONAL ASYMMETRIC DIMER BASED MONOCLINIC LATTICES

Abstract

Photonic band structure calculations are presented for base-centered monoclinic lattices with an asymmetric dumbbell shape basis. The calculations were made for inverted structures with a refractive index contrast of 3.5. Complete photonic bandgaps opened between the 8th and 9th bands for a range of highly fused particle shapes.

Introduction

Fabricating photonic bandgap materials operating at visible to near-infrared wavelengths has been challenging for top-down approaches due to the technological limitations of lithography and micro-fabrication at nanometer scale lengths. Harnessing self-organizing particle systems is a simple, rapid and cost-effective alternative in producing periodic dielectric structures with optical properties at this scale,[1] and has been an area of intense research over the past two decades.[2]

Spherical colloidal building blocks have been the primary focus of experimental and computational work.[3-6] The close packed phases are utilized for templating high dielectric materials in the form of macroporous structures.[7] While these structures show enhanced photonic properties, the enhancements to the photonic properties are limited and lack robustness. For example, direct FCC dielectric structures (i.e. dielectric spheres in an air matrix) with either homogenous or coated bases show only partial gaps in the optical band structure.[1,8] High refractive index

contrasts (> 2.9) are required for inverted structures (i.e. air spheres in a dielectric matrix), referred to as inverted opals, to produce a complete gap between the 8th and 9th bands. The gap is highly sensitive to small variations in the dielectric periodicity, closing with dispersity in the sphere radius greater than 2%.[9] Other defects such as staking faults or inhomogeneous filling during inversion processes can also inhibit gap formation.[10] The high contrast requirement also limits the range of viable materials for fabrication. The high symmetry close-packing arrangements favor degeneracies in the lower lying photonic bands at the W and U symmetry points in the FCC lattice and P and H in BCC, inhibiting wider and more robust bandgaps from opening.[11-14]

Several variations of the inverted FCC opal have been proposed to improve the optical properties. Examples include non-close packed structures of high dielectric spheres connected by dielectric cylinders,[15] close-packed structures of interconnected hollow spheres[16-18] and skeleton structures composed of dielectric cylinders connecting the tetrahedral and octahedral centers.[19] These structures have complete photonic bandgaps between the 8th and 9th bands, but provide only small improvements on the minimum dielectric contrast required to open a gap.

The structure with the most superior photonic properties is the diamond lattice, which produces the widest gaps proposed for photonic crystal structures.[12] A two sphere basis on the FCC lattice points lifts the degeneracies between the 2nd and 3rd bands, producing gaps in both direct and inverted structures.[13,14] Gap widths as large as 29% are achievable through optimization of the dielectric filling fraction.[13] However, fabricating the diamond structure from colloids has been quite challenging, with the only successful approach being brute-force micro-positioning of spherical particles onto the lattice sites.[19,21]

One proposed method to overcome the limitations of sphere based crystals is to assemble non-spherical building blocks. Preliminary computational work shows that a

non-spherical particle shape basis can break the symmetry induced degeneracies in the FCC close packed systems, allowing a gap to open between the 2nd and 3rd bands.[14] The gaps would then open at lower refractive index contrasts, allowing a broader range of materials to be used as the high dielectric material. Assembling non-spherical dimer- shaped (two spheres overlapping spheres) particles, for example, is one proposed strategy to produce the diamond lattice, if the particles are assembled onto an FCC lattice and oriented properly to give a diamond-like equivalent.[22] Crystals from high refractive index iron oxide dimers (n=3.01), for example, can produce a complete photonic bandgap between the 2nd and 3rd bands.[24] The dimer shape is also a viable non-spherical building block due to the well developed synthetic routes available to produce highly monodisperse particles in large quantities.[25-30]

However, the simulated phases of dimer particles show the stable crystalline lattice is base-centered monoclinic, with particle orientation in the plane of the base-centered face of the unit cell.[31-33] In this work the band structures of crystals with dimer-shaped bases on a base-centered monoclinic lattice are calculated as a function of particle shape. The particle shape in the crystal structure is systematically tuned by adjusting the symmetry of the constituent spheres and their center-to-center distance. Complete bandgaps between the 8th and 9th bands are produced by a range of particle shapes.

Crystal Model and Calculation Methods

Particle Shape

The shape of the asymmetric dimers was described by the normalized bond length parameter $L^* = L / 2r_l$ and the lobe symmetry $S = r_s / r_l$, where L is the center-to-center distance between the lobes, and r_l and r_s are the radii of the larger and smaller lobe, respectively. The model particle shape is spherical when $S \leq 1 - 2L^*$

(i.e., the small lobe lies inside the large lobe) and becomes two tangent spheres when $S = 2L^* - 1$. The region of parameter space satisfying the expression, $S \le -1 + 2\sqrt{1 - \sqrt{3}L^* + L^{*2}}$, consists of particles whose morphology resembles a sphere with a protruding nub which will fit into the interstices of the large spherical lobes in a close-packed arrangement[31]. We consider only dimers with $S > -1 + 2\sqrt{1 - \sqrt{3}L^* + L^{*2}}$ and $S > 2L^* - 1$ for optical band structure calculations to avoid the cases when the lobes no longer touch, are fused completely into one sphere, or have protrusions small enough to stabilize the interstice-based "degenerate" [31,32] crystal where large lobes tile a triangular lattice and small lobes uniformly populate the pore spaces. Figure 8.1 shows the boundaries of the particle shape parameter space explored here for orientationally-ordered arrangements.

The photonic band structures were calculated as a function of the particle parameters *S* and *L**, with a resolution of 0.05 in the parameter values.

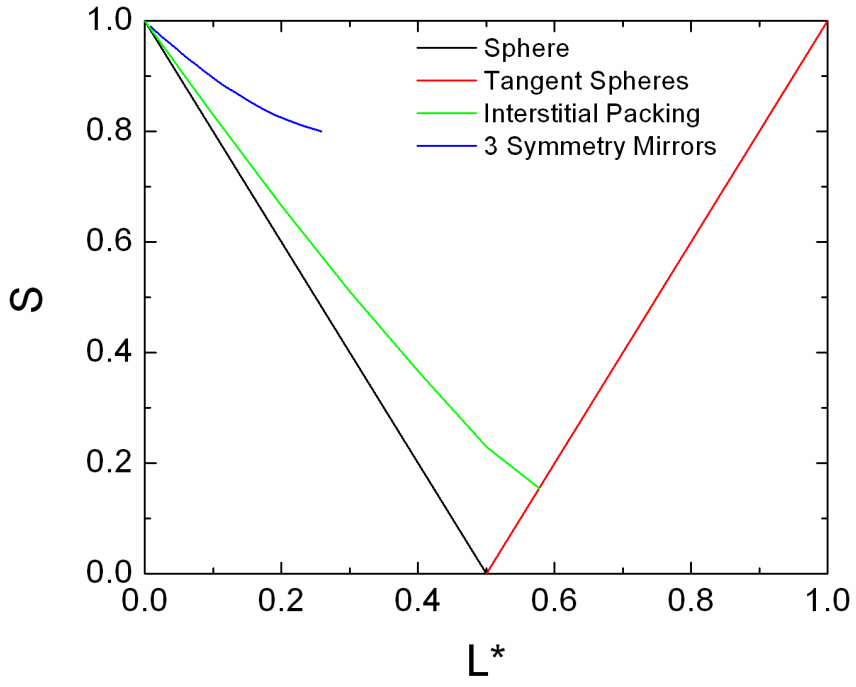

Figure 8.1. Particle shape parameter space.

Crystal Structure

Figure 8.2 shows a 3D model of the non-primitive unit cell of the crystal. The base-centered monoclinic lattice has non-primitive lattice constants *a*, *b* and *c*, with angles $\alpha \neq 90°$ and $\beta = \gamma = 90°$. The lattice consists of stacked 2D oblique lattices planes,[34] with dimers aligned in-plane. The non-primitive centered rectangular unit cell of the oblique lattice[35] constitutes the base-centered face in the 3D non-primitive unit cell. The lattice constants *b* and *c*, are defined as the sides of the base-centered face (see supplemental Figure S2). Close packing the dimers in this plane yields,

$$b = 2(\sqrt{r_2^2 + 2r_1r_2} + L)$$

$$c = 2r_1$$

The oblique lattices are stacked vertically with an offset in the direction of *b* and packed such that the large sphere of one particle is tangent to both small and large lobe of the particle below it (Figure 8.6). The value of the third lattice constant *a* is $2r_1$. The angle α can be determined from the triangle made from sides of lengths r_1, r_1+r_2 and *L*, where α is opposite length r_1+r_2. From the law of cosines,

$$\alpha = \cos^{-1}\left(\frac{L^2 + 4r_1^2 - (r_1 + r_2)^2}{4Lr_1}\right)$$

We followed the convention of Ruzaikin et al. to define the base-centered monoclinic primitive lattice vectors,[36]

$$a_1 = (a,0,0),\ a_2 = (\frac{b}{2}\cos\alpha, \frac{b}{2}\sin\alpha, -\frac{c}{2}),\ a_3 = (\frac{b}{2}\cos\alpha, \frac{b}{2}\sin\alpha, \frac{c}{2})$$

Symmetry

The lattice has a two-fold rotation axis (z-axis) and mirror plane (z = 0) which cuts the base-centered face along the direction of the lattice constant *b*. The symmetry of the lattice is classified as C_{2h} (*2/m*). For specific values of *S* and *L** the crystal structure has two additional mirror planes at x = 0 and y = 0 (see supporting

information for the calculation). In this special case, the crystal is face-centered orthorhombic and the symmetry classification of the lattice is D_{2h} (*mmm*). Figure 8.1 shows the curve representing the shape parameters which produce the orthorhombic lattice.

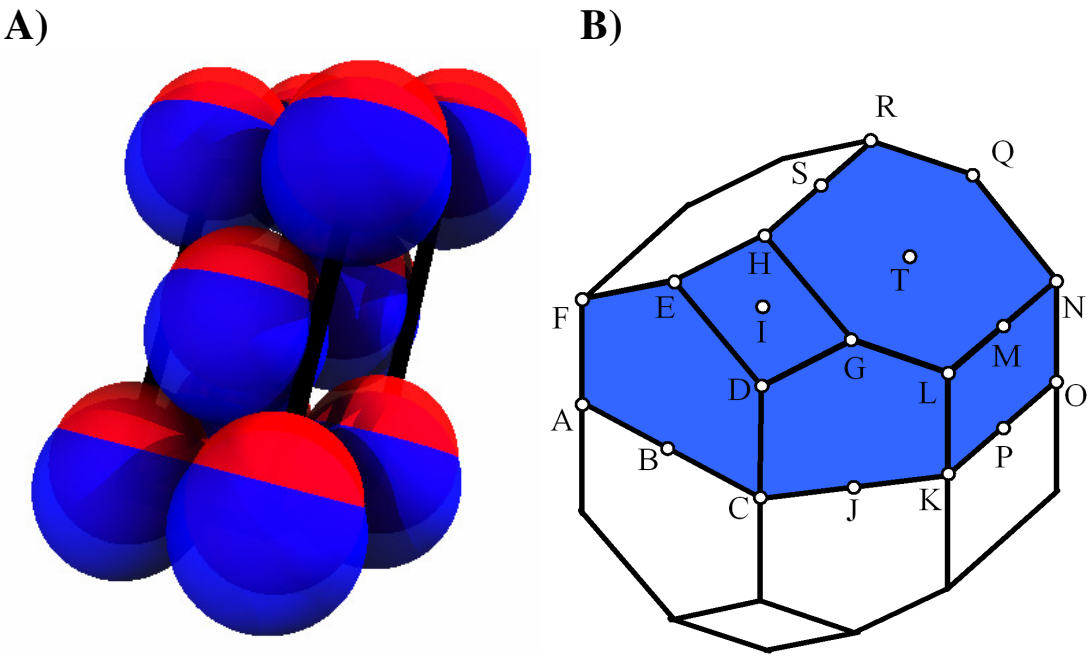

Figure 8.2. Monoclinic crystal structure. A) Non-primitive unit cell of dimer based crystal structure, with based centered monoclinc structure. Shape parameters are L*=0.1 and S=0.9. Blue and red spheres represent the large and small lobe, respectively. B) Corresponding 1st Brillouin zone, with the irreducible zone shaded. Critical points along the Brillouin zone surface are marked with white dots.

The Brillouin Zone

The shape of and critical point positions on the 1st Brillouin zone depend on the lattice constants and angle α. Ruzaikin et al. identified four Brillouin zone types, depending on which reciprocal lattice vectors define the faces of the Brillouin zone.[36] In the present case the lattice constants and angle α were a function of particle shape, thus the Brillouin zone and all its critical points were also calculated as a function of the shape parameters *S* and *L**. As an example, Figure 8.2b shows the 1st Brillouin zone for *S*=0.9 and *L**=0.1. The Brillouin zone assumed the higher

symmetry due to the particular shape parameters that produced additional symmetry in the crystal structure. This distorted FCC Brillouin zone is characteristic for an orthorhombic structure.[37]

Figure 8.2b also shows the irreducible Brillouin zone region. Photonic band calculations were performed for a mesh of interpolated points in the irreducible Brillouin zone. In all, a total of 501 k-points were calculated to construct the band structure. For simplicity, the band structures were labeled in order of the k-points calculated, from 1 to 501. See supporting information for the order of calculated k-points relative to their locations on the irreducible Brillouin zone (Figure 8.7).

Simulation

Photonic band structures were numerically calculated using the plane wave method in the full vectorial formulation,[38] implemented using the MIT Photonic Bands Package.[39] The resolution and mesh size of the computational cell were 16 and 5, respectively, and a convergence tolerance of 0.001% was used to determine the eigenfrequencies. Band structures were computed for inverted structures with a high refractive index matrix of 3.5, a value simulating crystalline silicon.[40] The calculated frequencies were produce in normalized units of c/a, where a is the magnitude of the lattice vector a_1.

Results & Discussion

Photonic bandgaps were observed for a range of high fusion (small L^*) particle shapes, opening between the 8^{th} and 9^{th} bands. Figure 8.3 shows the calculated photonic band structure of a crystal from particles with S=0.965 and L^*=0.03. This particle shape produced the largest gap-to-midgap ratio of 4.47% centered at a normalized frequency of 0.5717. The region of parameter space where gaps opened

was between $L^*=0$ to $L^*=0.2$ and $S=0.8$ to $S=1$. The contour plot of gap-to-midgap ratio versus S and L^* (Figure 8.4) showed that a range of particle shapes produced photonic bandgaps in proximity to the 3-mirror symmetries line identified in Figure 8.1. For a given symmetry S, the gaps were maximal when the L^* corresponded to a value on the mirror symmetry line. These results are most likely attributed to the Brillouin zones approximating a spherical shape, for this range of shape parameters, which is an optimal feature for bandgap formation.[13] The parameters on this line produce the most closely approximated spherical Brillouin zones, which lead to the largest gaps.

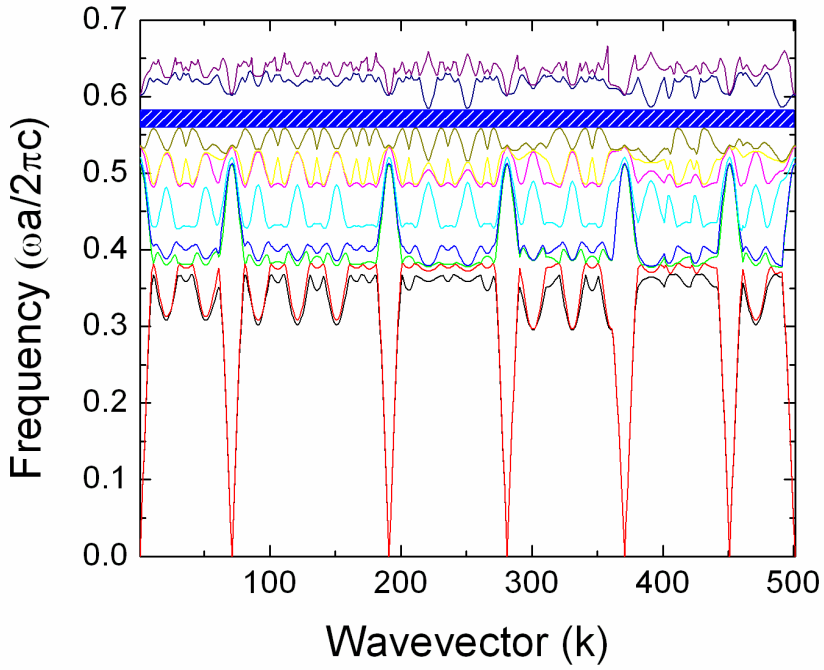

Figure 8.3. Photonic band structure, with L*=0.03 and S=0.965, producing a gap width of 4.47% between the 8th and 9th bands.

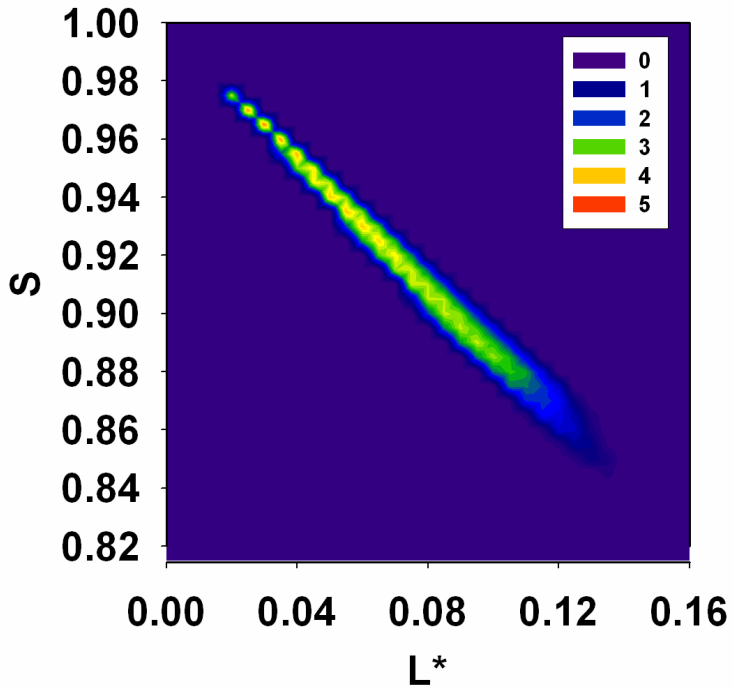

Figure 8.4. Contour plot of gap to midgap ratio versus S and L*.

The photonic band structures were systematically examined as a function of both filling fraction (i.e. volume percentage of the high refractive index material) and refractive index contrast for the particle shape that maximized the gap at close packing (i.e. S=0.965 and L*=0.03). The filling fraction was adjusted by varying the radius of the constituent lobes of the particles while the lattice constants remained fixed. Radii larger than the particle lobes emulate either physically sintering[41] the particles to fuse them together or subsequently depositing an additional layer (i.e. shell) of material on the particle surface.[42,43] The structures examined in this study are inverted replicas of the particle assembly that would be produced via removing the particles through chemical etching techniques or calcination after deposition of index material.[5] Following template removal, coating the inner walls of the network with additional high index material would produce pores with smaller radii than those for close packing arrangements. Bandgap values calculated for high dielectric shell structures were smaller than for structures made from complete filling of the

interstitial space, therefore only the latter was considered in the optimization.

Figure 8.5a shows the gap width as a function of filling fraction. The filling fraction at close packing maximized the gap, which experimentally offers the advantage of not requiring a volume fraction adjustment of the assembled template (i.e., sintering). The filling fraction range for the existence of complete bandgaps show in Figure 8.5 (14.02%-37.69%) is comparable to the range for the inverted opal (12.35%-37.01%),[41] indicating a similar stability of the gap. Inverted opals require interstitial filling fractions of 90%-97% in order to maximize the bandgap, which translates to dielectric volume fractions of 23.4%-25.2%. To achieve this filling range, high dielectric shells are typically grown on the colloidal template surface via vacuum deposition techniques such as chemical vapor deposition or atomic layer deposition, until the desired thickness is achieved. Filling fractions below or above this optimal range will begin to decrease the gap width, thus necessitating careful control over the shell thickness during infiltration. The gap to midgap ratio saturated to a value of approximately 13.78% upon increasing the index contrast (Figure 8.5b). The critical refractive index contrast to open a gap was approximately 2.94, which is comparable to the inverted opal value of approximately 2.90.[41] As a comparison, the skeleton inverse opal with the same high dielectric value achieves a gap width of approximately 3.6% and opens a gap at a refractive index of 2.91.[19] Spherical shells connected by cylindrical pores can produce much larger gaps at this dielectric value (~15%) and a gap opens at a refractive index of 2.3.

Calculations for direct structures were also made, however no gaps were produced for any particle shape. Additionally, monoclinic lattices produced by stacking the oblique planes with offset in the direction of c were also examined. However, these structures did not produce bandgaps for any particle shape within the parameter space examined in this study.

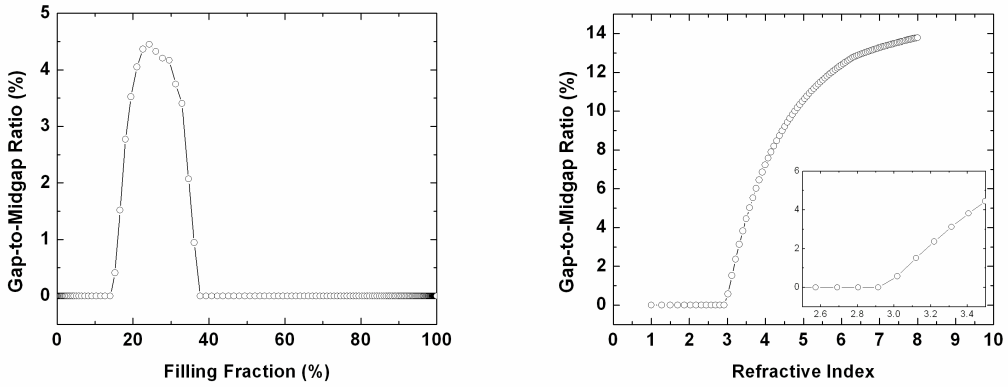

Figure 8.5. Gap to midgap ratio as a function of A) filling fraction and B) refractive index, for crystal structure from particles with L*=0.03 and S=0.965. Inset shows close up of the onset of a bandgap.

Conclusions

The photonic band structures for dumbbell based inverted dielectric structures were calculated as a function of the particle shape parameters. Complete photonic bandgaps between the 8th and 9th bands were found for highly fused particle shapes, and the gap was maximal at the close packing filling fraction. The gaps showed comparable stability to inverted opals. The fabrication process for producing bandgap materials from these particles should be simplified compared to spherical particles by not requiring volume fraction adjustments of the template or carefully monitoring the deposition of the high dielectric material.

Supporting Information

Determining the lattice constant b

The base-centered face on the lattice has a centered rectangle 2D unit cell. Figure 8.6 shows the close packing arrangement of three dumbbells and a enrlaged view of the contact between the two small lobes of one particle with the large lobe of

another. The lattice constant been can be expressed as,

$b = 2(x + L) = 2(\sqrt{r_2^2 + 2r_1 r_2} + L)$

and the lattice constant c is,

$c = 2r_1$

*Additional symmetry for certain S and L**

The additional mirror symmetries exist when the lattice constants *a* and *b* satisfy the equation $b\cos\theta = a$ which can be expressed in terms of the particle shape parameters: $(\sqrt{S(S+1)} + 2L^*)(4L^{*2} + 4 - (1-S)^2) = 8L^*$

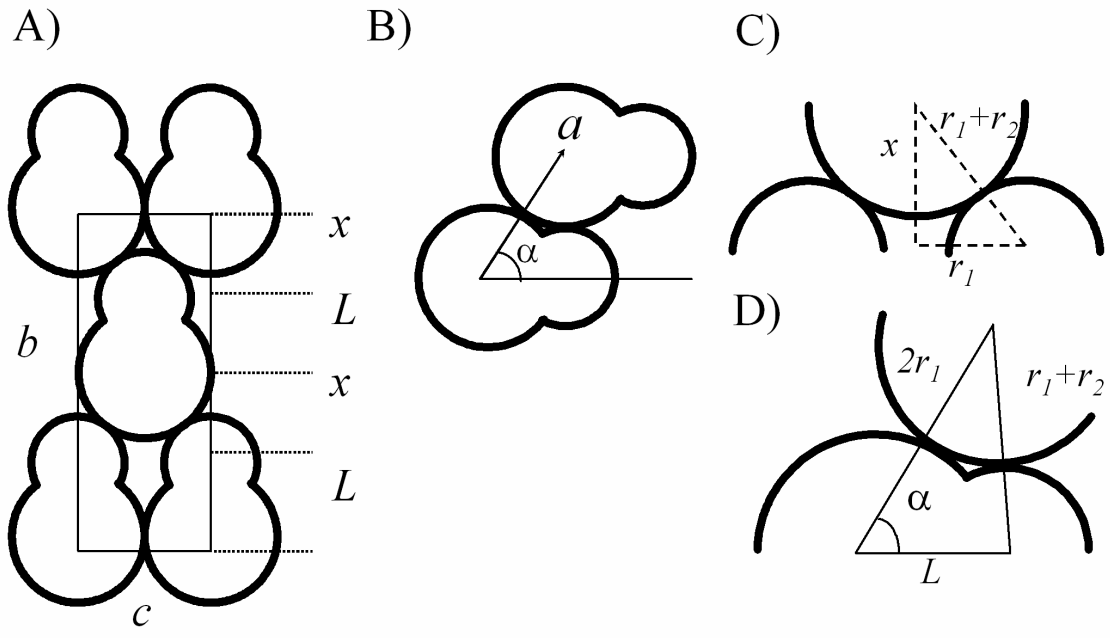

Figure 8.6. Packing geometries of particles on A) a centered rectangle 2D unit cell and B) stacking of the particle layer above the previous layer, in the direction of the lattice constant *a*. The large lobe of one particle is tangent to both the small and large lobe of the particle below it. C) Close up of the 2D close packing of the dimers, enlarged. The large lobe of center particles is tangent to the small lobes of the particles on the corners of the unit cell. D) Close packing of adjacent stacked particles.

Interpolated points in the irreducible Brillouin zone

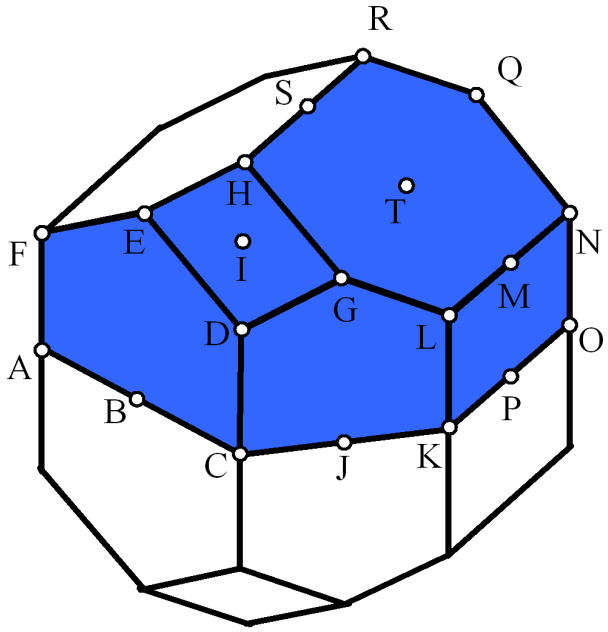

Figure 8.7. Brillouin zone for base-centered monoclinic lattice, with the critical k-points labeled. Irreducible zone is shaded.

Figure 8.7 shows the brillouin zone with the relevant k-points in the irreducible zone labeled. The Gamma Γ point is now shown. The order in which the k-points of the brillouin zone were calculated was:

Γ-D-B-E-F-B-A-Γ-H-T-N-L-T-R-Q-T-G-H-R-Γ-D-G-I-E-D-I-H-E-Γ-K-J-C-D-J-L-G-J-Γ-K-P-O-L-K-N-O-Γ-S-T-M-P-Γ

Interpolation of 9 additional points between these k-points was done to produce sufficient amount of k-points to examine the photonic band structure of the crystals.

REFERENCES

1. Busch, K.; John, S. *Phys. Rev. E* **1998**, *58*, 3896-3908.
2. Colvin, V. *MRS Bull.* **2001**, 637-641
3. Garcia-Santamaria, F.; Salgueirino-Maceira, V.; Lopez, C.; Liz-Marzan, L. M. *Langmuir* **2002**, *18*, 4519.
4. Gu, Z. Z.; Fujishima, A.; Sato, O. *Chem. Mater.* **2002**, *14*, 760.
5. Tétreault , N.; Míguez H., ; Ozin, G. A. *Adv. Mater.* **2004**, *16*, 1471 – 1476.
6. Stein, A.; Schroden, R. C. *Curr. Opin. Solid State Mater. Sci.* **2001**, *5*, 553.
7. Colloids and Colloid Assemblies
8. Moroz, A.; Sommers, C. *J. Phys.: Condens. Matter* **1999**, *11*, 997-1008.
9. Li, Z.-Y.; Zhang Z.-Q. *Phys. Rev. B* **2000**, *62*, 1516..
10. Vlasov, Y. A.; Astratov, V. N.; Baryshev, A. V.; Kaplyanskii, A. A.; Karimov, O. Z.; Limonov, M. F. *Phys. Rev. E* **2000**, *61*, 5784.
11. Li, Z.-Y.; Wang, J.; Gu, B.-Y. *Phys. Rev. B* **1998**, *58*, 3721 – 3729.
12. Maldovan, M.; Thomas, E. L. *Nat. Mater.* **2004**, *3*, 593-600.
13. Ho, K. M.; Chan, C. T.; Soukkoulis, C. M., *Phys. Rev. Lett.* **1990**, *65*, 3152-3155.
14. Yablonovitch, E.; Gmitter, T. J.; Leung, K. M. *Phys. Rev. Lett.* **1991**, *67*, 2295-2298.
15. Biswas, M.; Sigalas, M.; Subramania, G.; Ho, K.-M. *Phys. Rev. B* **1999**, *57*, 3701-3705.
16. Chen, H.-B.; Zhu, Y.-Z.; Cao, Y.-L.; Wang, Y.-P.; Chi, Y.-B. Phys. Rev. B **2005**, *72*, 113113.
17. Miguez, H.; Tétreault, N.; Yang, S. M.; Kitaev, V.; Ozin, G. A. *Adv. Mater.* **2003**, *15*, 597-600.

18. Rengarajan, R.; Jiang, P.; Colvin, V.; Mittleman, D.; *Appl. Phys. Lett.* 2000, *77*, 3517.
19. Dong, W.; Bongard, H. J.; Marlow, F. *Chem. Mater.* **2003**, *15*, 568-574.
20. Garcia-Santamaria, F.; Lopez, C.; Meseguer, F.; Lopez-Tejeira F.; Sanchez-Dehesa, J.; Miyazaki, H. T. *Appl. Phys. Lett.* **2001**, *79*, 2309-2311.
21. Garcia-Santamaria, F.; Miyazaki , H.T.; Urquia , A.; Ibisate , M.; Belmonte , M.; Shinya , N.; Meseguer , F.; Lopez , C. *Adv. Mater.* **2002**, *14*, 1144 – 1147.
22. Lu , Y.; Yin , Y.; Xia, Y. Adv. Mater. **2001**, *13*, 415 – 420.
23. Matijevic, E.; Scheiner, P. *J. Colloid Interface Sci.* **1978**, *63*, 509.
24. Xia, Y.; Gates, B.; Li, Z.-Y. *Adv. Mater.* **2001**, *13*, 409-413.
25. Sugimoto, T.; Khan, M. M.; Muramatsu, A. *Colloid Surf. A: Physicochem. Eng. Aspects* **1993**, *70*, 167.
26. Sugimoto, T.; Itoh, H.; Mochida, T.; *J. Colloid Interface Sci.* **1998**, *205*, 42.
27. Ocana, M.; Morales, M. P.; Serna, C. J.; *J. Colloid Interface Sci.* **1995**, *171*, 85.
28. Mock, E. B.; De Bruyn, H.; Hawkett, B. S.; Gilbert, G. S.; Zukoski, C. F. *Langmuir*, **2006**, *22*, 4037–4043.
29. Kim, J. W.; Larsen, R. J.; Weitz, D. A. *J. Amer. Chem. Soc.* **2006**, *128*, 14374–14377.
30. Kim, J.-W.; Larsen, R. J.; Weitz, D. A. Advanced Materials **19**, 2005-2009 (2007).
31. Gay, S. C.; Beale, P. D.; Rainwater, J. C. *Intl. J. Thermphys.* **1998**, *19*, 1535.
32. Vega, C.; Paras, E. P. A.; Monson, P. A. *J. Chem. Phys.* **1992**, *96*, 9060–9072.
33. Marechal, M.; Dijkstra, M. *Phys. Rev. E* **2008**, *77*, 061405.
34. Hammond, C. *The Basics of Crystallography and Diffraction, 2nd Ed.* Oxford University: Oxford, **2001**
35. Allen, S.M.; Thomas, E. L. *The Structure of Materials*, Wiley: New York, 1999.
36. Ruzaikin, P.; Kudryavtseva, N. V. *Russian Physics Journal* **1974**, *17*, 934-938.

37. Schilling, J.; White, J.; Scherer, A.; Stupian, G.; Hillebrand, R.; Gosele, U. *Appl. Phys. Lett.* **2005**, *86*, 011101.

38. Johnson, S.G.; Joannopoulos, J. D. *Optics Express* **2001**, *8*, 173-190.

39. Johnson, S.G.; Joannopoulos, J.D. *The MIT photonic-bands package*, http://ab-initio.mit.edu/mpb/.

40. Toneva, A.; Mihailova, T.; Danesh, P.; Pantchev, B.; *Semicond. Sci. Technol.* **1994**, *9*, 2285.

41. Míguez, H.; Meseguer, F.; Lopez, C.; Blanco, A.; Moya, J. S.; Requena, J.; Mifsud, A.; Fornes V. *Adv. Mater.* **1999**, *10*, 480-483.

42. Blanco, A.; Chomski, E.; Grabtchak, S.; Ibisate M., ; John, S.; Leonard, S. W.; Lopez, C.; Meseguer, F.; Miguez, H.; Mondia, J. P.; Ozin, G. A.; Toader, O.; van Driel, H. M. *Nature* **2000**, *405*, 437-440.

43. Vlasov, Y. A.; Bo, X. Z.; Sturm, J. C.; Norris, D. J. *Nature*, **2001**, *414*, 289.